Hydrogeophysical investigation of the impact of invasive tree species on groundwater at the Dayspring Children's Village, South Africa

David Dillon Ngobeni

School of Geosciences, University of the Witwatersrand

A Dissertation submitted to the Faculty Science, University of the Witwatersrand, Johannesburg, in fulfillment of the requirements for the degree of Master of Science

Johannesburg, 2013

DECLARATION

I declare that this Dissertation is my own, unaided work. It is being submitted for the Degree of Master of Science at the University of the Witwatersrand, Johannesburg. It has not been submitted before for any degree or examination at any other University.

(Signature of candidate)

09 day of October 20 13 in Braamfontein

Abstract

Dayspring Children's Village, which is located about 66 km northwest of Johannesburg, has been experiencing a chronic shortage of water for over 30 years. Five out of seven boreholes that are scattered within the school property are dry and there is evidence of contamination in one of the two wells that are producing water at two depths. The presence of bluegum (Eucalyptus globulus) trees is suspected to be the principal cause for the depletion of the aquifer(s) because of their documented high rate of transpiration. The purpose of this project is to determine the complex interaction between the plants and structural elements of the various aquifers, site wells for clean water, and assist with explaining the existing contamination. This study involved parallel studies by other students. My focus was the use time-lapse DC resistivity to map preferential pathways of groundwater so that the impact of the bluegum trees could be determined. Other geophysical studies included time-domain electromagnetics, gravity and magnetics. These methods were used to map geological contacts, lithologies, geological structures, and the distribution of groundwater. Hydrogeology results from a parallel study have shown that there at least two aquifer system at Dayspring School. Time-lapse resistivity and gravity measurements were collected towards the end of rainy season and towards the end of dry season. The results show that groundwater at Dayspring School is largely structurally controlled. The impact of the bluegum trees is not obvious, but it was concluded that the trees are not the cause of apparent groundwater depletion because their root lengths do not reach the mapped geologic structures.

Acknowledgements

I would like to extend my sincere gratitude to the following organisations and people for their assistance and support.

- Dr. Susan Webb for financial support.
- Geoscientists Without Borders and SEG for financial support.
- Professor Raymond Durrheim and NRF for financial support.
- Dr. Susan Webb and Dr. Michael Jones for tremendous supervision. Your hands-on assistance in the field did not go unnoticed.
- The Council for Geosciences for personnel, ground TDEM data and the CG-5
- Fugro Airborne, especially Mr. Darren Burrows, for the TDEM and magnetic data.
- Professor Tamiru Abiye for assistance with hydrogeology insight.
- My parents, especially my mother Aidah Theko, for her unreserved and unconditional support and sacrifices.
- My cousin Peter Ngobeni, for his support.
- Professor Robert de Mello Koch for sparking the interest in me to do research.
- My loving fiancée Miss Nkateko Sowane for her support and assistance during fieldwork.
- Professor Lew Ashwal for assistance in the field.
- Miss Madeline Lee for assistance and support during fieldwork.
- Honours students, Mr. Obone Sepato, Miss Sally-Anne Lee, and Miss Racheal Goba for their valuable data.

Contents

Chapter 1. Introduction 1

1.1 General Introduction 1

1.2 Background 4

1.3 Aims and objectives 5

1.4 General materials and methods 6

1.5 Limitations 6

Chapter 2. Geological setting and climatic conditions of the study area 7

2.1 Geology 7

2.1.1 Regional geology 7

2.1.2 Local geology 9

2.1.2.1 Description of the rocks 10

2.1.2.2 Weathering profile 11

2.2 Climatic conditions of the study area 14

Chapter 3. DC Resistivity surveys at Dayspring School 16

3.1 General introduction 16

3.2 DC Resistivity surveys 16

3.2.1 Introduction 16

3.2.2 Basic principles of the DC resistivity method 17

3.2.2.1 Data acquisition 17

3.2.2.2 Inversion 19

3.2.2.3 Advantages and disadvantages of the arrays used 22

3.2.2.4 Interpretation principles 23

3.2.3 Materials and methods 33
3.2.3.1 Description of the equipment and materials employed. 33
3.2.4 Experiments 36
3.2.4.1 Description of the experiment 36
3.2.5 Results and interpretations 37
3.2.6 Discussion of results 62
Chapter 4. Other data sets at Dayspring School 71
4.1 Preliminary DC Resistivity surveys at Dayspring School 71
4.1.1.1 Description of the equipment and materials employed. 71
4.1.1.2 Data acquisition in 2009 and 2010 71
4.1.1.3 Results and interpretations 73
4.2 Time-domain electromagnetic surveys at Dayspring School 80
4.2.1 Introduction 80
4.2.2 Basic principles of the TDEM method 80
4.2.3 Airborne TDEM 81
4.2.3.1 Materials and methods 81
4.2.3.2 Experiments and results 82
4.2.4 Ground TDEM 85
4.2.4.1 Materials and methods 85
4.2.4.2 Experiments and results 87
4.2.5 Discussion of results 91
4.3 Microgravity surveys at Dayspring School 92
4.3.1 Introduction 92
4.3.2 Basic principles of the gravity method 92

4.3.3 Materials and methods 93
4.3.3.1 Description of the equipment and materials employed. 93
4.3.3.2 Explanation of the way in which the work was done. 93
4.3.4 Experiments and results 95
4.3.4.1 Description of the experiment 95
4.3.4.2 Description of the results 95
4.3.5 Discussion of results 97
4.4 Magnetic surveys at Dayspring School 99
4.4.1 Introduction 99
4.4.2 Basic principles of the magnetic method 99
4.4.3 Airborne Magnetics 99
4.4.3.1 Materials and methods 99
4.4.3.2 Experiments and results 100
4.4.4 Ground magnetics 102
4.4.4.1 Materials and methods 102
4.4.5 Experiments and results 104
4.4.5.1 Description of the results. 105
4.4.6 Discussion of results 106
4.5 Hydrogeology surveys at Dayspring School 108
4.5.1 Introduction 108
4.5.2 Basic principles of the hydrogeology method 108
4.5.2.1 Groundwater Chemistry 108
4.5.3 Materials and methods 111
4.5.3.1 Description of the equipment and materials employed. 111

4.5.3.2 Explanation of the way in which the work was done. 111
4.5.4 Results and discussions 112
Chapter 5. General discussion 114
Chapter 6. Conclusion and recommendations for further work 121
6.1 Conclusion 121
6.2 Recommendations 122
References 123
Appendix 133

List of Figures

FIGURE 1.1. LOCALITY MAP OF THE STUDY AREA. (A) MAP OF SOUTHERN AFRICA. (B) THE ZOOMED-IN MAP SHOWING THE POSITION OF DAYSPRING SCHOOL RELATIVE TO JOHANNESBURG. 2
FIGURE 1.2. A MAP OF THE BOREHOLE LOCALITIES AT THE DAYSPRING SCHOOL. 5
FIGURE 2.1. A SIMPLIFIED GEOLOGY MAP (GEOLOGICAL SURVEY OF SOUTH AFRICA, 1981) OF THE REGION SHOWING THE POSITION OF THE STUDY AREA WITH THE FILLED POLYGON..... 8
FIGURE 2.2. THE DISTRIBUTION OF ROCK FLOATS, BOULDERS AND OUTCROPS AT DAYSPRING SCHOOL. 10
FIGURE 2.3. SOIL AND ROCK CHIPS COLUMN FROM BOREHOLE DS2. 12
FIGURE 2.4. AN EXAMPLE OF THE TOP REGOLITH FROM ONE OF THE PITS AT DAYSPRING SCHOOL. THE GEOLOGICAL HAMMER CAN BE USED FOR SCALE. 13
FIGURE 2.5. REGIONAL RAINFALL DATA OF THE STUDY AREA REPRESENTING DATA MEASURED FROM JANUARY 2007 TO DECEMBER 2011. (A) SHOWS DATA FROM JANUARY 2007 TO DECEMBER 2008, (B) SHOWS DATA FROM JANUARY 2009 TO DECEMBER 2010, AND (C) SHOWS DATA FROM JANUARY 2011 TO DECEMBER 2011 (G. WILLIAMS, PERSONAL COMMUNICATION, JANUARY 11, 2012).....15
FIGURE 3.1. TYPICAL RANGE OF RESISTIVITIES AND CONDUCTIVITIES OF GEOLOGIC MATERIALS; AFTER PALACKY (1988) 25
FIGURE 3.2 TEST MODEL WITH SMALL RECTANGULAR BLOCK. 27
FIGURE 3.3 MODEL OF SYNTHETIC METALLIC PIPE BURIED AT 3.6 M. (A) APPARENT RESISTIVITY DUE TO A LOW RESISTIVITY PRISM. (B) INVERSION MODEL OF THE SYNTHETIC METALLIC BURIED PIPE. 27
FIGURE 3.4. MODEL OF SYNTHETIC METALLIC PIPE BURIED AT 1.5 M. (A) APPARENT RESISTIVITY DUE TO A LOW RESISTIVITY PRISM. (B) INVERSION MODEL OF THE SYNTHETIC METALLIC BURIED PIPE. 28
FIGURE 3.5. MODEL OF SYNTHETIC METALLIC PIPE BURIED AT 1.5 M WITH THE RESISTIVITY CONTRAST REDUCED FROM 1:100 TO 10:100. (A) APPARENT RESISTIVITY DUE TO A LOW RESISTIVITY PRISM. (B) INVERSION MODEL OF THE SYNTHETIC METALLIC BURIED PIPE. 28
FIGURE 3.6. A 2D TWO-LAYER MODEL WITH LOW AND RESISTIVITY PRISMS. (A) IS THE ACTUAL MODEL, (B) THE PSEUDO-SECTION OF THE FORWARD MODEL, AND (C) THE INVERSE MODEL FOR THE WENNER-SCHLUMBERGER ARRAY. 29
FIGURE 3.7. A 2D TWO LAYER MODEL OF WIDE (11 M) FRACTURE BELOW A THICK (20 M) OVERBURDEN. (A) IS THE ACTUAL MODEL, AND (B) IS THE INVERSE MODEL FOR THE WENNER-SCHLUMBERGER ARRAY. 31
FIGURE 3.8. SYNTHETIC TIME-LAPSE RESISTIVITY INVERSIONS. (A) THE ACTUAL MODEL FOR THE INITIAL DATA SET WITH TWO PRIMS OF LOW (10 Ω·M) AND HIGH (1500 Ω·M) RESISTIVITY. (B) INVERSION

model after the resistivity of the top and bottom layers were increased by 15 and 5% respectively, while the resistivity of the prisms remained unchanged. (c) Inversion model after the resistivity of the top layers was increased by 15% and the resistivity of the bottom was decreased by 5%, while the resistivity of the prisms remained unchanged. 32
Figure 3.9. Image showing survey lines which were measured in 2011.....35
Figure 3.10: Electrical image along profile 7. (a) is the contoured apparent resistivity measured in in April 2011, (b) is the contoured apparent resistivity measured in in September 2011, (c) and (d) are the inverse models that represent the approximate electrical resistivity and depth of the geologic formations for the April and September data sets respectively, and (e) is the difference plot between the two periods starting from April 2011 to September 2011.....39
Figure 3.11. Electrical image along profile 9. (a) is the contoured apparent resistivity measured in in April 2011, (b) is the contoured apparent resistivity measured in in September 2011, (c) and (d) are the inverse models that represent the approximate electrical resistivity and depth of the geologic formations for the April and September data sets respectively, and (e) is the difference plot between the two periods starting from April 2011 to September 2011.....41
Figure 3.12. Electrical image along profile 11. (a) is the contoured apparent resistivity measured in in May 2011, (b) is the contoured apparent resistivity measured in in September 2011, (c) and (d) are the inverse models that represent the approximate electrical resistivity and depth of the geologic formations for the May and September data sets respectively, and (e) is the difference plot between the two periods starting from May 2011 to September 2011. 43
Figure 3.13. Electrical image along profile 13. (a) is the contoured apparent resistivity measured in in May 2011, (b) is the contoured apparent resistivity measured in in September 2011, (c) and (d) are the inverse models that represent the approximate electrical resistivity and depth of the geologic formations for the May and September data sets respectively, and (e) is the difference plot between the two periods starting from May 2011 to September 2011. 45
Figure 3.14. Electrical image along profile 15. (a) is the contoured apparent resistivity measured in in April 2011, (b) is the contoured apparent resistivity measured in in September 2011, (c) and (d) are the inverse models that represent the approximate electrical resistivity and depth of the geologic formations for the April and September data sets respectively, and (e) is the difference plot between the two periods starting from April 2011 to September 2011.....47

FIGURE 3.15. ELECTRICAL IMAGE ALONG PROFILE 17. (A) IS THE CONTOURED APPARENT RESISTIVITY MEASURED IN IN APRIL 2011, (B) IS THE CONTOURED APPARENT RESISTIVITY MEASURED IN IN SEPTEMBER 2011, (C) AND (D) ARE THE INVERSE MODELS THAT REPRESENT THE APPROXIMATE ELECTRICAL RESISTIVITY AND DEPTH OF THE GEOLOGIC FORMATIONS FOR THE APRIL AND SEPTEMBER DATA SETS RESPECTIVELY, AND (E) IS THE DIFFERENCE PLOT BETWEEN THE TWO PERIODS STARTING FROM APRIL 2011 TO SEPTEMBER 2011. 49
FIGURE 3.16. ELECTRICAL IMAGE ALONG CROSSLINE 10. (A) IS THE CONTOURED APPARENT RESISTIVITY MEASURED IN IN MAY 2011, (B) IS THE CONTOURED APPARENT RESISTIVITY MEASURED IN IN SEPTEMBER 2011, (C) AND (D) ARE THE INVERSE MODELS THAT REPRESENT THE APPROXIMATE ELECTRICAL RESISTIVITY AND DEPTH OF THE GEOLOGIC FORMATIONS FOR THE MAY AND SEPTEMBER DATA SETS RESPECTIVELY, AND (E) IS THE DIFFERENCE PLOT BETWEEN THE TWO PERIODS STARTING FROM MAY 2011 TO SEPTEMBER 2011. 51
FIGURE 3.17. ELECTRICAL IMAGE ALONG CROSSLINE 12. (A) IS THE CONTOURED APPARENT RESISTIVITY MEASURED IN IN MAY 2011, (B) IS THE CONTOURED APPARENT RESISTIVITY MEASURED IN IN SEPTEMBER 2011, (C) AND (D) ARE THE INVERSE MODELS THAT REPRESENT THE APPROXIMATE ELECTRICAL RESISTIVITY AND DEPTH OF THE GEOLOGIC FORMATIONS FOR THE MAY AND SEPTEMBER DATA SETS RESPECTIVELY, AND (E) IS THE DIFFERENCE PLOT BETWEEN THE TWO PERIODS STARTING FROM MAY 2011 TO SEPTEMBER 2011 53
FIGURE 3.18. ELECTRICAL IMAGE ALONG CROSSLINE 15. (A) IS THE CONTOURED APPARENT RESISTIVITY MEASURED IN IN MAY 2011, (B) IS THE CONTOURED APPARENT RESISTIVITY MEASURED IN IN SEPTEMBER 2011, (C) AND (D) ARE THE INVERSE MODELS THAT REPRESENT THE APPROXIMATE ELECTRICAL RESISTIVITY AND DEPTH OF THE GEOLOGIC FORMATIONS FOR THE MAY AND SEPTEMBER DATA SETS RESPECTIVELY, AND (E) IS THE DIFFERENCE PLOT BETWEEN THE TWO PERIODS STARTING FROM MAY 2011 TO SEPTEMBER 2011 55
FIGURE 3.19. ELECTRICAL IMAGE ALONG CROSSLINE 17. (A) IS THE CONTOURED APPARENT RESISTIVITY MEASURED IN IN MAY 2011, (B) IS THE CONTOURED APPARENT RESISTIVITY MEASURED IN IN SEPTEMBER 2011, (C) AND (D) ARE THE INVERSE MODELS THAT REPRESENT THE APPROXIMATE ELECTRICAL RESISTIVITY AND DEPTH OF THE GEOLOGIC FORMATIONS FOR THE MAY AND SEPTEMBER DATA SETS RESPECTIVELY, AND (E) IS THE DIFFERENCE PLOT BETWEEN THE TWO PERIODS STARTING FROM MAY 2011 TO SEPTEMBER 2011 57
FIGURE 3.20. ELECTRICAL IMAGE ALONG CROSSLINE 19. (A) IS THE CONTOURED APPARENT RESISTIVITY MEASURED IN IN MAY 2011, (B) IS THE CONTOURED APPARENT RESISTIVITY MEASURED IN IN SEPTEMBER 2011, (C) AND (D) ARE THE INVERSE MODELS THAT REPRESENT THE APPROXIMATE ELECTRICAL RESISTIVITY AND DEPTH OF THE GEOLOGIC FORMATIONS FOR THE MAY AND SEPTEMBER DATA SETS RESPECTIVELY, AND (E) IS THE DIFFERENCE PLOT BETWEEN THE TWO PERIODS STARTING FROM MAY 2011 TO SEPTEMBER 2011. 59

FIGURE 3.21. RESISTIVITY DEPTH SLICES FROM 0 TO 17 M FOR MARCH AND APRIL 2011. THE DEPTH RANGES ARE AS FOLLOWS: A) 0-1 M, B) 1- 4 M, C) 4-7 M, D) 7-10 M, E) 10-14, F) 14-17 M. 61
FIGURE 3.22. RESISTIVITY DEPTH SLICES FROM 17 TO 31 M FOR MARCH AND APRIL 2011. THE DEPTH RANGES ARE AS FOLLOWS: G) 17-22 M, H) 22-26 M, I) 26-31 M, J) 31-37 M. 62
FIGURE 3.23. A FENCE PLOT OF THE PROFILES AND CROSSLINES. 64
FIGURE 3.24. ELECTRICAL IMAGE ALONG PART OF PROFILE 15 USING THE SCHLUMBERGER CONFIGURATION. 68
FIGURE 3.25. ELECTRICAL IMAGE ALONG PART OF PROFILE 9 USING THE WENNER ARRAY. 68
FIGURE 3.26. ELECTRICAL IMAGE ALONG PART OF PROFILE 23 USING THE WENNER-SCHLUMBERGER ARRAY. 69
FIGURE 4.1. IMAGE SHOWING SURVEY OF THE PRELIMINARY DATA. 72
FIGURE 4.2. ELECTRICAL IMAGE ALONG LINE 1 FOR THE WENNER ARRAY. (A) IS THE MEASURED CONTOURED IMAGE, (B) IS THE CALCULATED IMAGE FROM THE MODEL, AND (C) IS THE INVERSE MODEL THAT REPRESENTS THE APPROXIMATE ELECTRICAL RESISTIVITY AND DEPTH OF THE GEOLOGIC FORMATIONS. 74
FIGURE 4.3. ELECTRICAL IMAGE ALONG LINE 2A. 75
FIGURE 4.4. ELECTRICAL IMAGE ALONG LINE 3. 76
FIGURE 4.5. ELECTRICAL IMAGE ALONG LINE 1 (REPEATED IN MARCH 2010) 77
FIGURE 4.6. ELECTRICAL RESISTIVITY MONITORING ALONG LINE 1. (A) INITIAL DATA SET AND (B) TIME-LAPSE DATA SET. (C) DIFFERENCE PLOT BETWEEN THE TWO PERIODS. 78
FIGURE 4.7. ELECTRICAL IMAGE ALONG LINE 2 (REPEATED IN MARCH 2010) 79
FIGURE 4.8. THIS IMAGE SHOWS THE SURVEY LINES OF THE TDEM AND MAGNETIC DATA MEASURED BY FUGRO AIRBORNE, SOUTH AFRICA. 81
FIGURE 4.9. THE APPARENT CONDUCTIVITY MAP DERIVED FROM THE TEMPEST Z-COMPONENT DATA. THE DATA PRESENTED IN PPM. PANELS (A) TO (I) REPRESENT WINDOWS 1 TO 9. THE SUBSEQUENT WINDOWS SHOW NOISE. THE POLYGON THAT IS SUPERIMPOSED ON THE GRIDS OUTLINES DAYSPRING SCHOOL. 84
FIGURE 4.10. THE DOTS REPRESENT THE POSITIONS OF THE GROUND TDEM SOUNDING POINTS. THE YELLOW LINE REPRESENTS A SYENITE DYKE WHILE THE PURPLE LINES REPRESENT THE POWERLINES, WITH BOLD REPRESENTING THE BIG POWERLINE. 86
FIGURE 4.11. APPARENT RESISTIVITY IMAGE DERIVED FROM TEMFAST Z-COMPONENT. THE PANELS SHOW RESISTIVITIES DERIVED FROM WINDOW 1(CH01) TO WINDOW 12(CH12). 89
FIGURE 4.12. APPARENT RESISTIVITY IMAGE DERIVED FROM TEMFAST Z-COMPONENT. THE PANELS SHOW RESISTIVITIES DERIVED FROM WINDOW 1 (A) TO WINDOW 20 (J). 90
FIGURE 4.13. THE APPARENT CONDUCTIVITY MAP DERIVED FROM THE TEMPEST Z-COMPONENT DATA OF WINDOW 3. THE MAP SHOWS A RIVER AND SYENITE DYKES SUPERIMPOSED ON IT. 91

FIGURE 4.14. THIS IMAGE SHOWS THE GRAVITY SURVEY STATIONS. THE LINES START FROM LINE 6 TO THE WEST TO LINE 17 TO THE EAST REPRESENTED BY THE DOTS.....94
FIGURE 4.15. BOUGUER GRAVITY DATA DERIVED FROM THE CG-5 IN APRIL 2011 (LEE, 2011). THE DATUM IS WGS 84, THE GRID IS UTM, AND THE ZONE IS 35S. 96
FIGURE 4.16. BOUGUER GRAVITY DATA DERIVED FROM THE CG-5 IN OCTOBER 2011 (LEE, 2011).....97
FIGURE 4.17. THE AIRBORNE REGIONAL MAGNETIC INTENSITY MAP.....101
FIGURE 4.18. THE ZOOMED-IN AIRBORNE MAGNETIC INTENSITY MAP. THE OUTLINE SUPERIMPOSED ON THE MAP IS THE GROUND MAGNETIC GRID. 102
FIGURE 4.19. THIS IMAGE SHOWS THE GROUND-MAGNETICS SURVEY LINES. THE LINES START FROM LINE 6 TO THE WEST TO LINE 17 TO THE EAST REPRESENTED BY THE DOTS. 104
FIGURE 4.20. THE GROUND MAGNETIC MAP OF DAYSPRING SCHOOL. THE MAFIC SILL AND HORNFELS BOUNDARY IS BASED ON THE INTERPRETATION OF GRAVITY DATA (AFTER SEPATO, 2011). 106
FIGURE 4.21. DEUTERIUM AND OXYGEN-18 VARIATION IN WATER SAMPLES FROM DS1 AND DS2.....113
FIGURE 5.1. A MAP SHOWING THE POSITION OF THE BOREHOLES AS WELL AS THE MAFIC SILL BOUNDARY (WHITE) AS INTERPRETED FROM GRAVITY AND RESISTIVITY METHODS. THE UNKNOWN NORTH-SOUTH STRIKING FEATURE (YELLOW) WAS MAPPED BY ELECTRICAL AND MAGNETIC METHODS. 116
FIGURE 5.2. A SCHEMATIC FINAL GEOLOGIC INTERPRETATION OF DAYSPRING SCHOOL FOR THE TOP 45 M. 117

List of Tables

TABLE 3.1. ARRAY CONFIGURATIONS FOR DIFFERENT ARRAY TYPES WITH THEIR MEDIAN DEPTH OF PENETRATION (Z). C1 AND C2 ARE THE CURRENT ELECTRODES WHILE P1 AND P2 ARE THE POTENTIAL ELECTRODES. A IS THE DISTANCE BETWEEN THE POTENTIAL ELECTRODES (AND CURRENT ELECTRODES FOR THE WENNER ARRAY) AND N IS AN INTEGER VALUE. L IS THE TOTAL LENGTH OF THE ARRAY (LOKE, 2001). 23
TABLE 4.1: GENESIS SYSTEM SPECIFICATIONS AS PROVIDED BY FUGRO. 82
TABLE 4.2: TEM-FAST SURVEY SPECIFICATIONS. 87
TABLE 4.3: GENESIS SYSTEM SPECIFICATIONS AS PROVIDED BY FUGRO. 100
TABLE 4.4. MEASURED AVERAGE MAGNETIC SUSCEPTIBILITIES (SEPATO, 2011).....105
TABLE 4.5. THE PHYSICAL PROPERTIES OF BOREHOLES DS1 AND DS2 (AFTER GOBA 2010). 112
TABLE 4.6. ANALYTICAL RESULTS OF THE ISOTOPES OF DEUTERIUM, OXYGEN-18, AND TRITIUM.....113

Chapter 1. Introduction

1.1 General Introduction

Dayspring School is located between S25° 53’ 50” and S25° 54’ 5” latitude, and E27° 27’ 32” and E27° 27’ 45” longitude, ~67 km northeast of Johannesburg (Figure 1.1). The school, which suffers chronic shortage of water, hosts about 100 staff members and pupils. Most of the pupils come from disadvantaged backgrounds and some are orphans and/or living with HIV and/or Aids. The management of the school desires to expand the school but cannot do so because of the shortage of water. The water shortage has worsened over the past 30 years, shown by the drying up of the boreholes scattered within the school property. In about the same period, alien mature bluegum (~20-30 m tall) and yellow wattle (~5-15 m) trees planted along the eastern fence of the school have matured. The purpose of this project was to determine the complex interaction between the plants and structural elements of the various aquifers using geophysical and hydrogeological methods.

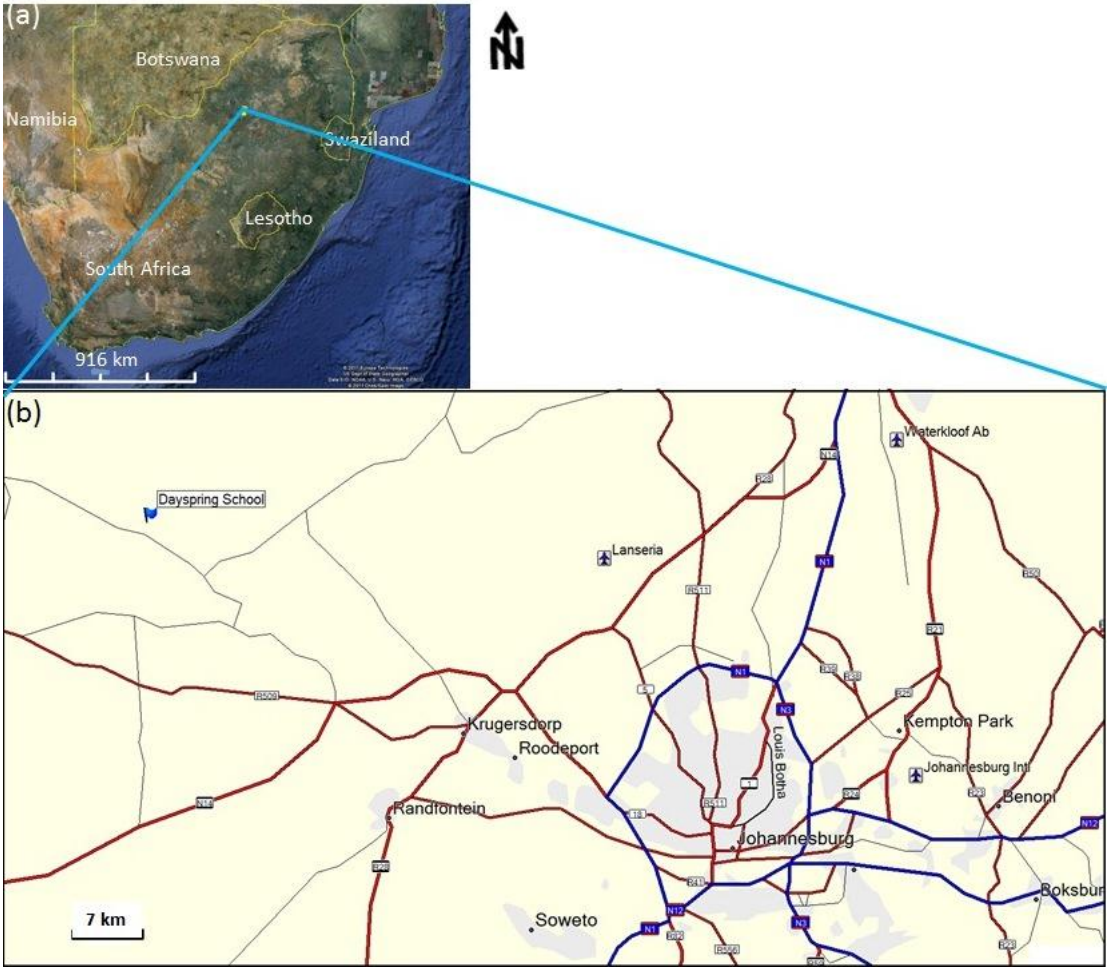

Figure 1.1. Locality map of the study area. (a) Map of southern Africa. (b) The zoomed-in map showing the position of Dayspring School relative to Johannesburg.

The impact of bluegum trees on groundwater has been studied over the years (e.g. Holland and Benyon, 2010; Sikka et al., 2003; Sharda et al., 1998; Calder, 1992; Pohjonen and Pukkala, 1990; Samraj et al., 1988; Sharda et al., 1988). Water-uptake by bluegum trees is also influenced by relief, of which Dayspring is located on relatively elevated terrain. For example, in West Australia, Greenwood et al. (1985) have quantified high rates of evapotranspiration by bluegum trees up to 2700 mm upslope and 2200 mm down slope per 1.5 ha of plantation.

Groundwater uptake by trees is seasonal, so the lateral roots are responsible for water uptake during the rainy season and switches to tap root system in the dry season

(Dawson and Pate, 1996). An example of this observation is found in the work done by Fritzsche et al. (2006), where the groundwater uptake in the wet season was less than the dry season. Moreover, David et al. (1997) studied the transpiration of eight-year-old Bluegum in Portugal where they estimated water-uptake to 0.5-03.64 mm day^{-1} during a water-deficit season for a plantation with a density of 1020 trees ha^{-1}.

Water uptake during the wet season is primarily due to rainfall wetting of the shallow subsurface whereas in the dry season, the trees tap into the water table. Work of Calder (1992) and Benyon et al. (2006) support this observation, where they showed that the annual rainfall was less than the annual transpiration by 61.9% and 73% respectively. If the groundwater uptake continues to exceed the annual rainfall, it is expected that the aquifer(s) may be depleted – under the assumption that the recharge is only from local rainfall.

Clearing of trees, such as bluegum, may yield positive results. Examples from the Thabazimbi area in Limpopo and Pietermaritzburg in Kwazulu-Natal, South Africa have shown that clearing of trees yields a significant rise in water-table level (Le Maitre et al., 1999). But, a limited number of studies in South Africa have focused on interactions between vegetation and groundwater, and where these interactions have been studied, most of the work focused on alluvial aquifers (Le Maitre et al., 1999). There is little direct information on vegetation-groundwater interactions on fractured aquifers, which covers ~90% of aquifer systems in South Africa (Le Maitre et al., 1999). This project will critically examine the effect of invasive plants on possible fractured and lithological-contact aquifers on a local scale.

Integrated geophysical methods have proved to be successful in geological and hydrological surveys (e.g. De Beer and Stettler, 1988; Van Overmeeren, 1981). Several geophysical methods including 3D DC resistivity, time-domain electromagnetic (TDEM), gravity, and magnetics were used to map lithologies, linear features, and distribution of groundwater. Groundwater chemistry was also

incorporated in interpretation of results as well as analysing the chemical evolution of the water.

The most significant result is that better geologic and hydrologic insights have been gained.

1.2 Background

Dayspring had seven boreholes (Figure 1.2), of which five have dried up over the past 30 years. The owner reported the depths of boreholes DS4, DS5, and DS7 as 35 m deep. DS4 dried up over 30 years ago; it only pumped for two weeks, but the water smelled bad. DS5 had greenish water but it has since dried up. DS6 is an old borehole, was blocked, and dried up. The depths of DS3 and DS7 are reported as 80 m deep. DS3 was dry at drilling while DS7 had water, but it has since dried. DS1 and DS2 are the only two boreholes that are producing water. DS1 ~50 m deep but is reported to draw water from a depth of 30 m. DS1 produces clean water that is used for drinking and washing, however, it has a low yield at <1000 l/hour. This is supplemented with rainwater for washing and bathing. DS2 is reported as ~162 m deep but draws water from a depth of 160 m. The school claims that the water is sometimes contaminated with Escherichia coli (E.coli). It is alleged that the water has sulphur smell; hence, it is used for gardening.

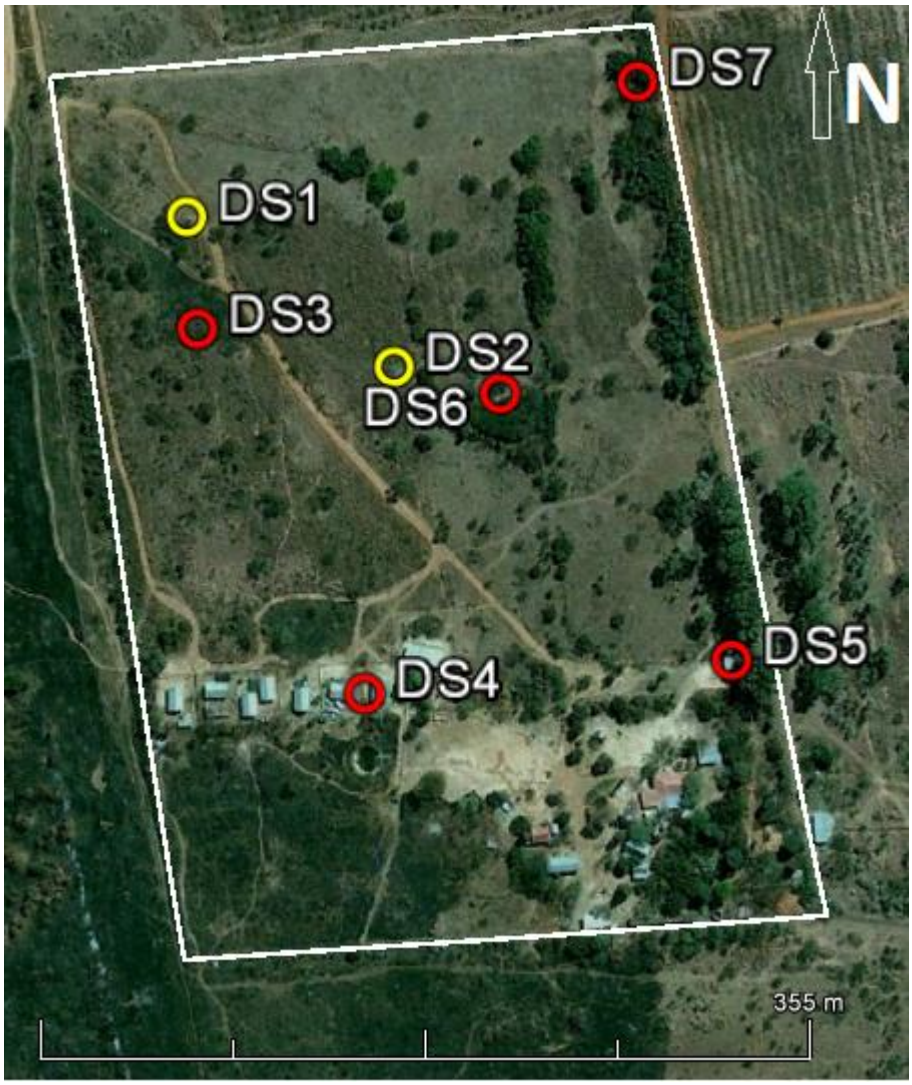

Figure 1.2. A map of the borehole localities at the Dayspring School.

1.3 Aims and objectives

The goals of the study are to:

1. provide a better geologic and hydrologic insight of the school,
2. quantify the effects of bluegum and yellow wattle plants on the local hydrology, and
3. locate wells for clean water and assist with explaining existing contamination.

1.4 General materials and methods

To meet the objectives, several geophysical methods were used. This project involved several honours students. Ngobeni (2009) used DC electrical resistivity at Dayspring School, as an honours project, to investigate the impact of alien tree species on groundwater at Dayspring School. In 2010 two students, Devkurran (2010) and Goba (2010) did gravity and hydrological studies respectively at Dayspring School, but the work of Goba (2010) covered a larger area. In 2011, Lee (2011) and Sepato (2011) completed their honours projects in the study focusing on 4D gravity and ground magnetics respectively. My focus was DC resistivity and TDEM. However, I have integrated all methods in my interpretation.

DC resistivity and TDEM methods were used to map out geology, groundwater, fracture zones, and tectonic features. The gravity method was used to map geology and lithological contacts with the time lapse gravity used to determine groundwater movements. Magnetics was used to map linear features. Hydrogeologic data were used to characterise and distinguish different aquifers. The different data sets were analysed using software packages including Res2dINV (Loke, 2001), Geosoft Oasis Montaj, Surfer (Golden software), and Excel.

1.5 Limitations

It was hoped that the alien trees would be removed in 2010 so that before and after measurements could be made. However, the trees were not removed, which hampered the original plan of work. Lack of 3D resistivity and TDEM inversion software was a challenge. Be as it may, it would have been possible to develop inversion codes, but it was beyond the scope of this dissertation. Thus, the resistivity and TDEM results are limited to 2D and quasi-3D resistivity, and 3D TDEM in raw data because the TDEM data were not inverted to get conductivity depth sections.

Chapter 2. Geological setting and climatic conditions of the study area

2.1 Geology

2.1.1 Regional geology

Previous regional geological studies could not depict with confidence the boundary between shales, slates, hornfels or dolerite (or feldspathic pyroxenite) sills in the proximity of the study area (Geological Survey of South Africa, 1981). The geological map (Figure 2.1) shows that the study area is located on shales, or slates, or hornfels, yet there are outcrops of feldspathic pyroxenite to the north of the study area. A precise delineation of the contact between the different rock units will be a good target for siting boreholes with good yields. A general overview of the regional geology is discussed below.

The Dayspring School is located on the Silverton Formation of the Pretoria Group of the Transvaal Supergroup (2500-2100 Ma) (Eriksson and Clendenin, 1990). The Silverton Formation is characterised by shales, slates, and hornfels and intrusive dolerite sills (2095 Ma) (Eriksson and Clendenin, 1990). There are two syenite dykes, striking north-south, to the west of the school property; and the syenite dyke nearest to the school property is ~50 m to the west. These dykes are younger than the dolerite sills because they crosscut the sills and in some places, they form linear ridges. Carruthers (1990) suggests that in places where the syenite outcrops, the adjacent rock is shale because shale weathers rapidly when compared to the syenite dykes and the dolerite sills.

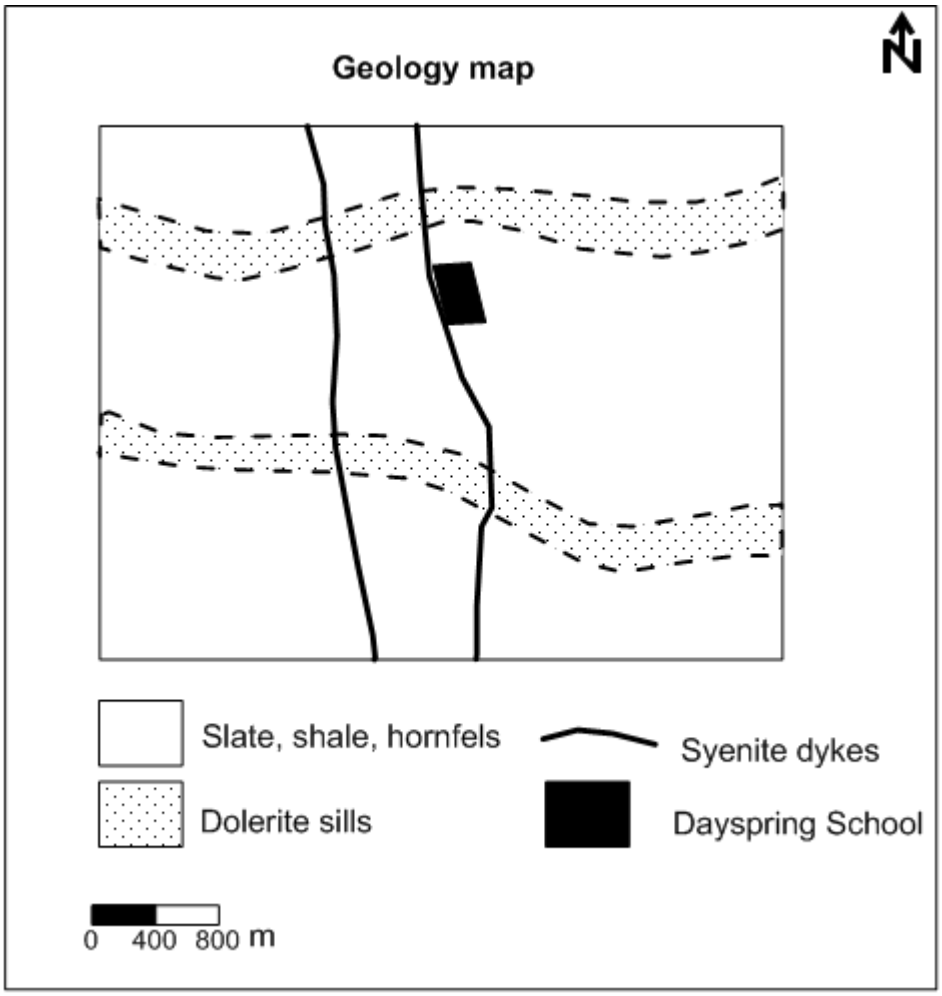

Figure 2.1. A simplified geology map (Geological Survey of South Africa, 1981) of the region showing the position of the study area with the filled polygon.

The Silverton Formation is divided into three members, the Lydenburg Shale Member, Machadodorp Volcanic Member and the Boven Shale member (Button, 1973). Stratigraphically, the Lydenburg Shale Member rests on top of the Machadadorp Volcanic Member while the Machadadorp rests on the Boven Shale Member. The thickness of the Lydenburg Shale Member, on which the Dayspring School is located, ranges from 1 200 to 1 700 m and dip up to 20° towards the center of the Bushveld Complex (Eriksson and Clendenin, 1990; Button, 1973). Thin limestone lenses are present in the top half of the Lydenburg Shale Member (Button, 1973).

The emplacement of the Bushveld Complex (2095 Ma) and intrusion of the related dolerite sills metamorphosed the shales (Eriksson and Clendenin, 1990). The intrusion of the syenite dykes may have metamorphosed the dolerite sills and the metamorphosed shales. The texture of the syenite dykes resembles the Pilanesberg (1250 M.a.) intrusion because of the large crystals (Carruthers, 1990). In fact, Carruthers (1990) suggests that the Pilanesberg magma radiated outward by exploiting zones of weakness. These zones of weakness, faults or fractures, could have been caused by the thermal effect during the emplacement of the Bushveld Complex. Thermal effect during the intrusion of the syenite dykes could have caused fracturing in the adjacent rock.

In areas without outcrop, the soil cover was assumed to be colluvial and was used to infer contacts between the different units. The weathering of shales and mudstones results in grey or creamy-coloured (yellow, orange, pink, or mauve) soils with remnants of the shale being present. The soil formed as a result of dolerite sills is red and gives rise to darker tones on aerial photographs. The hornfels weathers into large blocks and slabs and they usually rest within their residual soils (Button 1973).

2.1.2 Local geology

Racheal Goba, Dr. Michael Jones and Dr. Susan Webb did some geologic mapping at Dayspring School. Though the school is largely covered by soil, there are outcrops of feldspathic pyroxenite to the north and boulders and floats of hornfels (Figure 2.2).

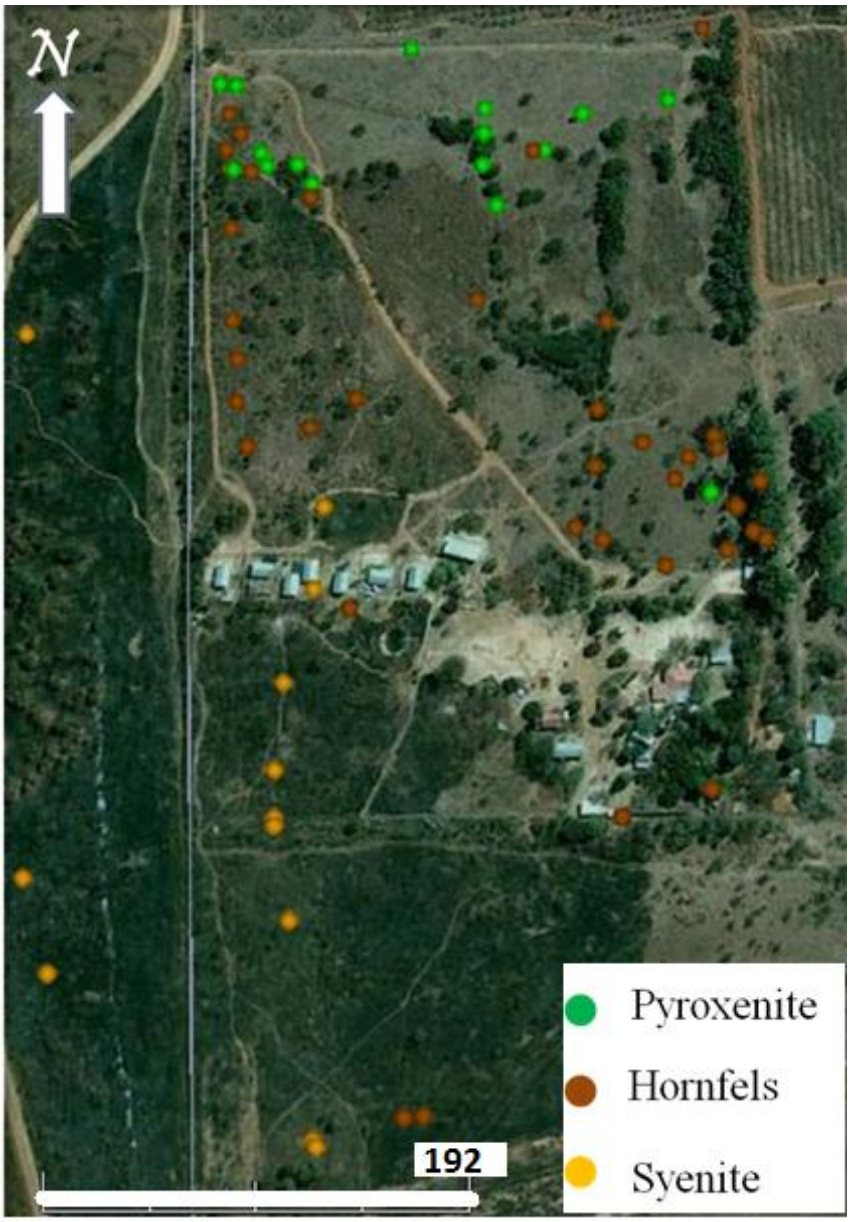

Figure 2.2. The distribution of rock floats, boulders and outcrops at Dayspring School.

2.1.2.1 ***Description of the rocks***

Feldspathic pyroxenite

The weathering surface of the pyroxenite is brown. The fresh surface is coarse-grained and greenish. The minerals on a hand specimen include pyroxene (in large quantity) with some quartz and feldspar. Thin sections of the pyroxenite reveal that

the rock contains zoned clinopyroxene, partially sericitized plagioclase, and interstitial graphic intergrowths of quartz and feldspar (Webb et al., 2011).

Hornfels

The weathering surface of the hornfels is light brown. The fresh rock is fine-grained and black which sparkles by the sunlight.

Thin sections from DS2 chips

Thin sections derived from DS2 chips at 40 m depth (Figure 2.3) reveals that the rock type contains clinopyroxene (in large quantity), olivine, small percentage of plagioclase, biotite (large quantity), and opaque minerals. The plagioclase is intercumulus and interstitial to the pyroxene. There is also green mineral, which is probably serpentine. This rock type is probably a pyroxenite.

2.1.2.2 ***Weathering profile***

The soil and rock chips derived from borehole DS2 reveal a thick regolith of about 35 m (Figure 2.3). The top regolith (0-10 m) looks compact, as there are agglomerates of red soil (average of 20 cm). A photograph of the soil from one of the pits at Dayspring is shown in Figure 2.4. The top regolith shows boulders of the parent rock resting in the residual soil and the reddish color is due to Fe oxide. The soil from 10 to 30 m is loose and light brown. The soil from 30 to 35 m is loose and is grey-brown revealing a transition from the regolith to the bedrock. The chips from 35 to 162 m (except where there are no borehole chips between 120 and 150 m) are fine-grained to very fine-grained revealing different levels of hardness of the mafic sill.

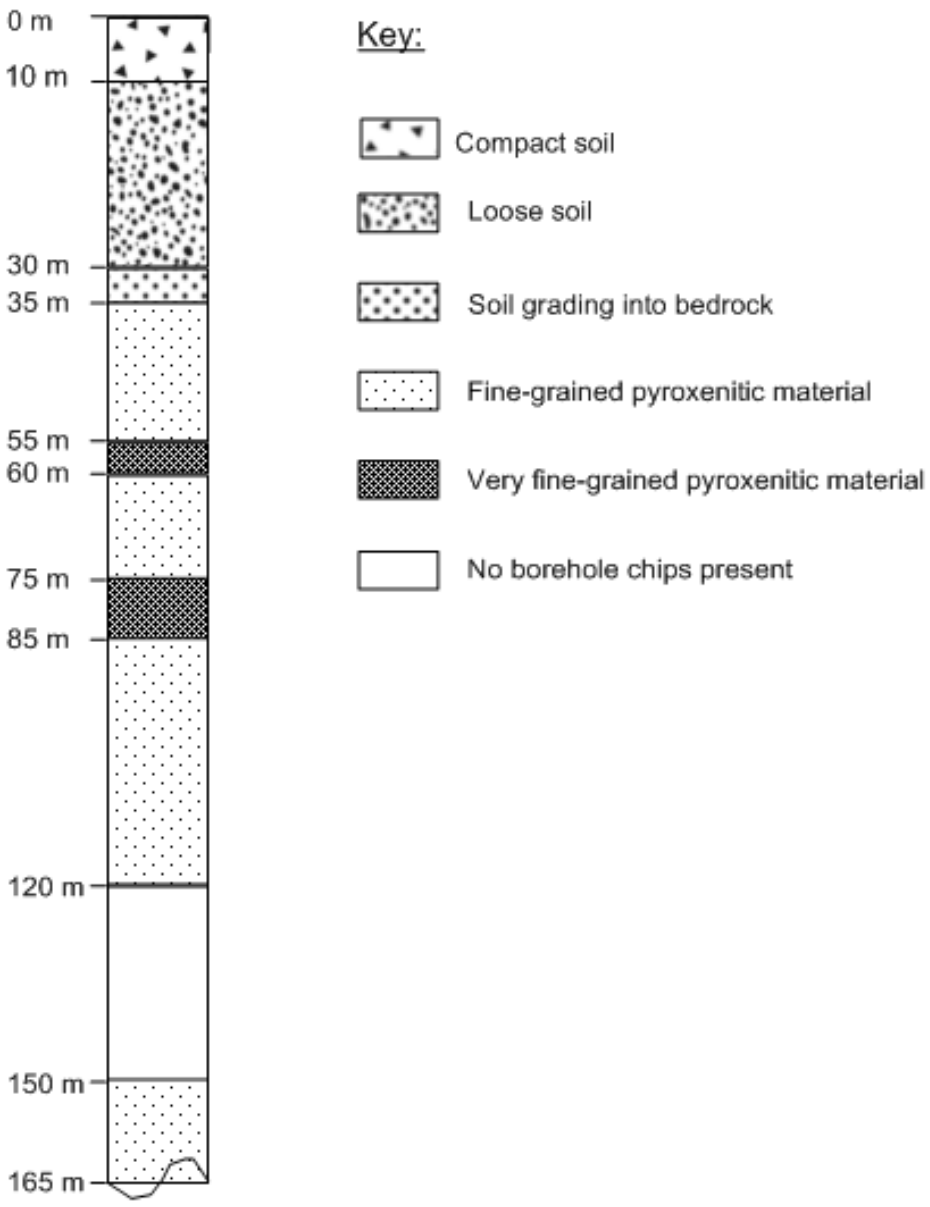

Figure 2.3. Soil and rock chips column from borehole DS2.

Figure 2.4. An example of the top regolith from one of the pits at Dayspring School. The geological hammer can be used for scale.

2.2 Climatic conditions of the study area

The study area falls under the humid subtropical climate. Humid subtropical climates are characterised by hot and wet summers, and dry and cold winters. Temperatures may rise as high as 30 °C in summer and as low as 1.8 °C in winter (Carruthers, 1990). The annual rainfall in the study area varies a lot. For example, in 2007 and 2008, maximums of 381 mm and 798 mm respectively were recorded in one of the farms in the region at the foot of the Magaliesberg quartzite ~10 km away from Dayspring (G. Williams, personal communication, 2012). Sometimes the annual rainfall can go as high as 1102 mm as it did in 2010. From 2007 to 2011, the average annual rainfall of the region was 835 mm. Most of the rainfall is in January while some winters yield absolutely none (Figures 2.5a, 2.5b and 2.5c) though in 2008 the highest rainfall was recorded in March. Sometimes winter rains occur, e.g., rainfall was recorded in June 2011. In summary, spring (August to mid-October), summer (mid-October to mid-February), and autumn (mid-February to April) are wet seasons while winter (May to July) is a dry season.

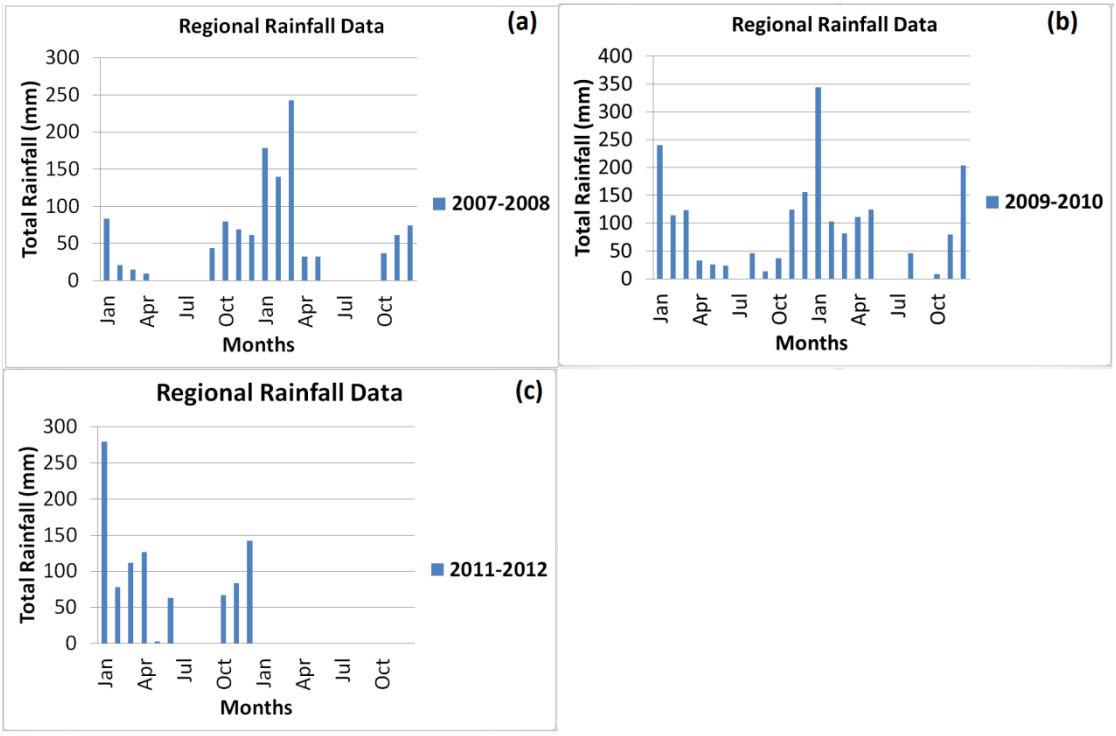

Figure 2.5. Regional rainfall data of the study area representing data measured from January 2007 to December 2011. (a) shows data from January 2007 to December 2008, (b) shows data from January 2009 to December 2010, and (c) shows data from January 2011 to December 2011 (G. Williams, personal communication, January 11, 2012).

Chapter 3. DC Resistivity surveys at Dayspring School

3.1 General introduction

Geophysics relies on the physical property contrasts of the geological formations below surface. Each geophysical method exploits a particular physical property. Some methods are good in exploration of groundwater and minerals, some are good for geological mapping; and others are good for both exploration and geological mapping. The choice of a method depends on the problem that is to be solved and the time, and money available to complete the work. The geophysical methods used in this survey include electrical resistivity, time-domain electromagnetic methods, microgravity, and magnetics. Integration of geophysical methods is the best tool in groundwater geophysics (e.g. De Beer and Stettler, 1988; Van Overmeeren, 1981). My focus was on DC resistivity and I will integrate other methods from parallel studies.

3.2 DC Resistivity surveys

3.2.1 Introduction

A lot of work has been done in South Africa using the resistivity method. Most published work involved deep structure investigations using deep resistivity sounding (e.g. De Beer and Stettler, 1992; De Beer et al., 1991; De Beer and Stettler, 1988; Stettler, Du Plessis and De Beer, 1988; Meyer and De Beer, 1987; Van Zijl and Joubert, 1975; Van Zijl et al., 1970; Van Zijl, 1969). Recent shallow resistivity profiling includes the work of van Schoor (2002). Most recently, time-lapse resistivity studies have been used to study fluid movements including groundwater (e.g. Rosqvist et al., 2003). However, literature has little or no published work on the study area or the region.

The resistivity method exploits contrasts in electrical properties of the subsurface. In crystalline terrains like Dayspring School, groundwater is expected to be found in

joints, weathered layers, faults, fractures and fissures and contacts; and mapping of these features can help in siting wells. The resistivity method has the ability to map these features because of their resistivity contrasts. Current flow in resistive formations depends on pore fluids and their content. This phenomenon allows the resistivity method to map groundwater and geological structure. A significant drop in resistivity of the weathered rock, for example, signals a change in moisture and/or its contents (e.g. Total dissolved solids).

The geology of the area was poorly mapped due to soil development; hence, successful boreholes could not be sited with confidence. The hydrological data from previous studies were too sparse to be conclusive of the hydrology of the study area. The impact of invasive plants was known from literature and was suspected to contribute to the continuing water problems.

The purpose of DC resistivity investigations was to monitor groundwater movement and to map suitable places for drilling wells which will produce clean water. To achieve this, the resistivity method was used to map the following: (1) geological structure, (2) moisture occurrence within the subsurface, and (3) the effect of water withdrawal. I used the Wenner alpha array to collect preliminary data in September 2009 and March 2010 and the Wenner-Schlumberger array in August 2010. In April, May, September, and October 2011, I used the Wenner-Schlumberger and the dipole-dipole arrays on east-west profiles, and only the Wenner-Schlumberger array on the north-south profiles.

The most significant outcome is that places with a potential for groundwater occurrence have been identified.

3.2.2 Basic principles of the DC resistivity method

3.2.2.1 Data acquisition

To make a measurement, the resistivity meter injects current into the subsurface using two current electrodes. The propagation of the electric charges, which are responsible

for current, depends on the geoelectric properties of the media (Lowrie, 2007; Burger et al., 2006; Telford et al., 1990). The resistivity meter measures the potential difference using two potential electrodes. The potential drop between the potential electrodes is related to the resistivity of the geologic formation between them.

The resistivity meter then calculates the apparent resistivity from the sum of volumetric contributions from the constituent layers below the subsurface, which is taken to be at a depth that Roy and Apparao (1971) define to be that depth that a thin horizontal layer below the surface would contribute significantly to the total measured signal. However, the inversion software (Loke, 2001) that was used for inverting the resistivity data has adopted the investigation depth that has been defined by Edwards (1977) as the median depth. The median depths of the different arrays used are as follows: Wenner—0.17L, Schlumberger—0.19L, and Dipole-dipole—0.25L, where L is the distance between the two furthest electrodes. The resistivity meter used the following equation to calculate the apparent resistivity:

$$\rho = \frac{\Delta V}{i}\left(\frac{2\pi}{\frac{1}{r_1}-\frac{1}{r_2}-\frac{1}{r_3}+\frac{1}{r_4}}\right) \quad (1)$$

where ρ is the apparent resistivity, ΔV is the potential difference, i is the current, and the term in the parentheses is the geometric factor . Geometric factors vary depending on the array type, i.e., the number and arrangement of current and potential electrodes. The array types that were used in this survey have the following geometric factors: Wenner—$2\pi a$, Schlumberger—$\pi n(n+1)a$, and dipole-dipole—$\pi n(n+1)(n+2)a$, where a is the distance between any two successive electrodes and n is the distance between current and potential electrodes (Lowrie, 2007; Burger et al., 2006; Loke, 2001; Telford et al., 1990).

The investigation of resistivity variations as a function of depth is called sounding while the investigation of resistivity variations, at the same depth, as function of lateral distance is called profiling (Kaufman and Anderson, 2010; Telford et al., 1990). Resistivity data are a convolution of geometric factor or array typed used,

geologic information and noise (Barker et al., 2001; Barker and Moore, 1998; Loke and Barker, 1995).

3.2.2.2 **Inversion**

The Res2dinv (Loke, 2001) inversion software was applied to remove noise and geometric factor from the measured signal. The inversion produces a model iteratively that best fits the measured data by applying mathematical algorithms. The software minimizes the difference between the calculated and measured apparent resistivity values by means a of least-squares algorithm (Constable et al., 1987; Lines and Treitel, 1984) given by

$$(\boldsymbol{J^T J} + \lambda \boldsymbol{C^T C})\boldsymbol{p} = \boldsymbol{J^T g}, \quad (2)$$

where $\boldsymbol{J}$ is the Jacobian matrix of partial derivatives, $\boldsymbol{C}$ is the smoothness filter, λ is the damping factor, $\boldsymbol{p}$ is the correction vector, and $\boldsymbol{g}$ the misfit vector between the measured and calculated data (Loke, 2001).

The software (Res2dinv) divides the subsurface into a grid of rectangular blocks or cells with respect to a specified discretization. It then assigns starting resistivity values of a homogeneous earth model into these cells by means of a forward modeling algorithm assuming that the subsurface resistivity did not vary within the cells and in the orthogonal direction (Loke, 2001; Loke and Barker, 1995; de Groot-Hedlin and Constable, 1990; Sasaki, 1989). The resistivity of a starting homogeneous earth model is calculated by taking the average of the logarithm of the measured apparent resistivity data (Sasaki, 1989). The choice of logarithmic resistivity and apparent resistivity is to reject completely negative values and to account for measurement error (Sasaki, 1989). The starting model of homogeneously resistive earth is calculated using the following equation

$$\chi_0 = \frac{1}{n}\sum_{i=1}^{n} \psi_i \, , \quad (3)$$

where ψ_i is the logarithm of the measured apparent resistivity values, and n is the number of data points (Loke and Barker, 1995).

The software then calculates the Jacobian matrix of partial derivatives for the particular array used. The partial derivatives are precalculated and stored in a data file. To calculate the partial derivatives, the software solves a double integration of the following equation

$$\frac{\partial V}{\partial \rho} = \frac{I_s}{4\pi^2} \int_{z_1}^{z_2} \int_{x_1}^{x_2} F_y \, dx \, dz \,, \tag{4}$$

where V is the potential, ρ is the resistivity, I_s is the point-current source located at $\mathbf{x_s}$, x is along the profile, and z is depth (Loke and Barker, 1995). F_y is given by

$$F_y = \int_{-\infty}^{+\infty} \frac{x(x-a)+y^2+z^2}{(x^2+y^2+z^2)^{3/2}[(x-a)^2+y^2+z^2]^{3/2}} dy \,, \tag{5}$$

where a is the position of the potential electrode (Loke and Barker, 1995).

The software then solves the least-squares to determine the correction vector $\boldsymbol{p_0}$ such that the estimate resistivity $\boldsymbol{\chi_1}$ of the cells (Loke and Barker, 1995) is given by

$$\boldsymbol{\chi_1} = \boldsymbol{\chi_0} + \boldsymbol{p_0} \,. \tag{6}$$

The software (Loke, 2001) compares the measured and calculated data, and iteratively minimizes the misfit between the two data sets by means of least-squares algorithm, either in a smooth manner (de Groot-Hedlin and Constable, 1990; Sasaki, 1989) or robust manner (Claerbout and Muir 1973). The model structure is adjusted automatically by varying the resistivity of the model cells until a satisfactory misfit was achieved, i.e., the difference between the measured and calculated data converged (Loke, 2001; Loke and Barker, 1995; de Groot-Hedlin and Constable, 1990; Sasaki, 1989).

The smoothness-constrained least-squares algorithm minimises the sum of squares of the spatial changes in the model and the data misfit (Loke et al. 2003). The smoothness-constrained least-squares solution is given by

$$(\mathbf{J}_i^T \mathbf{J}_i + \lambda_i \mathbf{C}^T \mathbf{C})\Delta \mathbf{p}_i = \mathbf{J}_i^T \mathbf{g}_i - \lambda_i \mathbf{C}^T \mathbf{C} \mathbf{p}_{i-1}, \quad (7)$$

where $\boldsymbol{J_i}$ is the Jacobian matrix of partial derivatives, $\boldsymbol{C}$ is the smoothness filter, $\lambda_i$is the damping factor, $\boldsymbol{g_i}$ the misfit vector between the measured and calculated data $\Delta \boldsymbol{p_i}$ is the change in model parameters for the ith iteration and $\boldsymbol{p_{i-1}}$ is the model parameters vector for the previous iteration (Loke et al. 2003). The smoothness-constrained least-squares algorithm is well suited for geology that shows smooth transition (Loke et al. 2003), such as transition between weathered rock and bedrock. If the subsurface geology has sharp boundaries, such as intrusive dykes, then the smoothness-constraint algorithm tends to smear out the boundaries and as a result, the inversion either gives resistivities that are too low or too high. If the geology has sharp boundaries, then the robust least-squares algorithm, which minimizes absolute values of the data misfit, produces optimal models (Loke et al. 2003). The robust least-squares is given by

$$(\mathbf{J}_i^T \mathbf{R_d} \mathbf{J}_i + \lambda_i \mathbf{C}^T \mathbf{R_m} \mathbf{C})\Delta \mathbf{p}_i = \mathbf{J}_i^T \mathbf{R_d} \mathbf{g}_i - \lambda_i \mathbf{C}^T \mathbf{R_m} \mathbf{C} \mathbf{p}_{i-1}, \quad (8)$$

where $\boldsymbol{R_d}$ and $\boldsymbol{R_m}$ are weighted matrices that give the model parameters and data misfit approximately equal weights in the inversion process (Loke et al. 2003).

Resistivity models, just like other geophysical methods, are not unique. That is, a different combination of the model parameters, e.g. resistivity and layer thickness, can produce similar inversion outcome because inverted data contain components which cannot be explained in geologic terms (Lines and Treitel, 1984) (e.g. Constable et al., 1987). A forward modeling program (Res2dmod) (Loke, 2001) was used to explore some of the possible scenarios of the shallow subsurface at Dayspring School. The test models assisted in removing some of the ambiguities in the inverted measured data.

3.2.2.3 ***Advantages and disadvantages of the arrays used***

The arrays that were employed were carefully chosen based on time available, depth of exploration, resolution, geologic target to be imaged, and signal strength. The signal strength is inversely proportional to the geometric factor, i.e., the larger the distance between the outside electrodes, the weaker the signal. The Wenner alpha, the Wenner-Schlumberger, and the dipole-dipole are the commonly used arrays and they were all used in this study. Table 3.1 summarizes the array configurations and depths of exploration for the different array types.

The Wenner alpha

The Wenner alpha array is insensitive to geologic and electric noise. It is the fastest but has low resolution and low depth range (about 1/6 of the maximum current electrode spacing). The Wenner alpha is suitable for mapping vertical changes, and relatively poor in mapping horizontal changes (Loke, 2001).

The dipole-dipole

The dipole-dipole array has poor signal strength for large dipole pair separation between the current and potential dipoles. It has the highest resolution and a depth range of about 1/4 the maximum distance between the current electrode (C1) and potential electrode (P2). The dipole-dipole array is good in mapping vertical structures and poorer in mapping horizontal structures because it most sensitive at the dipoles (current and potential) (Loke, 2001).

The Wenner-Schlumberger

The Wenner-Schlumberger has lower signal strength (i.e., lower resistance to geologic and electric noise) than the Wenner array but higher than the dipole-dipole. It has intermediate resolution between the Wenner and the dipole-dipole arrays, and has an exploration depth of about 1/5 of the distance between the current electrode (C1) and potential electrode (P2). The Wenner-Schlumberger array is moderate in mapping vertical and horizontal structures. The Wenner-Schlumberger is a good compromise where both vertical and horizontal structures are expected (Loke, 2001).

It is worth noting that the depth estimates are strictly valid for a homogenous earth, and therefore may be different if there is a large contrast in resistivity between any two layers of geologic formations. A conductive overburden may reduce the depth of penetration since the current would primarily flow in this layer in which case larger electrode spacing maybe necessary.

Table 3.1. Array configurations for different array types with their median depth of penetration (**z**). C1 and C2 are the current electrodes while P1 and P2 are the potential electrodes. **a** is the distance between the potential electrodes (and current electrodes for the Wenner array) and n is an integer value. **L** is the total length of the array (Loke, 2001).

Array type	**Configuration**	**n**	**z/L**
Wenner	**C1 a P1 a P2 a C2**		0.173
Dipole-dipole	**C1 a C2 na P1 a P2**	1	0.139
		2	0.174
		3	0.192
		4	0.203
		5	0.211
		6	0.216
Wenner-Schlumberger	**C1 na P1 a P2 na C2**	1	0.173
		2	0.186
		3	0.189
		4	0.190
		5	0.190
		6	0.190

3.2.2.4 **Interpretation principles**

Knowledge of resistivity of local lithologies is important in the interpretation of resistivity data. Figure 3.1 gives such information, however, it should be noted that the resistivities given in the table are laboratory values and tend to underestimate in-

situ resistivity measurements (e.g. Palacky, 1988). As shown in Figure 3.1, the uppermost layer of weathered igneous rock is a duricrust and has the highest resistivity in the weathered zone. The mottled zone in weathered metamorphic rocks has the highest resistivity in the weathered zone. The saprolite has the lowest resistivity in the weathered zone. A detailed discussion of the different weathering profiles can be found in Anand (2005).

The geology of Dayspring School has already been discussed, where Bushveld-age sills and hornfels are expected. A regolith of thicknesses of over 35 m are expected. The weathering profile developed over mafic rocks (e.g., pyroxenite) comprises (from top to bottom): a clayey ferruginous layer, clayey layer, saprolitic layer, fractured bedrock, and bedrock (Colin et al., 1990). However, it is difficult to place with confidence the horizon boundaries of these layers from the soil profile that came from borehole DS2, except for the top 10 m of the hard ferruginous layer. As shown in Figure 3.1, saprolites are the more conductive of the weathered profiles for both igneous and metamorphic rocks. The resistivity of saprolite is expected to be less than 500 Ω·m since Palacky (1988) has given a bracket of typical in-situ resistivities of fresh igneous rocks to vary between 500 and 1000 Ω·m (e.g. an in-situ fresh diabase resistivity was recorded at 450 Ω·m (Palacky, 1988). In fact, Acworth (2001) argues that saprolite has resistivities ranging from 30-300 Ω·m, while the fractured bedrock ranges between 300 and 600 Ω·m.

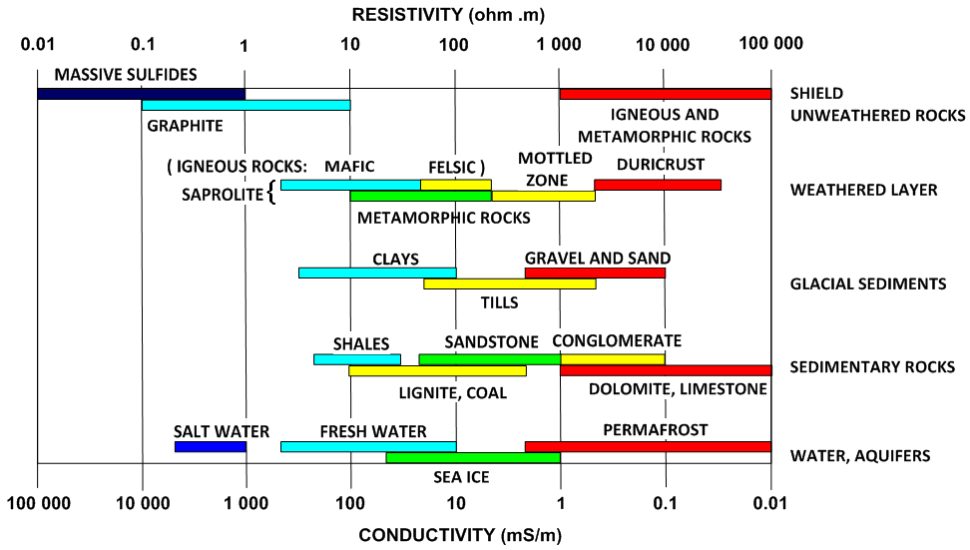

Figure 3.1. Typical range of resistivities and conductivities of geologic materials; after Palacky (1988)

In 2D electrical resistivity, 3D geology can complicate the interpretation of resistivity data. A survey line that is parallel to a steep contact may result in distortions in the lower section of the model obtained (Loke, 2001). Metallic objects such as metallic poles for fences, fences that are slightly buried in the soil, and buried metallic pipes can contaminate resistivity data with noise. Buried pipes, especially, can complicate the interpretation of resistivity models (Vickery and Hobbs, 2002). Hence, test models were necessary in understanding some of the inversion results.

Forward modeling

I used forward models to predict probable geologic features to help with survey design, array layout, and to test anomaly detectability for possible earth models and realistic physical properties (e.g. resistivity and layer thicknesses). The models were created with the Res2dmod software (Loke, 2001), and were exported into Res2dinv so that inversion could be performed. Some people (e.g. Loke, 1999; Loke and Barker, 1995) contaminate the data to be exported into the inversion program with up to 5% Gaussian random noise, which I tried, but data were noisier than the field measured data; hence no Gaussian random noise was added in the exported data. The number of iterations was determined by setting the convergence limit of 1%.

The test models that were looked at are the buried pipe, layered earth with lateral inhomogeneity, and time-lapse resistivity. The buried pipe model was chosen because Dayspring itself and the surrounding area has been inhabited for years and has been used for farming. While modern irrigation pipes are made from plastic, in the past they were often metallic. Hence, old pipes may be present on the property. The layered earth with lateral inhomogeneity was chosen because Dayspring is on hard-rock environment where layers of weathering horizons and fractures are expected, hence the fracture model was chosen. Inhomogeneities are expected because of preferential weathering; hence, boulders and water filled fractures in the bedrock are expected. The time-lapse model was chosen to see the feasibility of the method since Kim et al. (2009) and Loke (1999) suggested that inversion of noisy data caused by measurement error may result in artifacts that could be created by the software during inversion.

Buried pipe test model

A model of buried conductive pipe (Figure 3.2) was created, using the Wenner-Schlumberger array, with almost similar specifications as in Vickery and Hobbs (2002), and produced an inversion model with two lobes of low resistivity on either side of the pipe, and a high resistivity directly on top of the pipe (Figure 3.3). The pipe was buried at 3.6 meter, had a diameter of ~ 0.8 m, and was placed centered laterally at the 18 m mark. The inversion model did not honour the shape of the pipe. The depth of burial for the pipe was then reduced to 1.5 m while the diameter remained almost the same size. The size of the pipe changed because top cells of the forward model program are shorter than the subsequent lower cells. The inversion model produced a model with two lobes of low resistivity centered at 11 and 24 m marks, slightly higher than the resistivity at the center of the pipe at 18 m mark (Figure 3.4). Again, the inversion did not honour the shape of the pipe. When the contrast was reduced from 1:100 to 10:100, the resistivity of the outside lobes increased while the middle lobe honoured the shape of the pipe (Figure 3.5). The

symmetric signature about the vertical axis of the center of the pipe is a common factor in all the models.

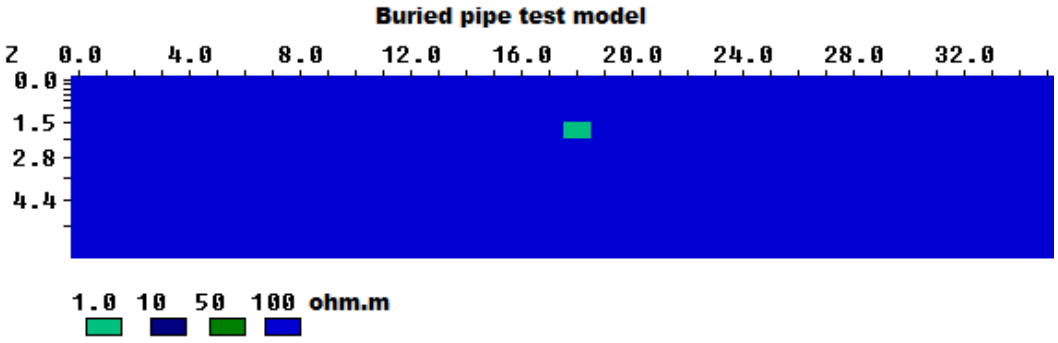

Figure 3.2 Test model with small rectangular block.

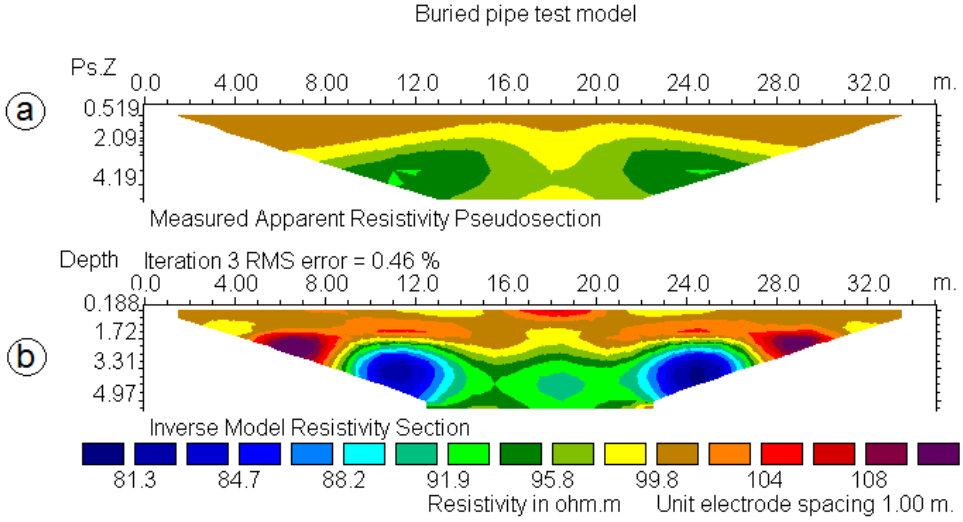

Figure 3.3 Model of synthetic metallic pipe buried at 3.6 m. (a) Apparent resistivity due to a low resistivity prism. (b) Inversion model of the synthetic metallic buried pipe.

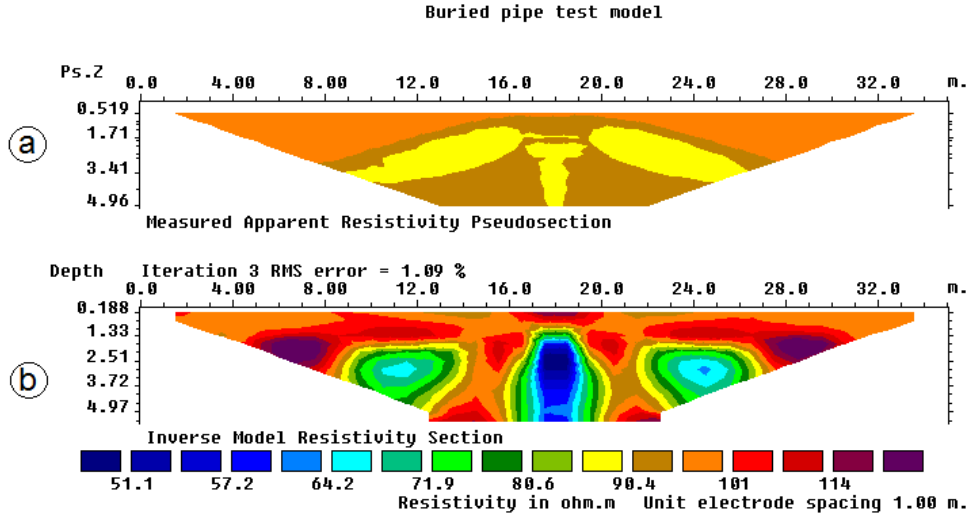

Figure 3.4. Model of synthetic metallic pipe buried at 1.5 m. (a) Apparent resistivity due to a low resistivity prism. (b) Inversion model of the synthetic metallic buried pipe.

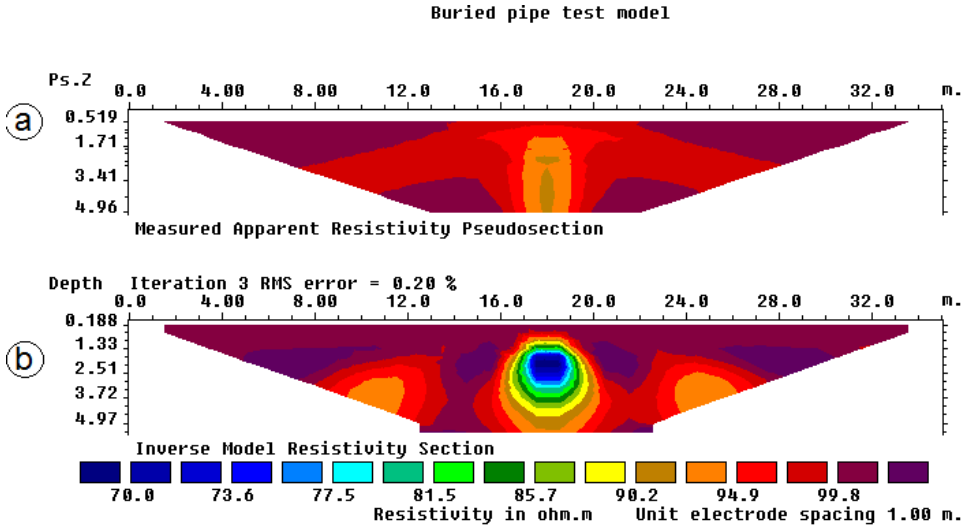

Figure 3.5. Model of synthetic metallic pipe buried at 1.5 m with the resistivity contrast reduced from 1:100 to 10:100. (a) Apparent resistivity due to a low resistivity prism. (b) Inversion model of the synthetic metallic buried pipe.

Layered earth with lateral inhomogeneity test model

Figure 3.6a shows layered model with high (1000 Ω·m) resistivity prisms between the surface and a depth of 20 m, and low (50 Ω·m) resistivity prisms between a depth of 20 and 25 m. The top layer has a resistivity of 300 Ω·m while the bottom layer has

a resistivity of 1000 Ω·m. The high resistivity prisms simulate boulders in the regolith while low resistivity prisms simulate water in fractured and fissured bedrock. Figure 3.6b shows the pseudo-section of the forward model, which shows little information about the lateral inhomogeneity of the model. Figure 3.6b shows the result of the inversion and clearly depicts most of the shallow resistive prisms; however, their resistivities and sizes have been underestimated. Similar results were obtained by Loke and Barker (1995). This phenomenon highlights the fact that the inverted images underestimate dimensions and the resistivity of an inhomogeneous subsurface electrical boundaries.

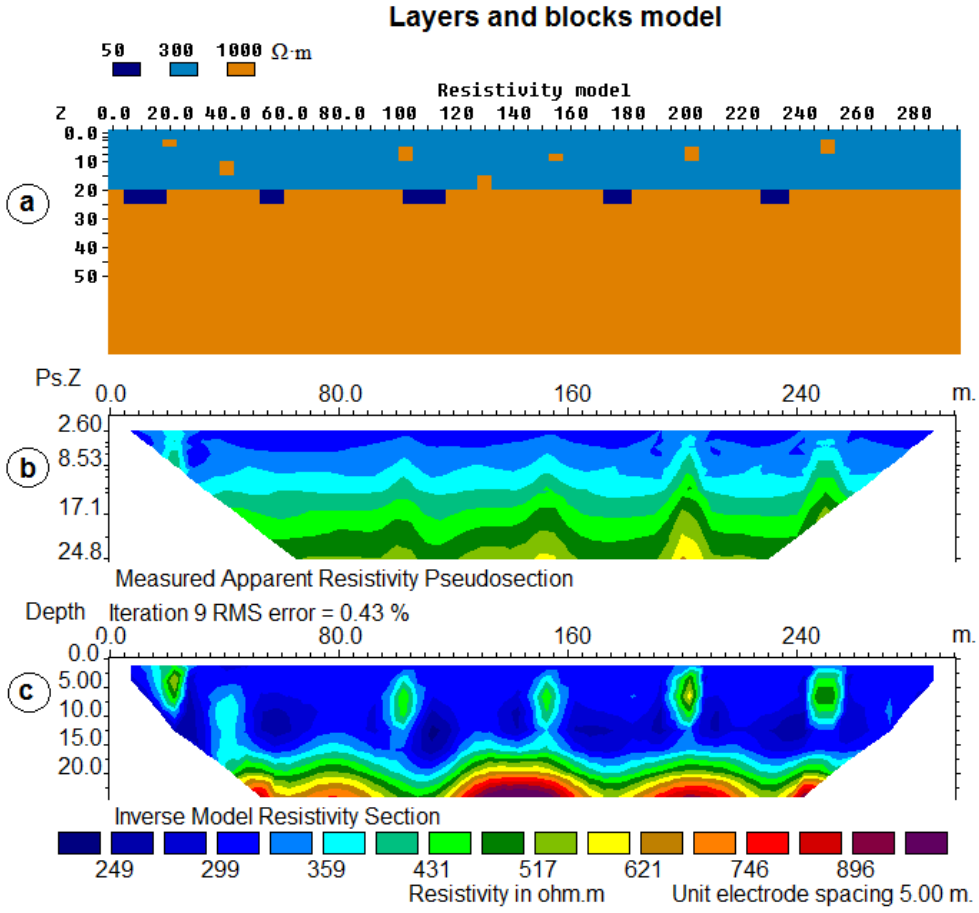

Figure 3.6. A 2D two-layer model with low and resistivity prisms. (a) is the actual model, (b) the pseudo-section of the forward model, and (c) the inverse model for the Wenner-Schlumberger array.

The smooth inverse model recovers the depth horizontal interface at $\sim 20\ m$. Though the robust constraint inversion would have produced better results, the choice of smooth model was based on the idea that gradational changes on interfaces were expected at Dayspring School; therefore, it was logical to see how subsurface inhomogeneities affect the smooth inverse model.

Fracture test model

Figure 3.7a shows a model of a conductive fracture with its top at a depth of 20 m; it is the thinnest (11 m) fracture model that can be detected successfully with the Wenner-Schlumberger array at this depth. The model is based on the borehole chips that came from DS2 which show that the regolith is ~30 m thick; hence, a fracture may be expected below a depth of 20 m owing to the crystalline rocks at Dayspring. The Wenner-Schlumberger array was chosen because this particular array would be used to collect data at Dayspring School, though the Wenner alpha and the dipole-dipole arrays would be used to confirm anomalous features. The inverse model (Figure 3.7b) shows a circular low resistivity above the fracture between a depth of 5 and 10 m, which shows lateral extent to the right and to the left. The symmetry about the fracture and the depression of resistivity layers reveal the position of the fracture. Similarly, a zone of lithological contact with similar thickness as the fracture model and buried below a 20 m thick overburden would be detectible, but the image would not be symmetric about the contact zone. The smooth inverse model recovers the depth horizontal interface at $\sim 20\ m$.

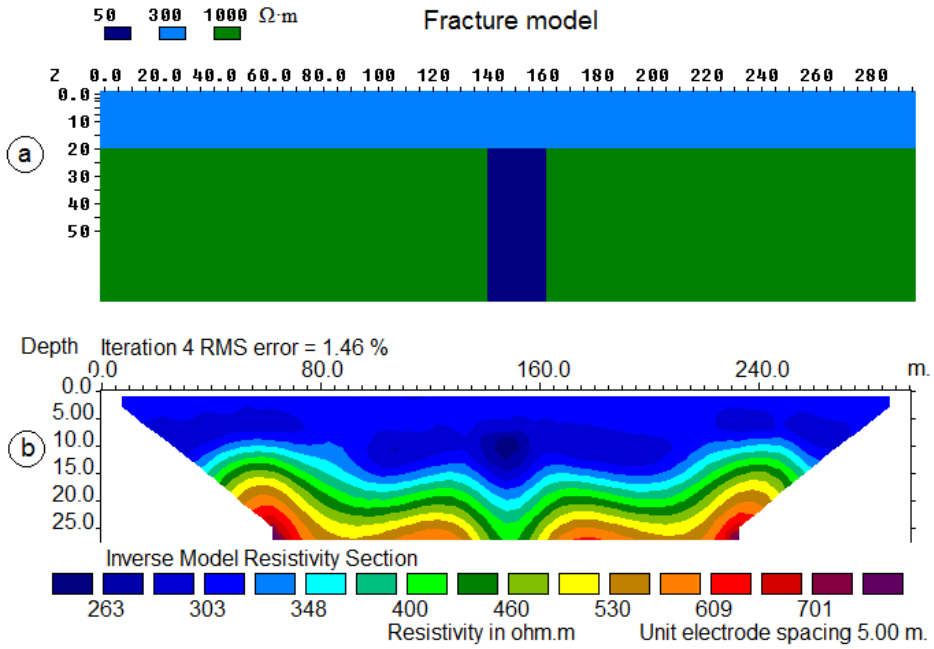

Figure 3.7. A 2D two layer model of wide (11 m) fracture below a thick (20 m) overburden. (a) is the actual model, and (b) is the inverse model for the Wenner-Schlumberger array.

Time-lapse test models

A time-lapse forward model was also performed to take note of artifacts (Kim et al., 2009; Loke, 1999) that could be created by the software during inversion if the data are noisy because of measurement error. The data were not contaminated with random noise because noise would mask the artifacts which were an important aspect of this exercise. Figure 3.8 shows the time-lapse model. Figure 3.8a is the actual model of the initial data set. The prisms were added to complicate (Loke, 1999) the inversion as it is expected that inversion of the real data will be complicated owing to high resistivity boulders in the regolith (of lower resistivity).

Figure 3.8b shows the time-lapse resistivity model after the top and the bottom layers of the initial (Figure 3.8a) data set were increased by 15 and 5% respectively. This model simulates a layer of top soil that dries quicker than the underlying weathered rock because of groundwater withdrawal. This effect can influence resistivity

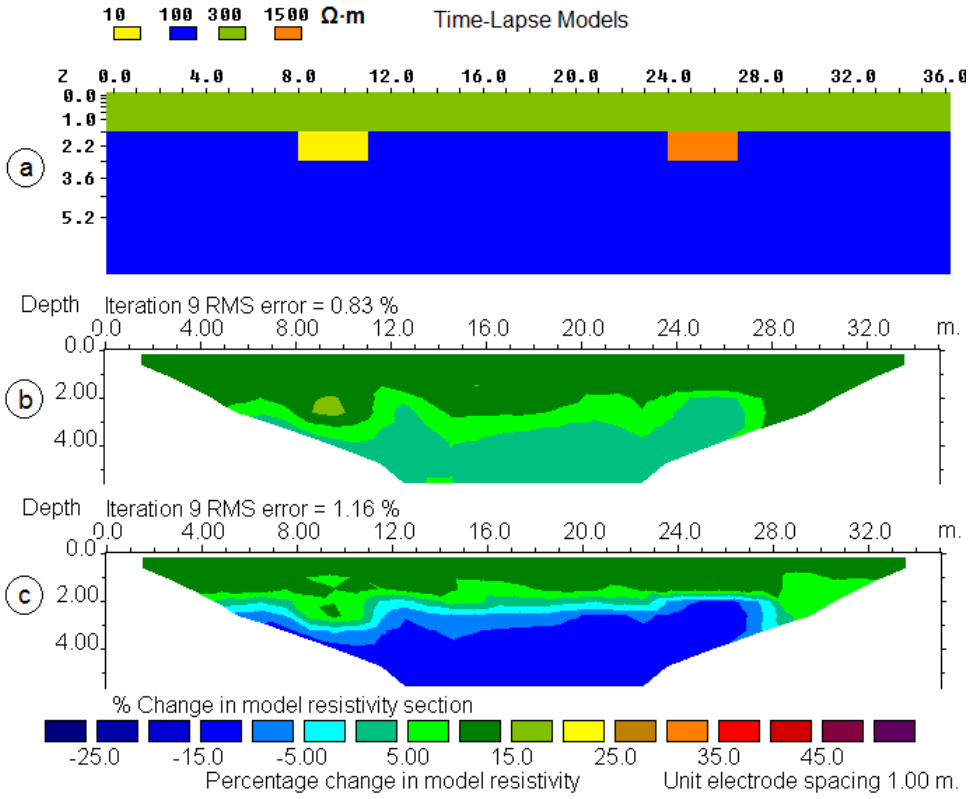

Figure 3.8. Synthetic time-lapse resistivity inversions. (a) The actual model for the initial data set with two prims of low (10 Ω·m) and high (1500 Ω·m) resistivity. (b) Inversion model after the resistivity of the top and bottom layers were increased by 15 and 5% respectively, while the resistivity of the prisms remained unchanged. (c) Inversion model after the resistivity of the top layers was increased by 15% and the resistivity of the bottom was decreased by 5%, while the resistivity of the prisms remained unchanged.

measurements with time. The results show that the changes in resistivity can be imaged though the prisms show changes in the time-lapse model owing to a complicated inversion caused by the size (of the prisms) and resistivity contrast with respect to the background resistivity.

As water migrates downwards, the soil dries up while the weathered rock gets wet. This effect results in an increase in the resistivity of the soil and a decrease in the resistivity of the weathered rock. In an attempt to simulate this condition, the resistivity of the top layer in the initial (Figure 3.8a) data set was increased by 15%

and the bottom layer was reduced by 10% while the prisms remained at constant resistivities. Figure 3.8c shows the subsequent percentage difference plot. Again, the time-lapse image (Figure 3.8c) shows that the changes could be imaged successfully.

The time-lapse results have shown that if the data are not noisy, the temporal resistivity variations can monitored using DC resistivity method.

3.2.3 Materials and methods

3.2.3.1 **Description of the equipment and materials employed.**

Data were acquired using the ARES Resistivity and IP Automatic system. The system comes with the following: five multi-electrode cables with eight take-outs at 5.5 m, 45 stainless steel electrodes, hammers, and O-ring rubber bands. It uses up to 200 electrodes in a single array. The transmitter current output can go as high as 2A while the voltage ranges between 10-550 V. The transmitter has a precision 0.5%. The receiver, which is built-in has an input impedance of 20 MΩ; input voltage range of 5V, mains frequency filter of 50-60 Hz, and a precision 0.1%. It uses a 12 V battery for power source in the field and has an AC power adapter for office use. Supported configurations for 2D and 3D are Wenner, Schlumberger, dipole-dipole, pole-dipole and reverse; pole-pole, and user defined configurations. It can perform vertical electrical sounding (VES), induced polarization (IP) and SP measurements. The formants that the instrument can output data include Resd2INV, Res3dINV, and Surfer.

Data acquisition in 2011

The cable sections were connected in series to make a line of 214.5 m. Each cable section had 8 take-outs at 5.5 m (which was used as the electrode spacing, but note that the electrode spacing need not to be the same as the take-out spacing), and the take-outs were attached to electrodes which were half buried in the ground. The one end of the line of cable-sections was attached to the ARES system through a T-piece, which is useful for roll-along surveys. To do a roll-along, the first cable section was moved to the end of the cable-sections where it was connected to the last cable after

the resistivity meter would have prompted for such an action. The resistivity meter checked ground contacts before it could begin with the measurements, and where contact was poor, the electrode was saturated with water to improve ground contact. A stack of four measurements and a standard deviation of 1% were selected such that if the standard deviation exceeded 1%, the resistivity meter would re-run the measurement until a standard deviation than < 1% was achieved. The duration of the measurement depended on the type of array, stacking number, and the standard deviation, hence a lower stack was opted to minimize time.

Data were collected in April and May 2011, towards the end of the rainy season, and in September and October 2011, towards the end of the dry season. The repeat survey lines were coinciding with initial lines unless the initial line was extended in the repeat measurements (Figure 3.9). The initial data sets were measured in the following days of 2011: profile 7 on 21 April, profiles 15 and 17 on 22 April, profile 9 on 23 April, profile 11 on 24 May, profile 13, crosslines 12 and 15 on 24 May, and crosslines 10,17, and 19 on 25 May. The time-lapse data sets were measured on the following days of 2011: profile 7 on 11 September, profiles 13, 15 and 17 on 22 September, profiles 9 and 11 and crossline 12 on 13 September, and crosslines 10, 15, 17 and 19 on 14 September.

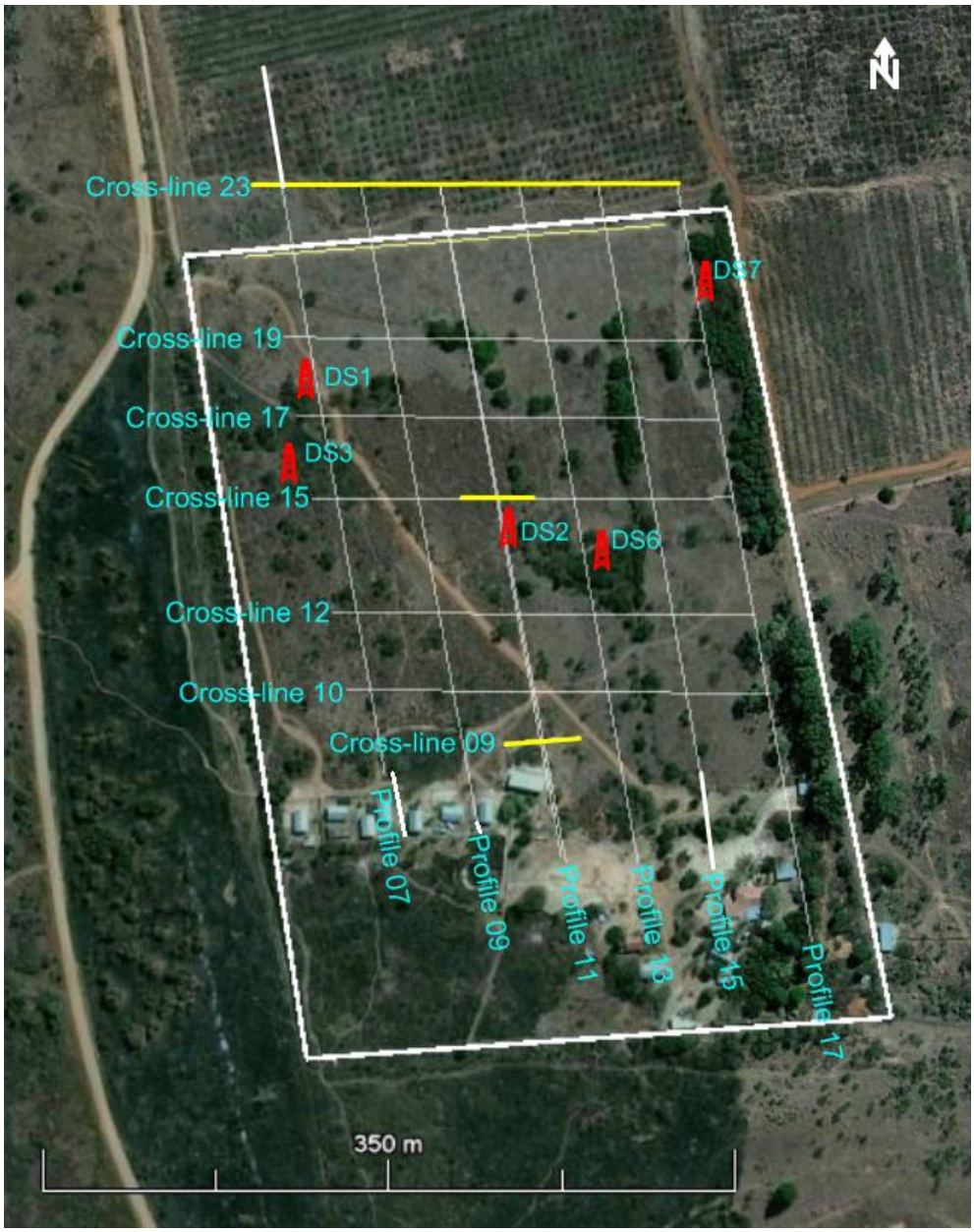

Figure 3.9. Image showing survey lines which were measured in 2011.

3.2.4 Experiments

3.2.4.1 **Description of the experiment**

Fieldwork

In the field, the resistivity meter was connected to an array of electrodes. The resistivity meter began a measurement using a distance that is equal to the minimum unit electrode and automatically did a traverse along the profile at steps of a unit electrode by selecting four electrodes at a time. The instrument would then vary the distance between the current and/or potential electrodes so that it could measure at a greater depth than the previous depth. Unless stated otherwise, the Wenner-Schlumberger array (with n = 1, 2, 3, 4, 5, 6) was used to collect data because vertical and horizontal structures were expected.

The starting points for the data measured in April and March 2011 were recorded by hand-held GPS with an accuracy of ~5 m and were marked with wooden boards so that the September measurements should have the same staring points. However, profiles 7 and 15 were extended to the north and south respectively. For the purpose of temporal comparisons, they were trimmed to the lengths of the initial data, but for structural interpretation, the full data set was used. An inversion was applied to minimize the effect of array type and noise, so that the resulting image was, as close as possible, a good approximation of the earth electrical image.

Data inversion

The data were exported using the Ares software, and were inverted using the Res2dINV software package. Finite-difference (Dey and Morrison, 1979) discretization was used for the inversion of the entire resistivity data set. A trapezoidal finite-difference grid with finer mesh was selected because some resistivity contrasts were more than 1:50 (Loke, 2001), notwithstanding that Sasaki (1989) argued that model blocks that are too small will often produce unrealistic models. The standard smoothness-constrained least-squares algorithm (de Groot-Hedlin and Constable, 1990) was selected for the inverse models because a

gradational change in the resistivities was expected due to deep weathering. A robust (Claerbout and Muir, 1973) smoothness-constraint with time-constraint weight of 10 units was selected for the time-lapse inversion (Loke, 2001; Loke, 1999). The robust smooth-constrain least-squares algorithm, which minimises the absolute changes in the model resistivities between the initial and time-lapse data sets, was used for the time-lapse inversion because it produces better results than the standard smooth-constrain least-squares algorithm, because the standard smooth-constrain least-squares algorithm produces a model that varies in a smooth manner, which obscures subtle changes. A default convergence value of 1% was used to determine the number of iterations; and where data could not converge below nine iterations, especially the time-lapse data, the inversion was terminated at the ninth iteration. After the convergence limit would have been reached, doing more iterations increased the rms error.

Time-lapse results and interpretations

The data will be interpreted by means of joint inversion between the data at the end of the rainy season and those at the end of the dry season. The measured data sets do not show noise which is shown by the rms error of 1.12-2.7% in the independent inversions, except for profile 11; hence, the pseudosections correctly show the apparent resistivity. Thus, the resistivity change between the two periods, except for profile 11, is largely influenced by moisture variations.

3.2.5 Results and interpretations

The depth scale shown in Table 3.1 was used for the pseudosections. The depth scale for the inverted models was calculated iteratively as it is one of the parameters that the resistivity data were inverted for.

Figure 3.10 shows the electrical image measured along profile 7 in Figure 3.9. The initial data set were measured April 2011 while the time-lapse data were measured in September 2011. The repeat profile was extended to the north by 55 m and to the south by 33m. The apparent resistivity, in the initial data (Figure 3.10a) and repeat

data (Figure 3.10b), increases with apparent depth and in the southerly direction. The apparent thin resistive layer of 158 Ω·m is sandwiched between layer of apparent lower resistivity and that of higher resistivity, but comes out to the surface towards the south end of the profile (Figures 3.10a and 3.10b), while thinning out to the northern end. The resistivity layers show an undulating character (Figure 3.10a and 3.10b).

Figure 3.10c shows the inverse model of the initial data while Figure 3.10d show the inverse model of the repeat data. Figure 3.10d is longer than Figure 3.10c the repeat profile was extended to the north and south so that the fault-like feature at the 66 m mark could be imaged better than Figure 3.10c. The lateral resistivity change in the top 5 m of the regolith at the 148 m mark in Figures 3.10c and 3.10d may indicate the effect of past agricultural practices. The low resistivity layer (Figure 3.10c) between the 77 and 225 m marks and a depth of 2-11m may indicate the presence of water, but the presence of the same layer in Figure 3.10d (time-lapse data set) suggests that this layer could be water-saturated clay. The sharp decline in resistivity of the regolith at the 66 m mark (Figure 3.10c and 3.10d) may indicate a lithological contact or shallow bedrock to the north. A fault striking east-west may also be a possibility. The resistivity highs at the bottom edges of Figure 3.10c could be an edge effect, however, since Figure 3.10d shows high resistivity at the bottom of the section may suggest that the high resistivity at the edges of Figure 3.10c are genuine. Bedrock resistivity values (>600 Ω·m) are showing up below the 33 m depth (Figures 3.10c and 3.10d).

Figure 3.10e shows the temporal resistivity image measured along profile 7, it is the difference plot between the two data sets (Figures 3.10c and 3.10b). Figure 3.10e shows that the resistivity of the top regolith (0-11 m) has increased by 15-20% between the 0 m and the 115 m marks, while the top regolith after this mark and the rest of the regolith have increased 5%. This suggests that the hydraulic conductivity of the soil to the north of the 88 m mark is higher than the hydraulic conductivity to

the south. The patches of little or no change in resistivity could be due to water-filled fractures that did not lose water between April and September 2011.

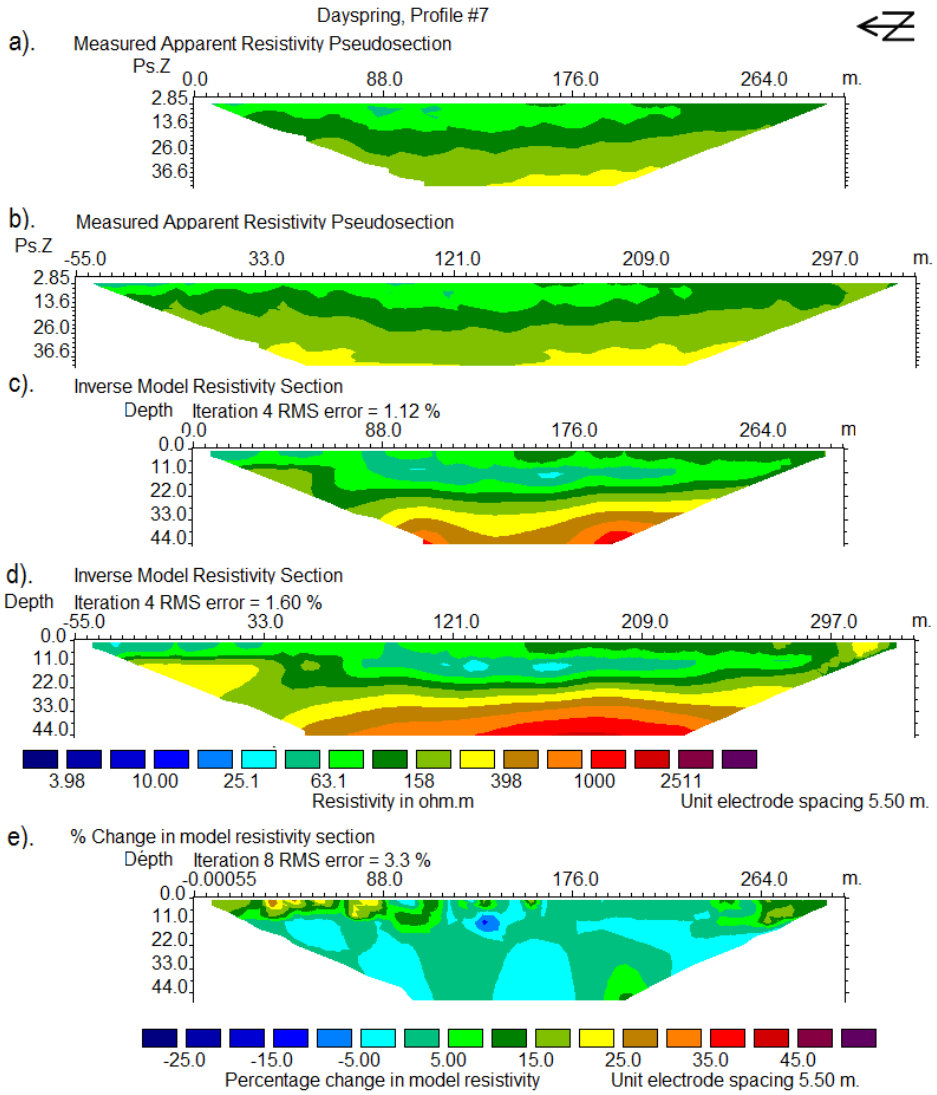

Figure 3.10: Electrical image along profile 7. (a) is the contoured apparent resistivity measured in in April 2011, (b) is the contoured apparent resistivity measured in in September 2011, (c) and (d) are the inverse models that represent the approximate electrical resistivity and depth of the geologic formations for the April and September data sets respectively, and (e) is the difference plot between the two periods starting from April 2011 to September 2011.

Figure 3.11 shows an electrical image measured along profile 9 in Figure 3.9. Figure 3.11a shows the initial (April 2011) measured apparent resistivity data while Figure 3.11b, which was extended to the south by 16.5 m, shows the repeat (September 2011) measured apparent resistivity data. The measured apparent resistivity increases to the south and vertically (Figures 3.11a and 3.11b). The apparent resistivity of the top subsurface to the south is higher than that to the north. The apparent resistivity layers have an undulating character. The contoured measured data shows low noise levels (Figures 3.11a and 3.11b).

Figure 3.11c shows the inverse model of Figure 3.11a while Figure 3.11d shows the inverse model of Figure 3.11b. The lateral change in resistivity of the top regolith (0-5 m) at the 143 m mark (Figures 3.11c and 3.11d) suggests that the electrical properties are different, which could have been caused by agricultural activities in the past. The two data sets (Figures 3.11c and 3.11d) show, from south to north, a steep change in the resistivity of the regolith at the 71 m mark, which could be due to lithological contact. The low resistivity layer (<100 Ω·m) could be a layer of clay. Bedrock resistivities are showing up below the depth of 30 m.

Figure 3.11e shows the temporal variation between the April and September data sets (Figures 3.11c and 3.11b respectively). Figure 3.11e shows that the resistivity of the top regolith (0-11 m) increased by up 20-25% between the 0 m and 220 m marks, suggesting that the soil to the north dewatered at a faster rate. The less resistive soil in Figures 3.11c and 3.11d shows a higher dewatering rate in the time-lapse image Figure 3.11c. The subtle vertical increase in resistivity below the 88-104.5 m mark reflects the presence of trees in this area. The horizontal low resistivity band (63 Ω·m) in Figures 3.11c and 3.11d shows a decrease in resistivity in Figure 3.11c probably due to water accumulation between the 121 m and the 214.5 m marks. The resistivity increase of the regolith at a depth of 22 m between the 165 and the 258 m marks suggests that the regolith in this region dewaters at a faster rate, suggesting that the lithology probably changes about the 165 m mark (Figure 3.11e). The bedrock

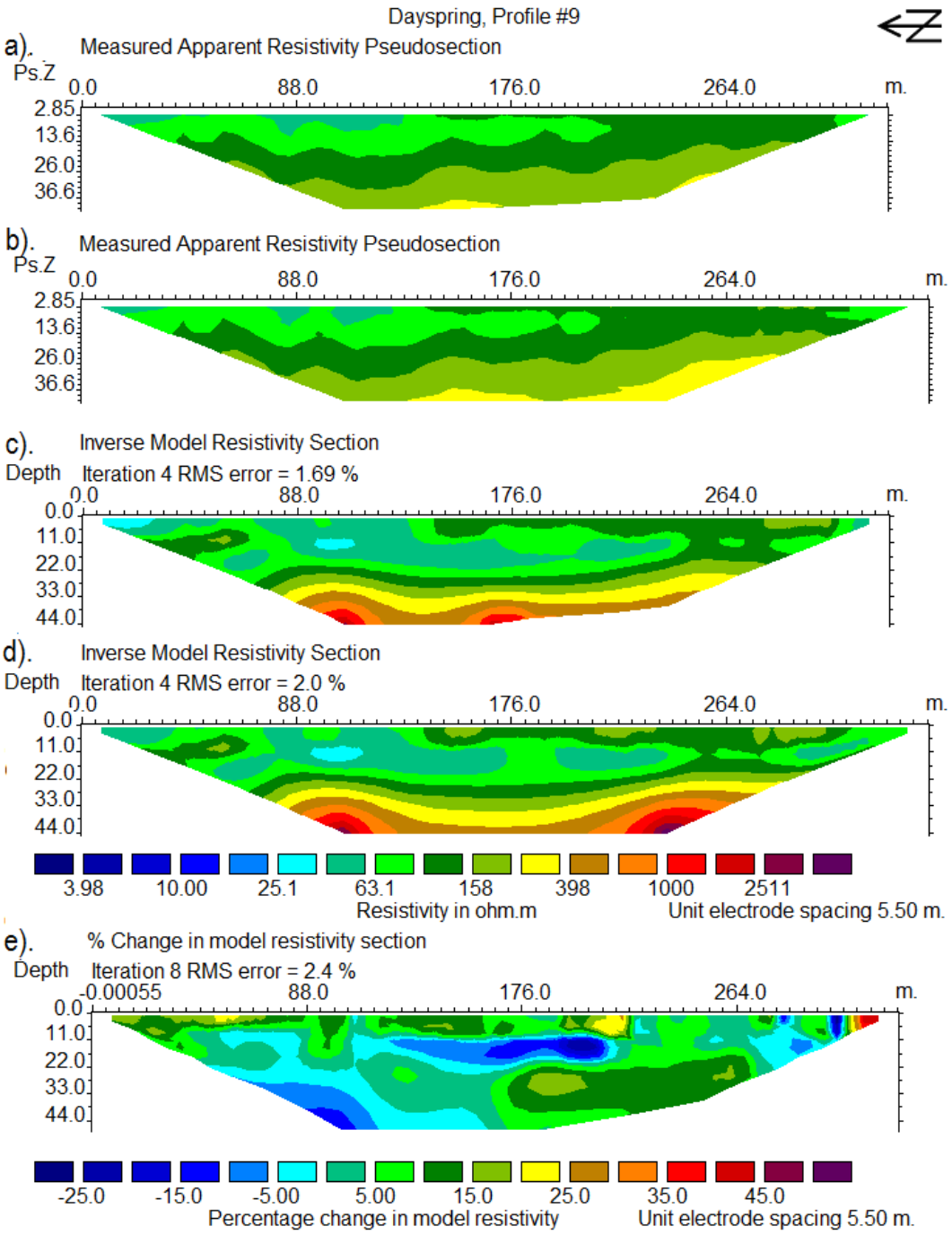

Figure 3.11. Electrical image along profile 9. (a) is the contoured apparent resistivity measured in in April 2011, (b) is the contoured apparent resistivity measured in in September 2011, (c) and (d) are the inverse models that represent the approximate electrical resistivity and depth of the geologic formations for the April and September data sets respectively, and (e) is the difference plot between the two periods starting from April 2011 to September 2011.

that emerges at the bottom left edge of Figures 3.11c and 3.11d shows a resistivity decrease in the difference plot (Figure 3.11e). This suggests that the bedrock is probably fissured and therefore may lose groundwater; it could also be that it is not bedrock but an artifact because edge effect.

Figure 3.12 shows an electrical image along profile 11 in Figure 3.9. Figure 3.12a shows the initial apparent resistivity data that were measured in May 2011, while Figure 3.12b shows the apparent resistivity data that were measured in September 2011. The contoured measured images show a thin low-apparent-resistive layer between the 88 and 292 m marks (Figures 3.12a and 3.12b). The apparent resistivity increases with depth (Figures 3.12a and 3.12b). The higher apparent resistivities seem to be shallower north of the 88 m mark though the layers seem to be dipping to the north (Figures 3.12a and 3.12b). The 398 Ω·m apparent resistivity at the bottom of the measured data (Figures 3.12a and 3.12b) is more prominent in this profile when compared with profiles 7 and 9.

Figure 3.12c, the inverse model of the initial data, and Figure 3.12d show a less resistive layer (< 60 Ω·m) in the top 11 m of the sections and as little as 25 Ω·m between 88 and 176 m mark, and between the 176 and 264 m mark. The shallow high resistivities may be due to current distortions, which may result in insufficient currents flowing into the deeper subsurface (Figures 3.12a and 3.12b). Figures 3.12c and 3.12d may not represent the geologic picture of the subsurface because borehole chips that came from DS2 show that the bedrock is approximately 35 m deep in the proximity of profile 11. Notice the rms error on both figures. Therefore, the apparent shallow bedrock may be due to current distortions, though the data are reproducible. The reproducibility of the data suggests that the low resistivity feature in the shallow subsurface is real, but it is not clear whether it is geologic or artificial.

Figure 3.12e is the temporal variation between the initial data (Figure 3.12c) and the repeat data (Figure 3.12d). There is a general 10% increase in resistivity in the top 11 m between 88 and 264 m. The maximum increase in resistivity to the south in top 22

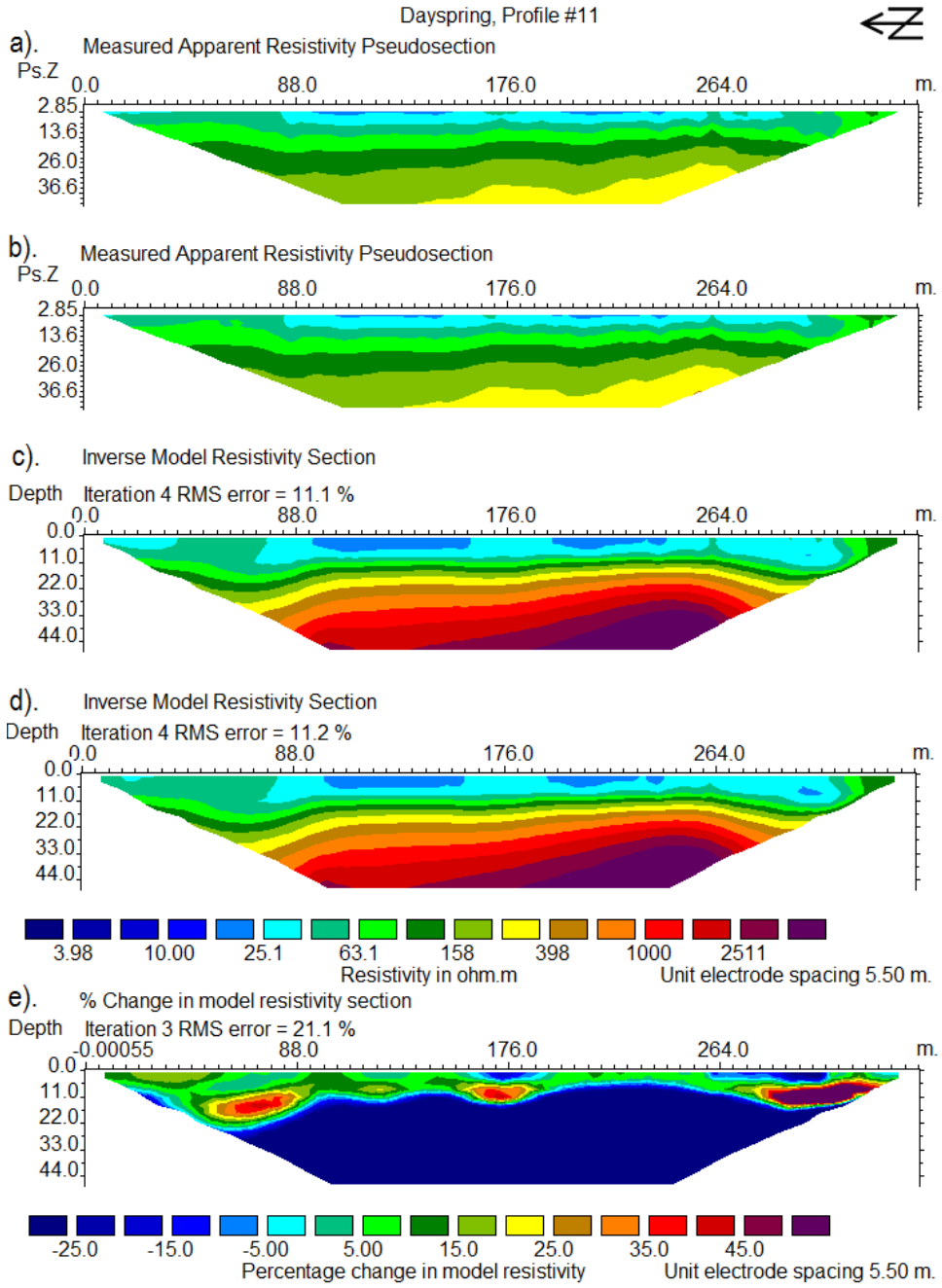

Figure 3.12. Electrical image along profile 11. (a) is the contoured apparent resistivity measured in in May 2011, (b) is the contoured apparent resistivity measured in in September 2011, (c) and (d) are the inverse models that represent the approximate electrical resistivity and depth of the geologic formations for the May and September data sets respectively, and (e) is the difference plot between the two periods starting from May 2011 to September 2011.

m of the section underlies a maximum decrease in resistivity. The patch of ~ 35 % increase in resistivity at the 176 m mark underlies a patch of resistivity decrease. The maximum decrease below the band of resistivity increase in Figure 3.12e may indicate that this profile does not represent a geologic cross-section because if the high resistivities in Figures 3.12c and 3.13d represent bedrock resistivities, then maximum decrease in resistivity is unlikely due to the low porosity and permeability of igneous and metamorphic rocks.

Figure 3.13 shows the electrical image along profile 13 in Figure 3.9. Figure 3.13a shows the initial apparent resistivity data that were measured in May 2011, while Figure 3.13b shows the apparent resistivity data that were measured in September 2011.The measured data (Figures 3.1ba and 3.13b) shows low apparent resistivity layers to the north. The arrangement of the apparent resistivity changes to the south of the 88 m mark. The 398 Ω·m apparent resistivity layer is more prominent here.

Figures 3.13c and 3.13d show the inverse models of Figures 3.13a and 3.13b respectively. The lateral changes in resistivity of the regolith indicate variations in hydraulic conductivity, which may indicate changes in lithology (Figures 3.13c and 3.13d). Bedrock resistivities are showing up below the 33 m depth, but disappear in the middle of the image, which could be due to a wide fracture or lithological change (Figures 3.13c and 3.13d).

Figure 3.13e shows the difference plot between Figures 3.13dc and 3.13d. The difference plot shows an overall resistivity change of +10% for the top regolith (0-11 m) across the profile suggesting a constant dewatering rate across the profile. The slightly higher resistivity increase of the top soil between the 165 and 209 m marks can be attributed to a thick bush in this area. The layer of soil just below the top regolith that shows little or no change in resistivity could be clay. This layer truncates a vertical feature that shows little or no change in resistivity between the 170 m and the 203 m marks. The difference plot shows a background resistivity increase of 5%.

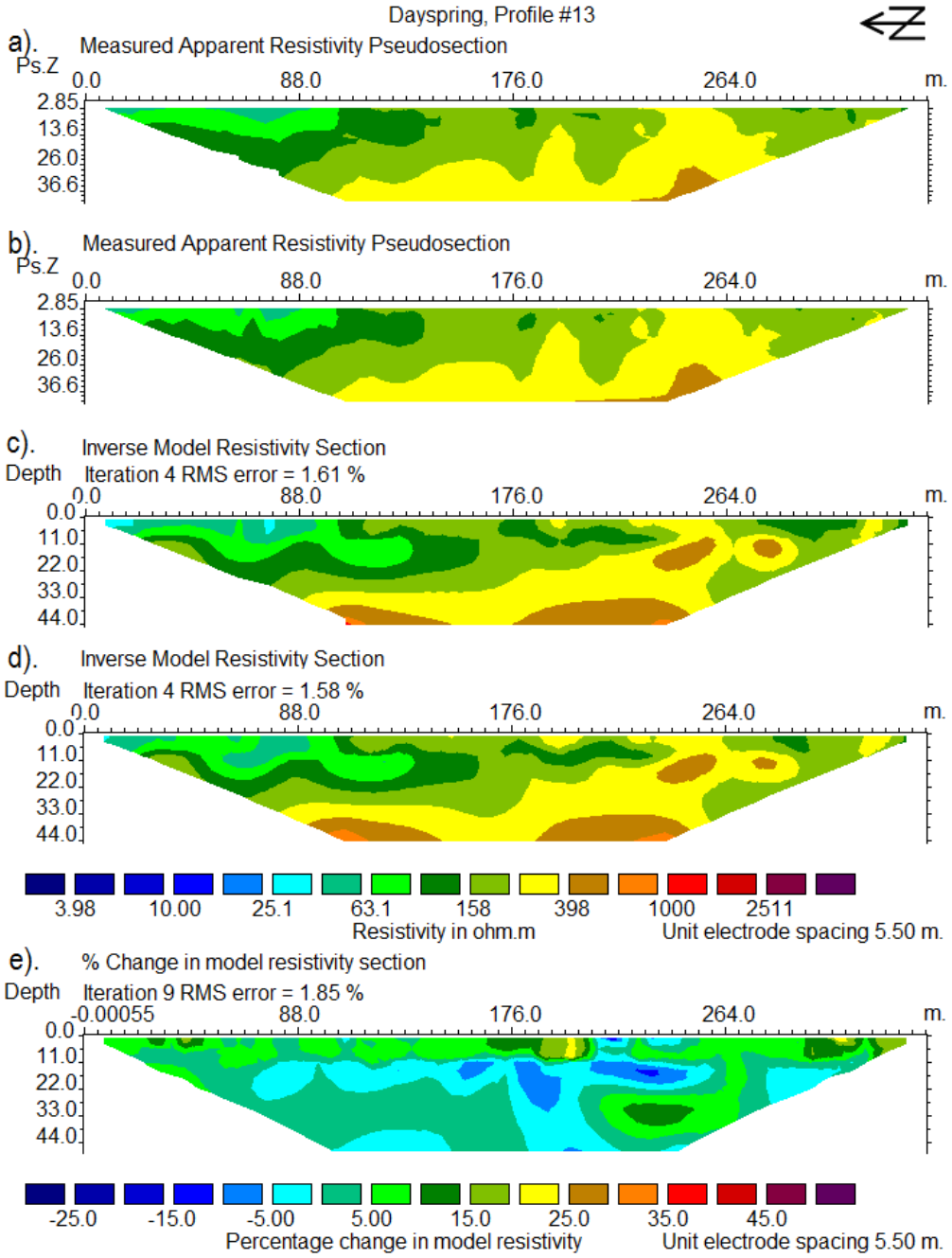

Figure 3.13. Electrical image along profile 13. (a) is the contoured apparent resistivity measured in in May 2011, (b) is the contoured apparent resistivity measured in in September 2011, (c) and (d) are the inverse models that represent the approximate electrical resistivity and depth of the geologic formations for the May and September data sets respectively, and (e) is the difference plot between the two periods starting from May 2011 to September 2011.

Figure 3.14 shows the electrical image measured along profile 15 in Figure 3.9. Figure 3.14a shows the initial apparent resistivity data that were measured in April 2011, while Figure 3.14b shows the apparent resistivity data that were measured in September 2011.The measured data (Figure 3.14a and 3.14b) shows lower apparent resistivities to the north and higher apparent resistivities to the south. The arrangement and apparent resistivities to the north looks similar to those observed in profile 13. The apparent resistivity layers show a general northerly dip. The apparent resistivity to the south shows higher resistivities when compared with profile 13, which is 40 m west of this profile.

Figures 3.14c and 3.14d show the inverse models of Figures 3.14a and 3.14b respectively. The lateral change in resistivity of the regolith may indicate changes in lithology (Figures 3.14c and 3.14d). The bedrock is deeper to the north of the 176 m mark and shallower to the south with the depression of bedrock in the middle of the section suggesting a wide fracture or change in lithology (Figures 3.14c and 3.14d).

Figure 3.14e shows the difference plot between the two data sets (Figures 3.14c and 3.14d). Figure 3.14e shows an inconsistent change in resistivity across the profile. The resistivity change for the regolith south of the 88 m mark depicts the top of the regolith while the resistivity change to the north of the 88 m mark does not show the top of the regolith. A maximum decrease in resistivity between the 99 m and the 160 m marks is located below a maximum increase. The little or no change in resistivity at the bottom left of the picture may indicate the presence of a compact rock.

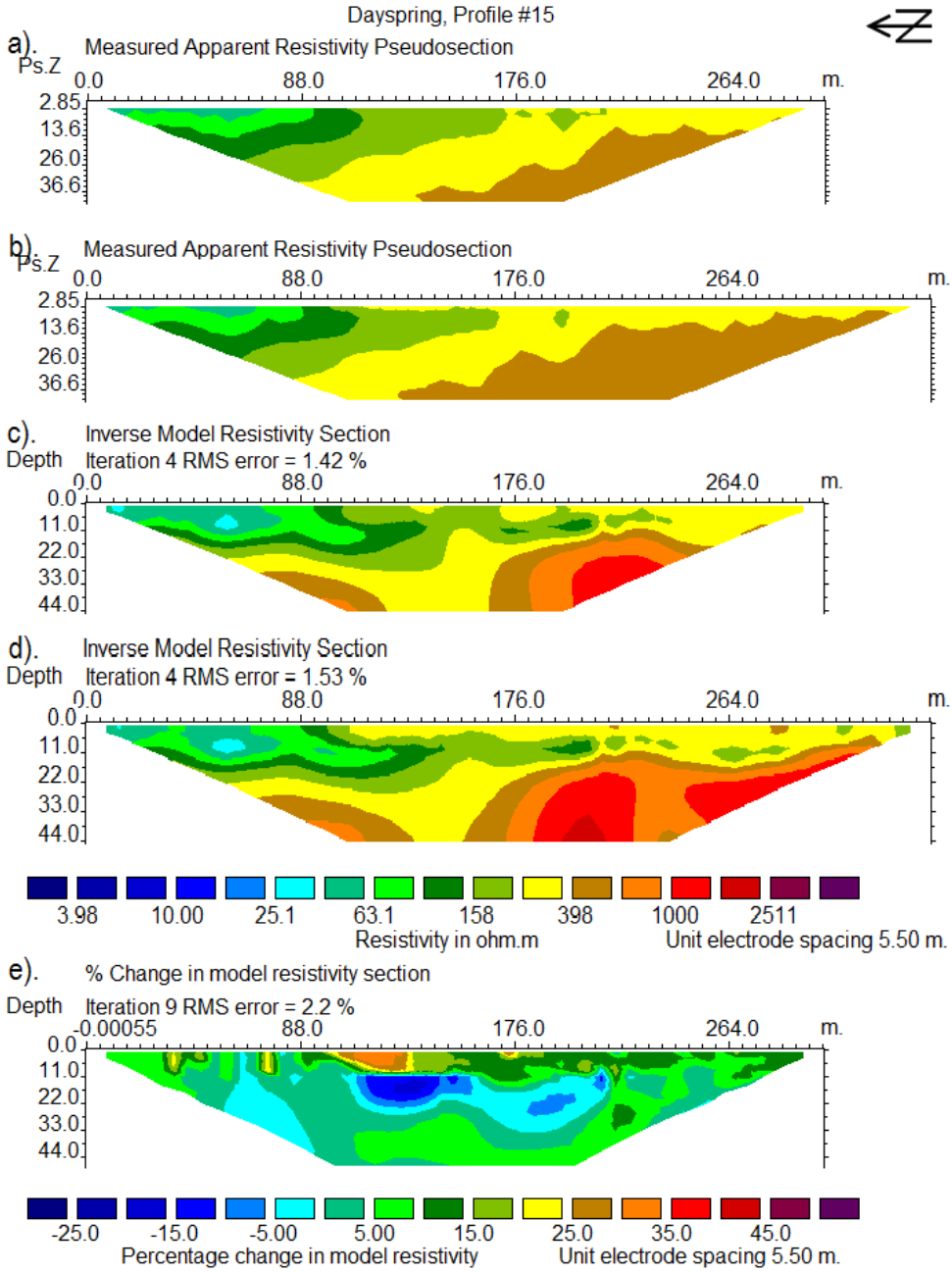

Figure 3.14. Electrical image along profile 15. (a) is the contoured apparent resistivity measured in in April 2011, (b) is the contoured apparent resistivity measured in in September 2011, (c) and (d) are the inverse models that represent the approximate electrical resistivity and depth of the geologic formations for the April and September data sets respectively, and (e) is the difference plot between the two periods starting from April 2011 to September 2011.

Figure 3.15 shows the electrical image measured along profile 17 in Figure 3.9, which is the closest to the bluegum and yellow wattle trees. Figure 3.15a shows the initial apparent resistivity data that were measured in April 2011, while Figure 3.15b shows the apparent resistivity data that were measured in September 2011.The contoured measured data (Figures 3.15a and 3.15b) shows low apparent resistivities to the north similar to profiles 13 and 15. The high resistivities are shallowest to the south of the 176 m mark when compared with the other profiles except for profile 11.

Figures 3.15c and 3.15d show the inverse models of Figures 3.15a and 3.15b respectively. The lateral change in the resistivity of the regolith may indicate changes in lithology (Figures 3.15c and 3.15d). The high resistivity (>400 Ω·m) in the top 5 m of the regolith in Figure 3.15d may indicate the effect of the bluegum trees. The bedrock is deeper to the north of the 176 m mark and shallower to the south, which may indicate lithological changes or deep weathering to the north. The sub-vertical feature at the 313 m mark could be a fracture, or the high resistivity feature between the 313 and 363 m marks and a depth of 5-16 m could be a boulder.

Figure 3.15e shows the difference plot between the two data sets (Figures 3.15c and 3.15d). The difference plot of profile 17 shows similar resistivity changes to those of profile 15 (Figure 3.14). The deeper soil (> 5 m depth) shows three zones of different resistivity changes. The noisy look of the image could be caused by the fissures in the bedrock, which preferentially allow water to pass through. The 15% increase in resistivity of the top regolith (0-11 m) below the bluegum trees could be reflecting the effect of the trees. The regolith below the yellow wattle trees shows little or no change in the two periods. Therefore, from this result, the impact of the yellow wattle trees is not obvious. The resistivity increase of up to 25% between the 176 and 264 m marks, laterally sandwiched between zones of little or no change in resistivity, could be due to the effect of deeper roots of the bluegum trees.

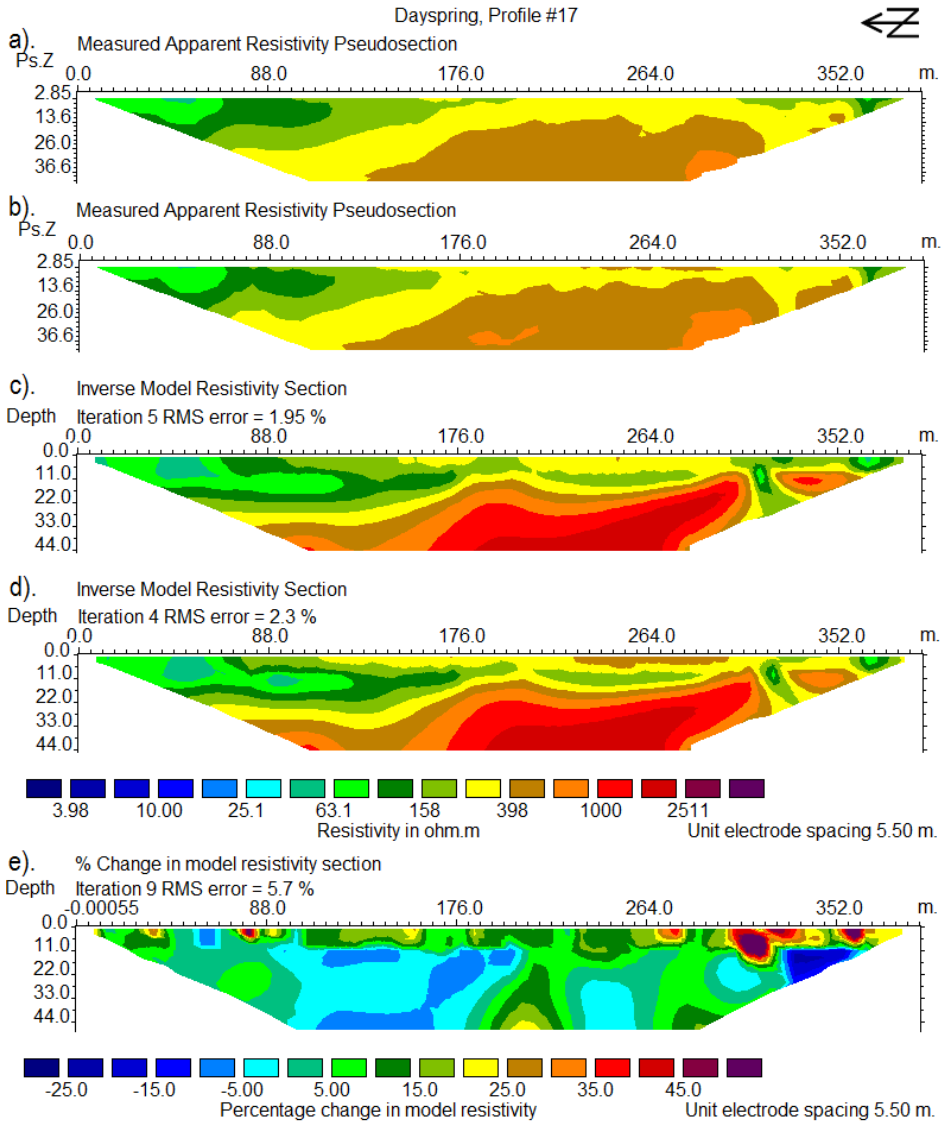

Figure 3.15. Electrical image along profile 17. (a) is the contoured apparent resistivity measured in in April 2011, (b) is the contoured apparent resistivity measured in in September 2011, (c) and (d) are the inverse models that represent the approximate electrical resistivity and depth of the geologic formations for the April and September data sets respectively, and (e) is the difference plot between the two periods starting from April 2011 to September 2011.

Figure 3.16 shows the electrical image measured along crossline 10 in Figure 3.9. Figure 3.16a shows the initial apparent resistivity data that were measured in May 2011, while Figure 3.16b shows the apparent resistivity data that were measured in September 2011. The measured data (Figures 3.16a and 3.16b) shows two distinctive apparent resistivities; higher apparent resistivities to the east and lower apparent resistivities to the west. There is a low apparent resistivity feature in the middle of the measured data.

Figures 3.16c and 3.16d show the inverse models of Figures 3.16a and 3.16b respectively. The resistivities of the regolith show two distinct properties reflecting a possible lithological contact (Figures 3.16c and 3.16d). The low resistivity feature in the middle of the images (Figures 3.16c and 3.16d) may be due to contaminated soil or conductive buried pipe. The bedrock is shallower to the east and deeper to the west.

Figure 3.16 shows the image measured along crossline 10 in Figure 3.9 at two different times of the year. Figure 3.16e shows the difference image between the two data sets (Figures 3.16c and 3.16d). The change in resistivity between the 132 m and the 214 m mark depicts the thickness of the top regolith (0-16 m. The 10% resistivity increase in the middle of the image reflects higher rate of dewatering, which may indicate that the hydraulic conductivity of the soil in this zone is higher.

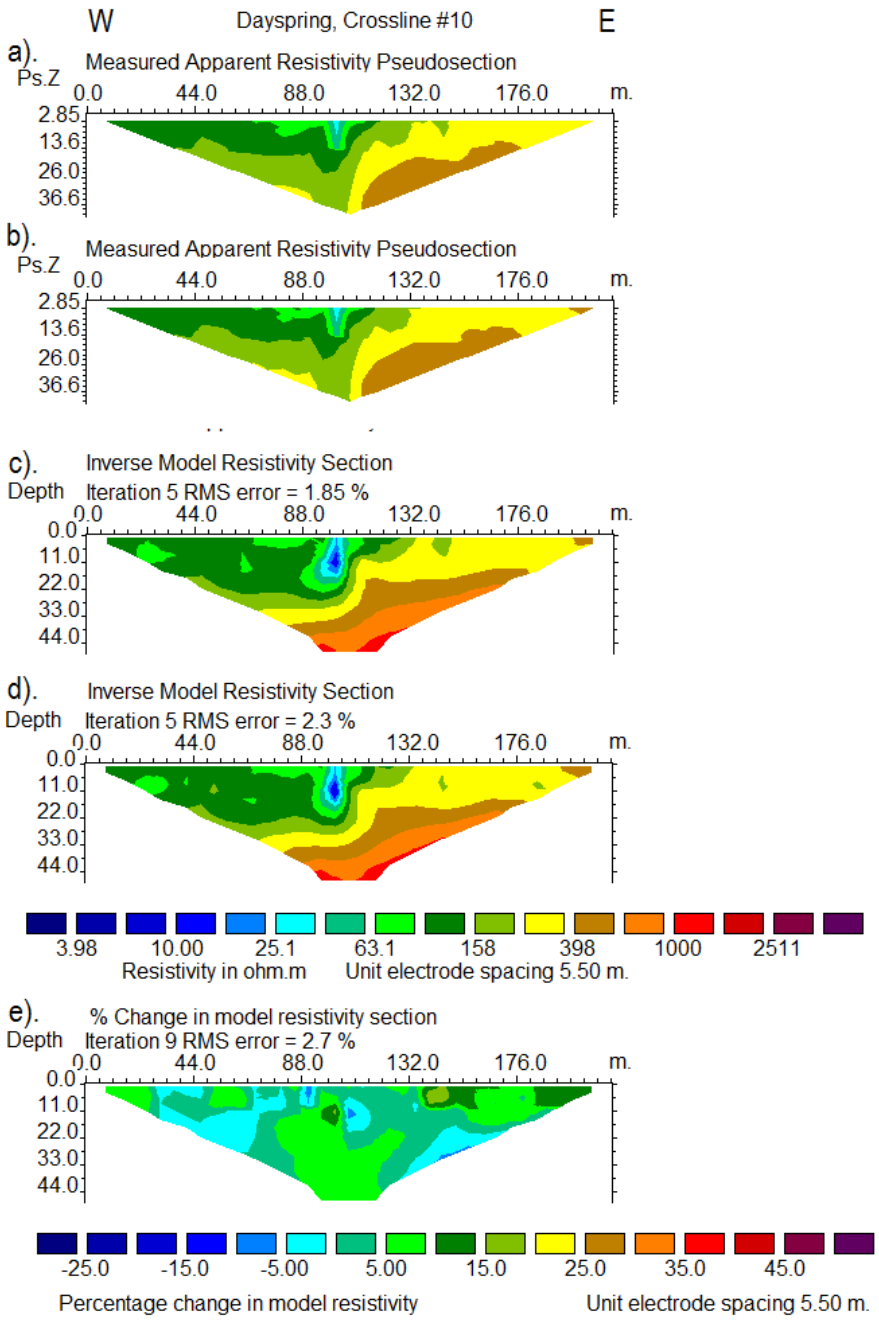

Figure 3.16. Electrical image along crossline 10. (a) is the contoured apparent resistivity measured in in May 2011, (b) is the contoured apparent resistivity measured in in September 2011, (c) and (d) are the inverse models that represent the approximate electrical resistivity and depth of the geologic formations for the May and September data sets respectively, and (e) is the difference plot between the two periods starting from May 2011 to September 2011.

Figure 3.17 shows the electrical image along crossline 12 in Figure 3.9. Figure 3.17a shows the initial apparent resistivity data that were measured in May 2011, while Figure 3.17b shows the apparent resistivity data that were measured in September 2011. The measured data shows higher apparent resistivities to the east and lower apparent resistivities to the west. There is a low apparent resistivity feature in the middle of the section.

Figures 3.17c and 3.17d show the inverse models of Figures 3.17a and 3.17b respectively. The inverse models show two regoliths separated by the low resistivity feature in the middle of the section, which may reflect changes in lithology. The depth to the bedrock and resistivities of the regolith to the west resemble those observed in profile 07 and 09 in Figures 3.10 and 3.11 respectively, while the resistivities to the east reflect those observed in profiles 13, 15 and 17 in Figures 3.13, 3.14, and 3.15 respectively. Notice the low resistivity feature in the middle of the image.

Figure 3.17e shows the difference image between Figures 3.17c and 3.17d measured along crossline 12. The top 8 m of the regolith to the east of the 115 m mark show a general resistivity increase of 10%, which suggest that the hydraulic properties of the soil across the profile are different, and thus lithological change at the 115 m mark. The resistivity decrease between the 115 and the 154 m marks shows water accumulation. The middle low resistivity feature shows a significant dewatering with a resistivity change of up to 20%. The bedrock resistivity values show a general increase of 5% because it is probably fractured, fissured and jointed, therefore permeable; or the resistivity increase in the bedrock may just be an artifact caused by an overshoot or undershoot in the join-inversion of the two data sets. The difference plot shows background resistivity increase of 5% and does not show any effect of the bluegums, as the resistivity change towards the trees is not as high except for the top regolith.

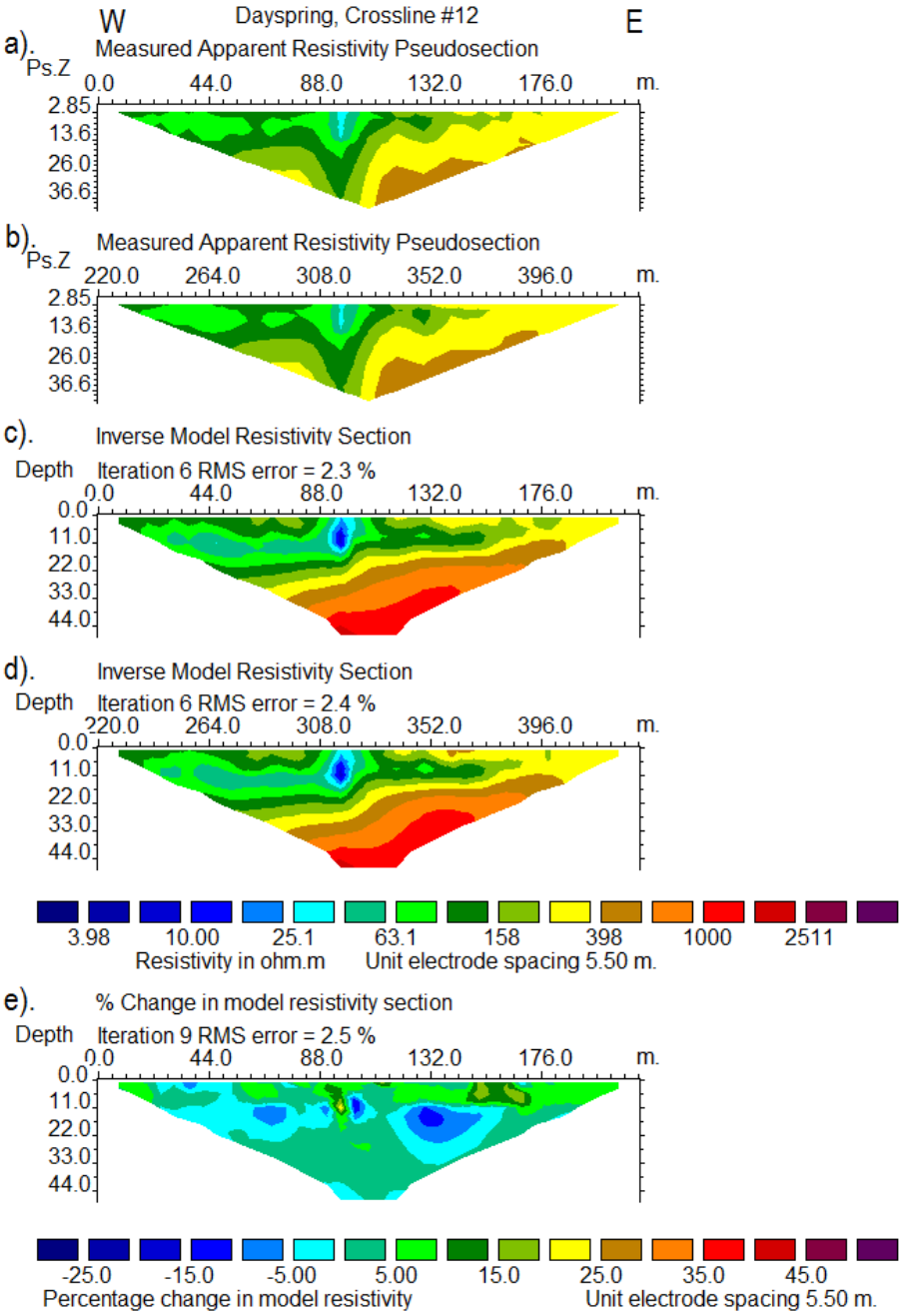

Figure 3.17. Electrical image along crossline 12. (a) is the contoured apparent resistivity measured in in May 2011, (b) is the contoured apparent resistivity measured in in September 2011, (c) and (d) are the inverse models that represent the approximate electrical resistivity and depth of the geologic formations for the May and September data sets respectively, and (e) is the difference plot between the two periods starting from May 2011 to September 2011

Figure 3.18 shows an electrical image measured along crossline 15 in Figure 3.9. Figure 3.18a shows the initial apparent resistivity data that were measured in May 2011, while Figure 3.18b shows the apparent resistivity data that were measured in September 2011. The measured data shows higher apparent resistivity to the east and lower apparent resistivity to the west. The resistivity change is about a low apparent resistivity feature in the middle of the image.

Figures 3.18c and 3.18d show the inverse models of the measured data, Figure 3.18a and 3.18b respectively. The inverse models show a thick regolith with lateral change in electrical properties at the 104 m mark, which may indicate lithological changes. Notice the low resistivity feature in the middle of the section. Bedrock is shallower to the east and deeper to the west.

Figure 3.18e show the difference image of Figures 3.18c and 3.318d measured along crossline 15. While the top soil (0-11 m depth) is well delineated by the difference plot, the soil to the east of the middle low resistive feature shows higher rate of dewatering than the soil to the west. The middle feature shows resistivity decrease in Figure 3.18e while this feature showed resistivity increase in Figures 3.16e and 3.17e. The regolith to the west in Figures 3.18c and 3.18d is less resistive than the regolith to the east, yet the hydraulic conductivity of the regolith to the east is higher than that to the west, which may reflect different lithologies. Figure 3.18e shows a lens with a negative differences (blues) surrounded by positive differences (green). The difference plot does not show a resistivity increase towards the bluegum trees.

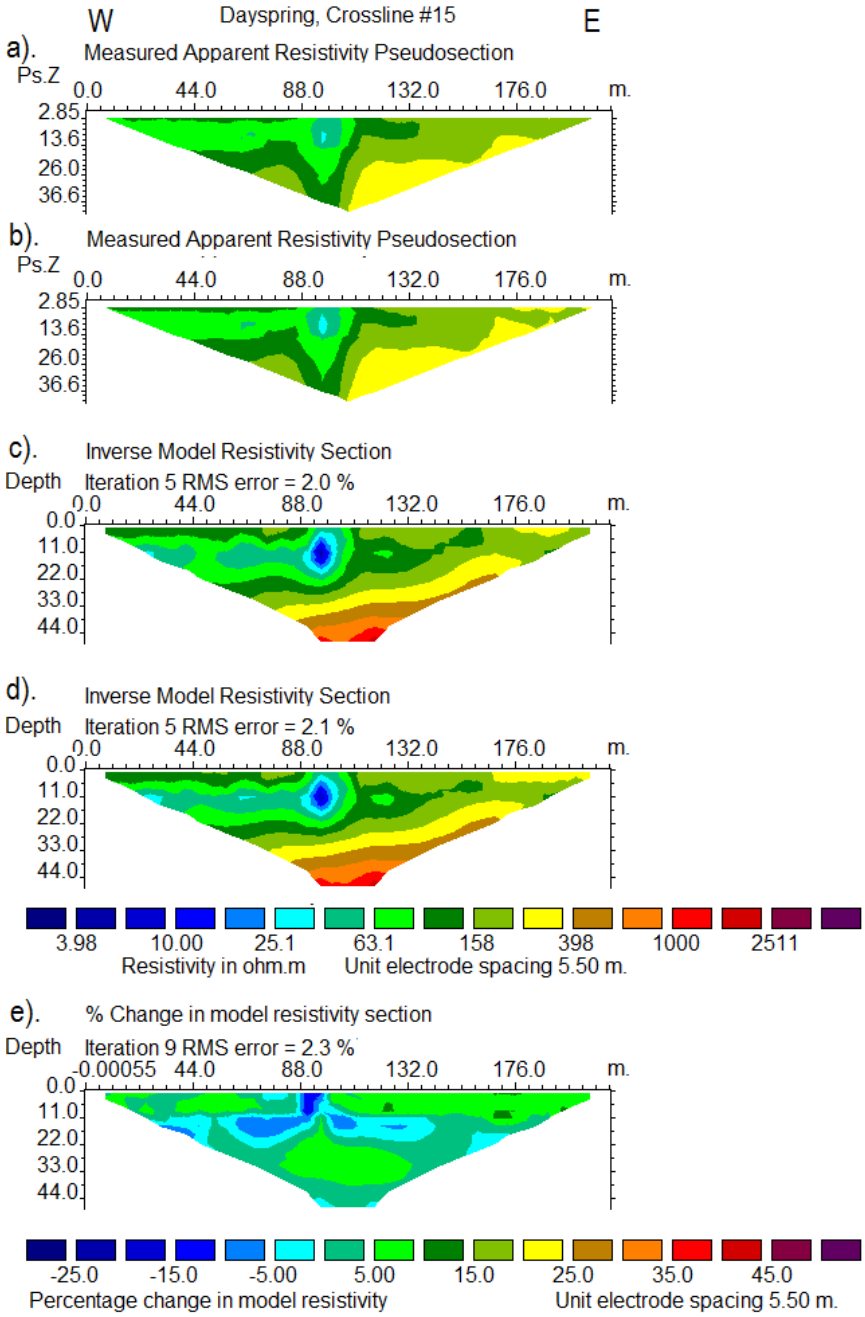

Figure 3.18. Electrical image along crossline 15. (a) is the contoured apparent resistivity measured in in May 2011, (b) is the contoured apparent resistivity measured in in September 2011, (c) and (d) are the inverse models that represent the approximate electrical resistivity and depth of the geologic formations for the May and September data sets respectively, and (e) is the difference plot between the two periods starting from May 2011 to September 2011

Figure 3.19 is the electrical image measured along crossline 17 in Figure 3.9. Figure 3.19a shows the initial apparent resistivity data that were measured in May 2011, while Figure 3.19b shows the apparent resistivity data that were measured in September 2011. The measured data shows higher apparent resistivity to the east and lower apparent resistivity to the west. There is a low apparent resistivity feature between the 121 and 132 m marks..

Figures 3.19c and 3.19d show the inverse models of Figures 3.19a and 3.19b respectively. The inverse models show a 30 m thick regolith with lateral changes in resistivity, which may indicate lithological changes. Notice the low resistivity feature in the middle of the section. The bedrock is showing up below the 33 m depth.

Figure 3.19e show the time-lapse image computed between the two data sets in Figures 3.19c and 3.19d. The general 10% resistivity increase of the top regolith across the section shows that rate of dewatering is constant. The maximum increase in resistivity between the 165 and 176 m marks is associated with presence of trees at this position (Figure 3.9). Crossline 17 shows a layer of continuous hydraulic conductivity below the top regolith (0-11 m) across the profile that shows little or change, which may indicate that the lithology is continuous across the profile. The difference plot also shows the 10% increase in resistivity in the middle of the section that connects the low resistivity feature, similar to crosslines 10 and 15. The difference plot does not show resistivity increase towards the yellow wattle trees.

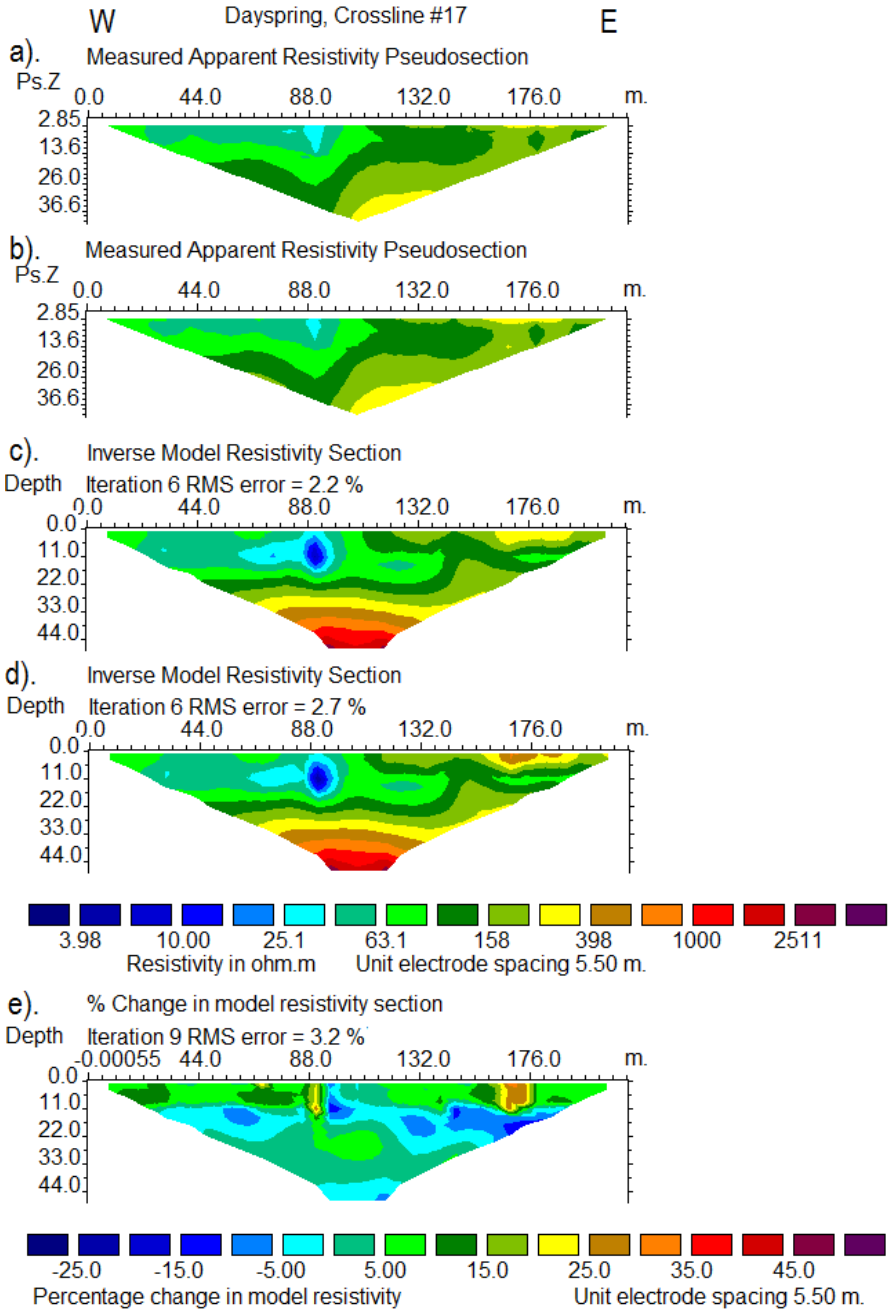

Figure 3.19. Electrical image along crossline 17. (a) is the contoured apparent resistivity measured in in May 2011, (b) is the contoured apparent resistivity measured in in September 2011, (c) and (d) are the inverse models that represent the approximate electrical resistivity and depth of the geologic formations for the May and September data sets respectively, and (e) is the difference plot between the two periods starting from May 2011 to September 2011

Figure 3.20 shows an electrical image measured along crossline 19 in Figure 3.9. Figure 3.20a shows the initial apparent resistivity data that were measured in May 2011, while Figure 3.20b shows the apparent resistivity data that were measured in September 2011. The measured data shows continuous apparent resistivities along the section except in the top subsurface where there is 63 Ω·m, and the middle of section where there is a depression associated with the low apparent resistivity feature.

Figures 3.20c and 3.20d show the inverse models of Figures 3.20a and 3.20b respectively. Figure 3.20c appears clipped to west and shows a narrow bottom because an electrode, that was supposed to be in the middle of the road, was not used in the measurement of the initial data set. The inverse data show a thick regolith with the lateral change not so great to warrant lithological change (Figures 3.20c and 3.20d). Notice that the resistivity of the middle feature has decreased when compared to profiles 10, 12, 15, and 17. The bedrock is showing up below the depth of 22 m.

Figure 3.20e shows the difference image computed between the two data sets (Figures 3.20c and 3.20d). The hydraulic conductivity of the top regolith (0-11 m) is similar across the section, depicted by the 10% increase in resistivity, which may indicate continuous lithology across the profile. The low resistivity feature in the middle shows resistivity increase. The bedrock shows little or no change to the west and 5% decrease to the east probably because it is fractured and /or fissured and thus permeable. The difference plot does not show resistivity increase towards the yellow wattle trees.

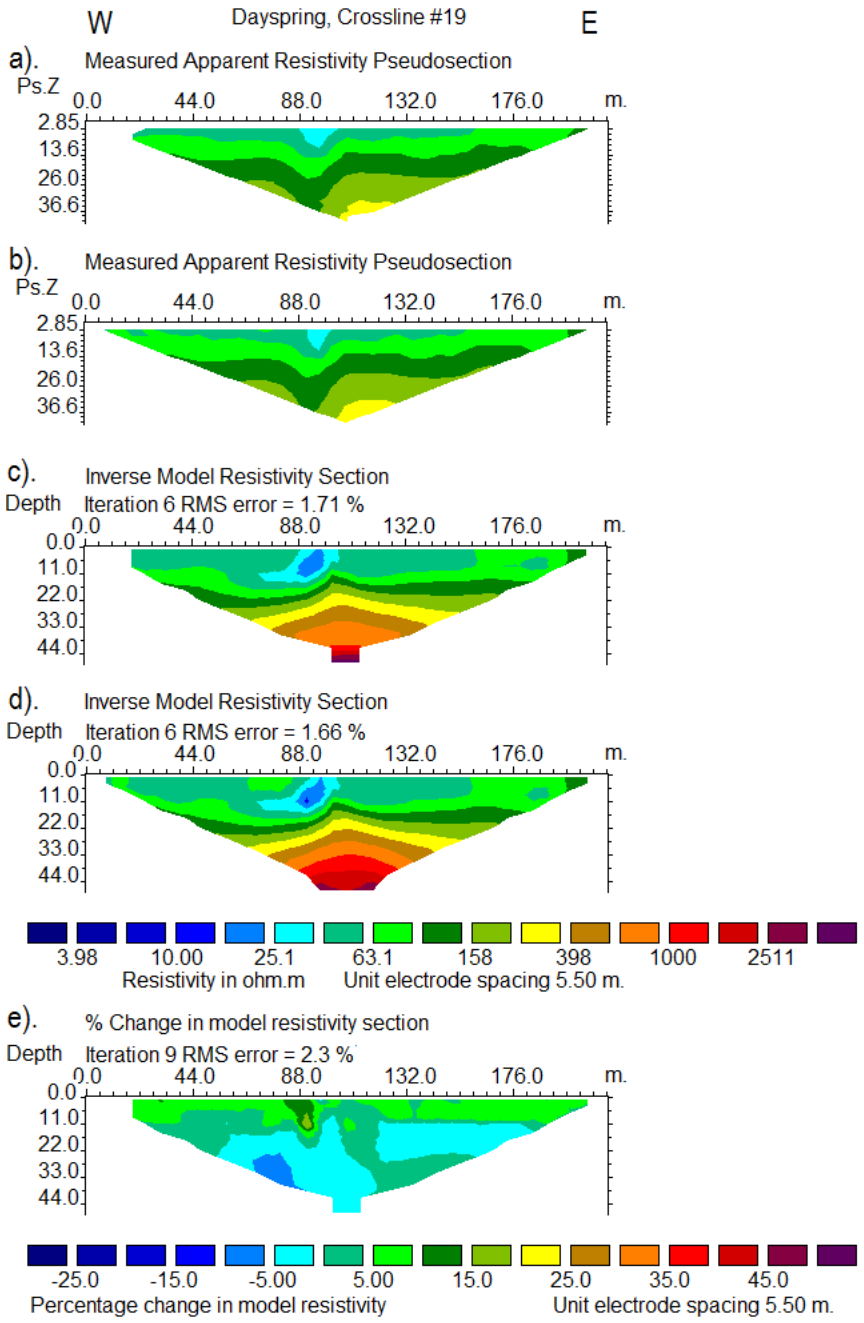

Figure 3.20. Electrical image along crossline 19. (a) is the contoured apparent resistivity measured in in May 2011, (b) is the contoured apparent resistivity measured in in September 2011, (c) and (d) are the inverse models that represent the approximate electrical resistivity and depth of the geologic formations for the May and September data sets respectively, and (e) is the difference plot between the two periods starting from May 2011 to September 2011.

The inverted resistivity data obtained before the end of the wet season are summarized in Figures 3.21 and 3.22. The data are presented in depth slices obtained from the inverse model sections and were gridded to get the resistivity maps. The depth ranges are 0-1 m, 1-4 m, 4-7 m, 7-10 m, 10-14 m, 14-17 m, 17-22 m, 22-26 m, 26-31 m, and 31-37 m. This grid comprises five profiles and five crosslines with line spacing of 40 m (except between profiles 09 and 13, and crosslines 12 and 15) and station spacing of 5.5 m. Profile 11 is not included in the grid as it may not represent the subsurface geology. Thus, the grid honours the resistivity distribution of the subsurface, though the ground coverage becomes smaller with depth.

On the depth-range (0-1 m) image (Figure 3.21a), the low resistivity zone to the north coincides with mafic rocks, while the higher resistivity to the southeast coincides with boulders of hornfels. The intermediate resistivity in light green maps feature that is running north-south (Figure 3.21a). On the depth-range 1-4 m image (Figure 3.21b), the higher resistivity to the southeast decrease slightly, while the resistivity of the north increases slightly. The north-south feature is more developed at this depth range (1-4 m). The image (Figure 3.21c) for depth-range 4-7 m shows that while the resistivity to the north is increasing, the resistivities to the southeast and to the west are decreasing. As the resistivity of the northern part increases, a low resistive feature develops running almost east-west (Figure 3.21c). On the image for depth-range 7-10 m (Figure 3.21d), the resistivity to the north continues to increase, while a patchy less resistive zone develops to the west. By depth-range 10-14 m (Figure 3.21e), the less restive zone to the west is more developed, while the less resistive feature that was running east-west is no longer evident. The resistivity to the southeast begins to increase at this depth range (10-14 m). On the image for depth-range 14-17 m (Figure 3.21f), the low resistive zone that had developed to the west has become non-coherent smaller substantially reduced. Moreover, the 14-17 m depth range shows that there are higher resistivity zones to the east than those to the west. Depth ranges 17-22 m and 22-26 m (Figure 3.22g and 3.22h) show that the resistive zone to the southeast is more developed, while the increasing resistivity to the west develops

patchy zones of intermediate resistivities. Figures 3.22i and 3.22j begin to show high resistivities across the entire images.

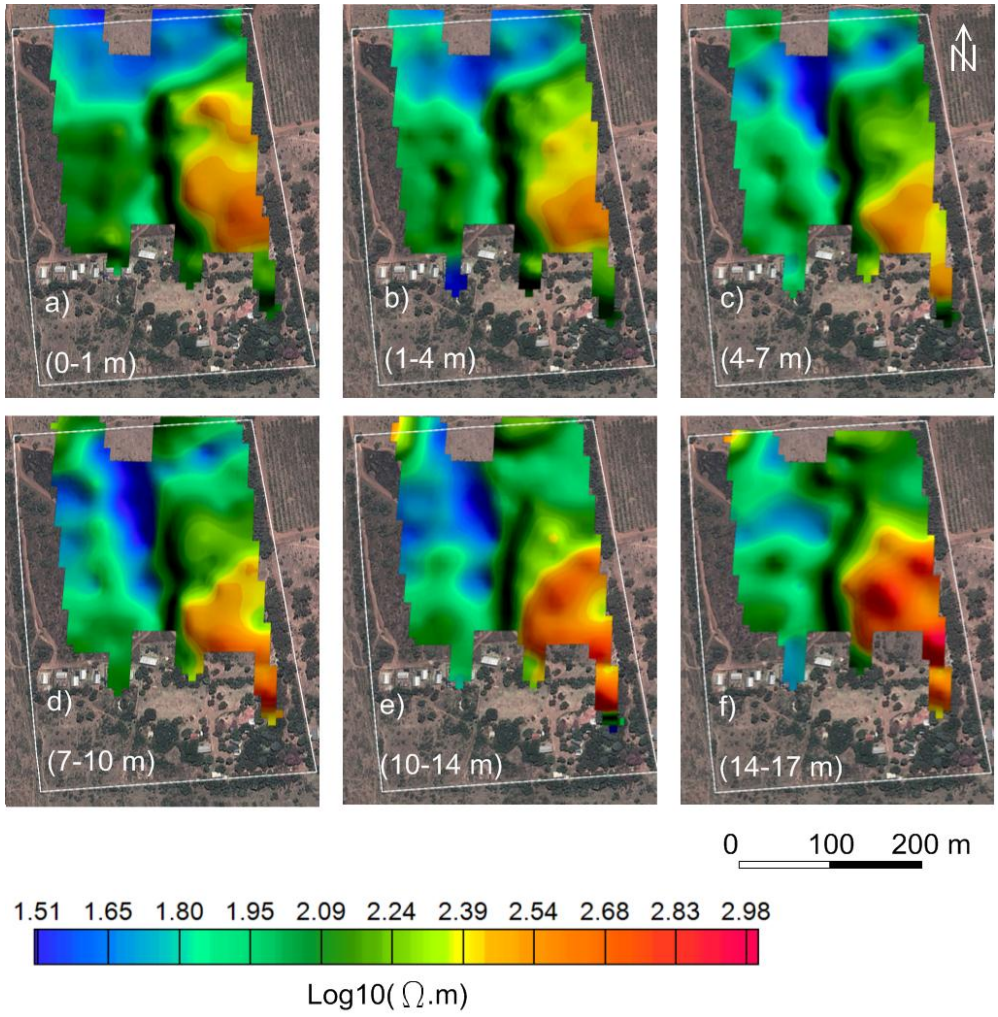

Figure 3.21. Resistivity depth slices from 0 to 17 m for March and April 2011. The depth ranges are as follows: a) 0-1 m, b) 1- 4 m, c) 4-7 m, d) 7-10 m, e) 10-14, f) 14-17 m.

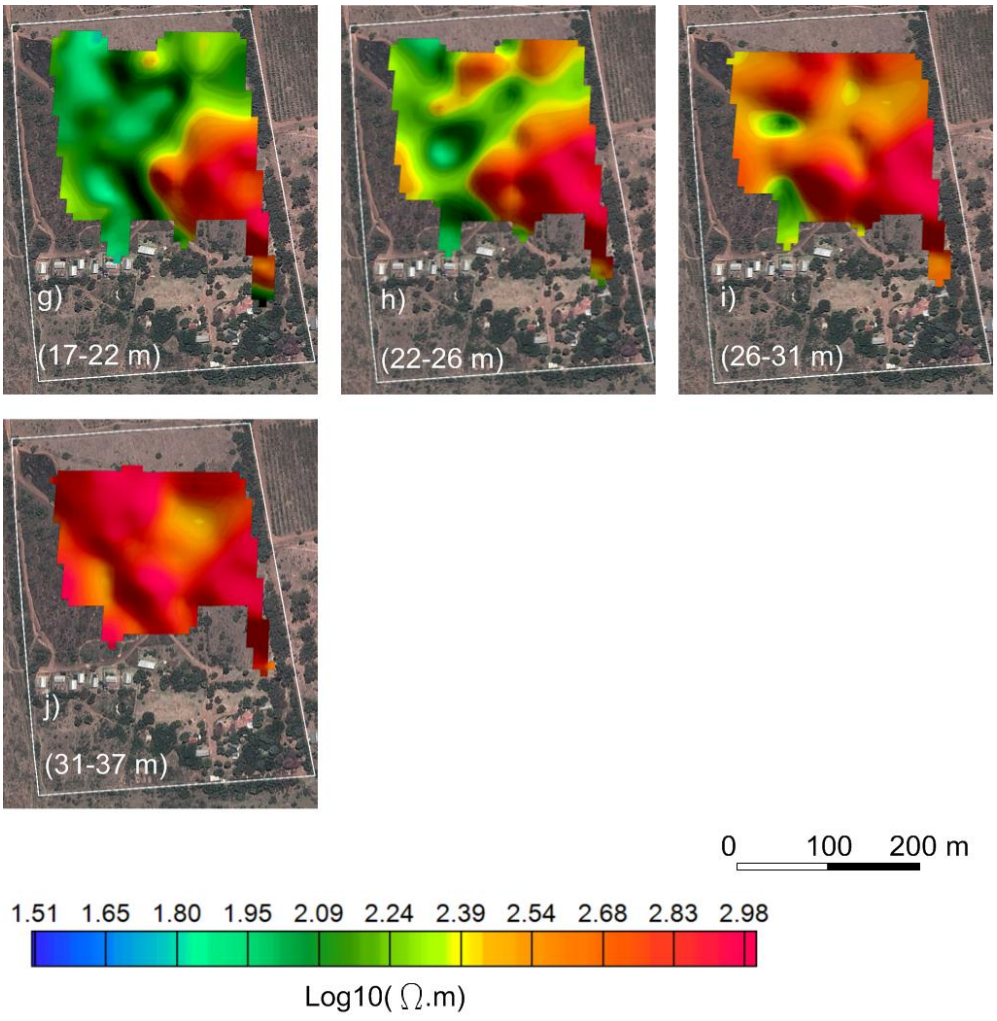

Figure 3.22. Resistivity depth slices from 17 to 31 m for March and April 2011. The depth ranges are as follows: g) 17-22 m, h) 22-26 m, i) 26-31 m, j) 31-37 m.

3.2.6 Discussion of results

Electrical noise

Van Zijl (1977) has reported electrical noises due to telluric and industrial leakage currents. As reported in Van Zijl (1977), sources of the electrical noises from industrial leakages include railway lines, hoists in mining areas, electric furnaces, and

aluminum smelters. However, due to the distance (> 10 km) between the study area and industrial places the electrical noise can be deemed insignificant. Moreover, I used a maximum MN spacing of 16.5 m with the ARES Resistivity and IP Automatic system for the Wenner-Schlumberger array configuration, which gives good signal to noise ratio. Thus, the resistivity results of this study show little electrical noise if any and can be trusted for interpretation.

Geology

The fence plot in Figure 3.23 summarizes the profile and crossline data for the data which were collected at the end of the dry season. There is great correlation between the profiles and the crosslines especially in the resistivity of the regolith. The correlation of the bedrock resistivities is poor on profiles 11 and 13. As pointed out before, profile 11 does not represent the geologic image of the subsurface, hence poor correlation, though the top regolith correlates well with the crosslines. I cannot explain the failure of profile 13 to correlate with crossline at the lower regolith.

The north-south profiles reveal that there may be lithological changes as the shown by the lateral changes in the resistivity of the regolith (Figure 3.23). The lithology to the north could be mafic sills as there are outcrops of the rock type towards the northern fence of the school property (Figure 2.2). Profiles 15 and 17 reveal that the bedrock is shallow to the south, and boulders of hornfels are found in this area (Figure 2.2), which may indicate that the lithology to the south is hornfels. Profiles 07 and 09 show a thicker regolith when compared with those of profiles 15, and 17 (Figure 3.21), which may indicate a lithological change from east to west. Crosslines 10, 12, 15 and 17 show lateral changes in resistivity of the regolith (Figure 3.23). The regolith to the west is thicker than the regolith to the east, which supports the observation from the profiles that there is a possibility of lithological change from east to west, or deeper weathering to the west.

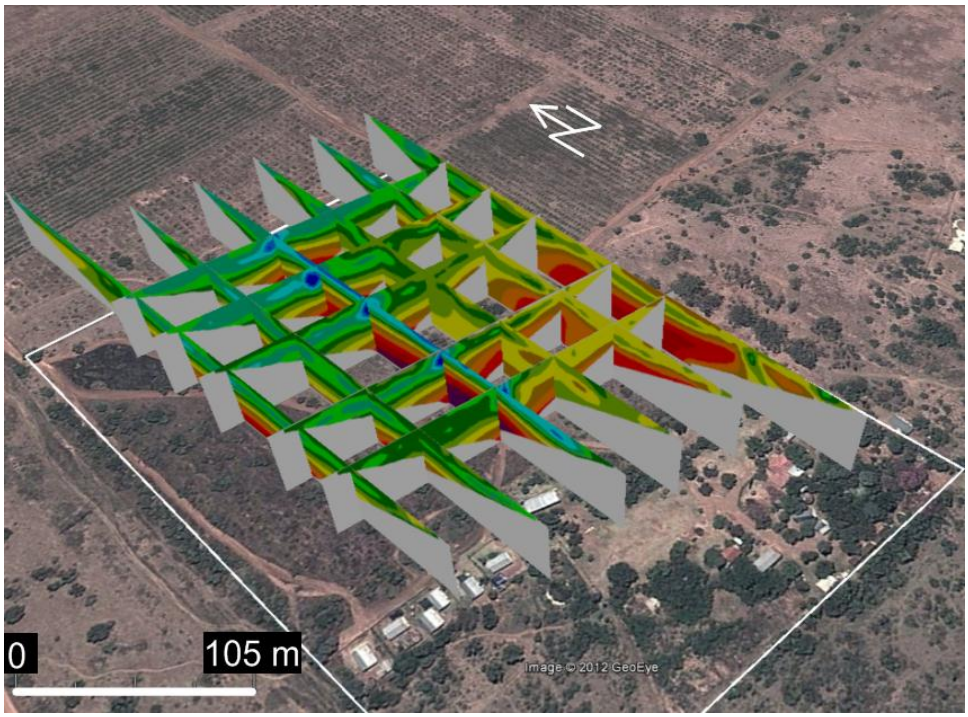

Figure 3.23. A fence plot of the profiles and crosslines.

The top regolith (0-4 m) is divided into north and south regions; and the southward region is further subdivided into two east and west regions (Figure 3.22a and 3.22b). The low resistivity to the north may reflect clayey soil that was derived from the weathering of mafic sills because there are outcrops of mafic rocks coinciding with the resistivity change in Figures 3.22a and 3.22b. The lithology to the east marked by high (>250 Ω·m) resistivity is a hornfels, because there are boulders of this rock type in this area (Figure 2.2), and the bedrock is shallower (Figure 3.21e to Figure 3.22h). The lithology to the west is difficult to classify because there is no clue of any rock type except for rock floats. However, the low resistivity that emerges in this area as depth increase (Figures 3.21d and 3.21e) could be due to a regolith that was derived from mafic sills, which are slightly deeper than the northwards mafic sills. Figures 3.22i and 3.22j show that bedrock resistivities for the probable mafic sills west start to emerge from a depth of about 26-31 m.

The profile and crossline data have shown that the geology of the study area, as small as 300 m x 400 m, is complex. The bedrock (>600 Ω·m) is shallow to the east and to

the south, but fractured and or fissured as revealed by the time-lapse resistivity changes. This argument is supported by Acworth (2001) where it was suggested that fractured bedrock resistivities are between 300 and 600 Ω·m. Thus, the regolith is as thick as 33 m to the west and as shallow as 11 m to the east. Palacky (1988) argued that a saprolite is the most conductive part of the regolith, but may not be distinguishable because it is intermediate between the overlying mottled zone and underlying fractured bedrock. Acworth (2001) supports this argument, but uses a different nomenclature. This seems to be the case at Dayspring because the resistivity data show a gradual increase between the top soil and the bedrock.

Impact of invasive plants

Conein and Barker (2002) argue that if precipitation is not enough to feed the needs of the trees, the soil around them slowly dehydrates. They further argued that while the effect of roots is up to 1 to 1.5 times the height of the tree, visible effects are confined to the upper 3 m of the soil. Sudmeyer et al. (2004) in their study have shown that the root density of bluegum was highest in the top 0.5 m and the root lateral extent was 1.5 to 2 m times the height of the tree. Time-lapse resistivities that were measured by Barker and Moore (1998) and Jones et al. (2009) have shown that tree root effects start near the tree and, with time, increases in magnitude, lateral extent, and depth extent. However, the depth of investigation was limited to the top 5 m of the subsurface or less and therefore is not conclusive of the effect of trees at greater depths.

In this study, the general increase in resistivity, between the end of rainy and dry seasons, of the top 5 m of soil is 10% across all profiles. Profile 17, which is the closest to the invasive trees, shows an increase of up to 20% of the top soil; which may imply that the depletion of groundwater during the dry season by the trees increased the resistivity by an extra 10%. The line of indigenous trees along profile 15 (Figure 3.9) makes it difficult to relate the 20% increase in resistivity, which was ascribed to the invasive trees above. However, profiles 9 and 7, which are 160 and 200 m west of profile 17 respectively, show increases up to 20% in the resistivity of

the top soil which makes it difficult to ascribe the resistivity increase near the invasive plants to their effect.

Sudmeyer et al. (2004) have concluded in their study that the lateral extent and density of the roots within the top 0.5 m would make bluegum compete for water with agricultural crops. However, most ground of the study area is covered with grass, short and tall, but no agricultural crops. In fact, the resistivity increase of up to 20% shown by profiles 7 and 9 corresponds to short grass with roots that do not extend lower than 0.2 m. Therefore, the higher dewatering rate shown by profiles 7 and 9 could be attributed to soil with higher hydraulic conductivity while the higher dewatering rate near the invasive plants could to be attributed to the shallow root effect.

The work of Dawson and Pate (1996) has shown that the majority of water uptake comes from the top soil during the rainy season and deeper sources during the dry season. This could explain the lower than expected dewatering rate of the top soil near the invasive trees. It appears that the trees are using taproots to get water from depth, possibly the fractured bedrock because deeper roots of the bluegum show visible effects on the changes of the soil resistivity in profile 17, which is in agreement with the work of Dawson and Pate (1996).

Linear structures

The low resistivity feature that was observed in the crosslines can also be seen in the gridded data. This north-south striking feature could be due to a buried metallic pipe because it is shallow. However, evidence from the test model of a buried pipe, suggest that this signature could not be that of a buried pipe because it does not show the two low resistivity lobes on either side of the feature as shown in Figures 3.3 to 3.5. An in-depth discussion of a double lobe low resistivity on either side of a buried pipe can be found in Vickery and Hobbs (2002). Nassir and Lee (1999) did an electrical resistivity line over a metallic buried pipe, and their results showed resistivity lows on either side of the pipe. While they could account for the resistivity

low to the left of the pipe, they did not mention anything about the resistivity low to the right.

In an attempt to verify the test models of a buried pipe, so that the north-south striking feature could be explained, I did three resistivity lines, two with an electrode spacing of 1 m (similar to the test model), and the other was 5.5 m spacing but was slightly north of Dayspring property. I did part of crossline 15 in Figure 3.9 with an electrode spacing of 1m using the Wenner-Schlumberger array across the low resistivity feature. The results (Figures 3.24) show a resistivity low at the feature but fail to show any low resistivity lows on either side of the feature. The feature does not resemble a pipe because it is slightly inclined and elongate in one direction (Figure 3.24). I also did a short line parallel to crossline 9 in Figure 3.9 with an electrode spacing of 1 m using the Wenner array because it has high signal strength and hence resistant to noise. The results (Figure 3.25) obtained with the Wenner array show that the feature continues to the south, but very wide (~ 9 m) for a buried pipe. As this feature was thought of as a buried pipe at Dayspring property, I did crossline 23 in Figure 3.9 with a station spacing of 5.5 m using the Wenner-Schlumberger array. The results (Figure 3.26) obtained show that the feature continues to the north, off Dayspring property but it is not as conductive as in the crosslines to the south. Therefore, there is no plausible evidence that this feature is due to a buried pipe.

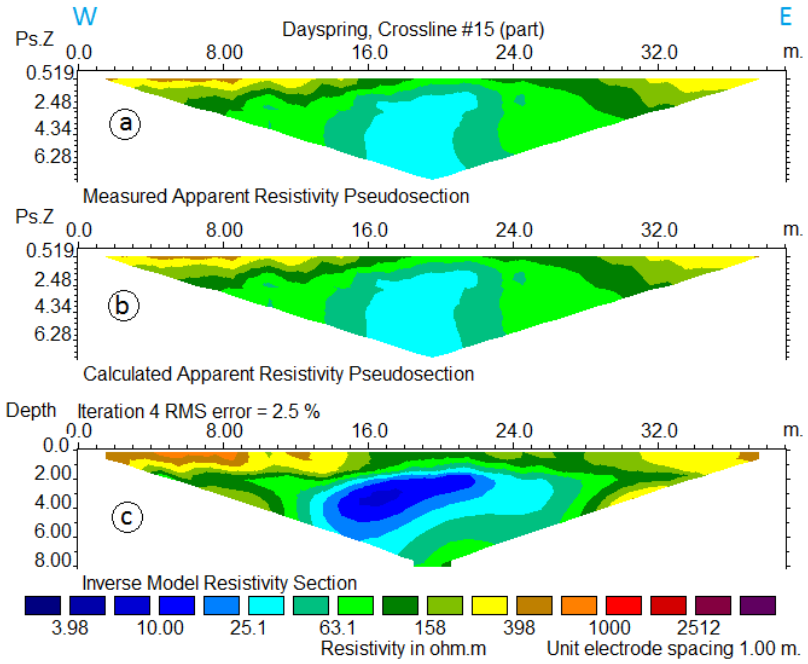

Figure 3.24. Electrical image along part of profile 15 using the Schlumberger configuration.

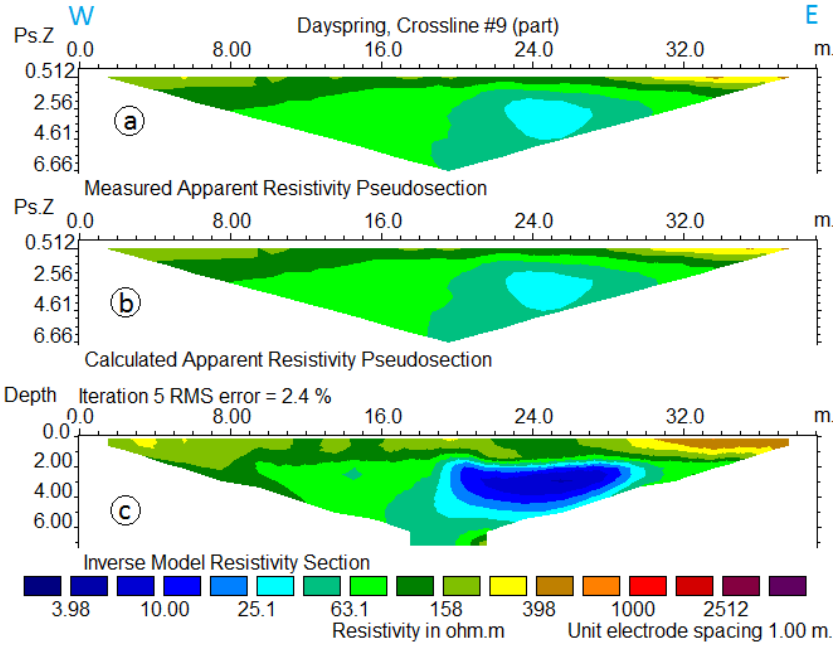

Figure 3.25. Electrical image along part of profile 9 using the Wenner array.

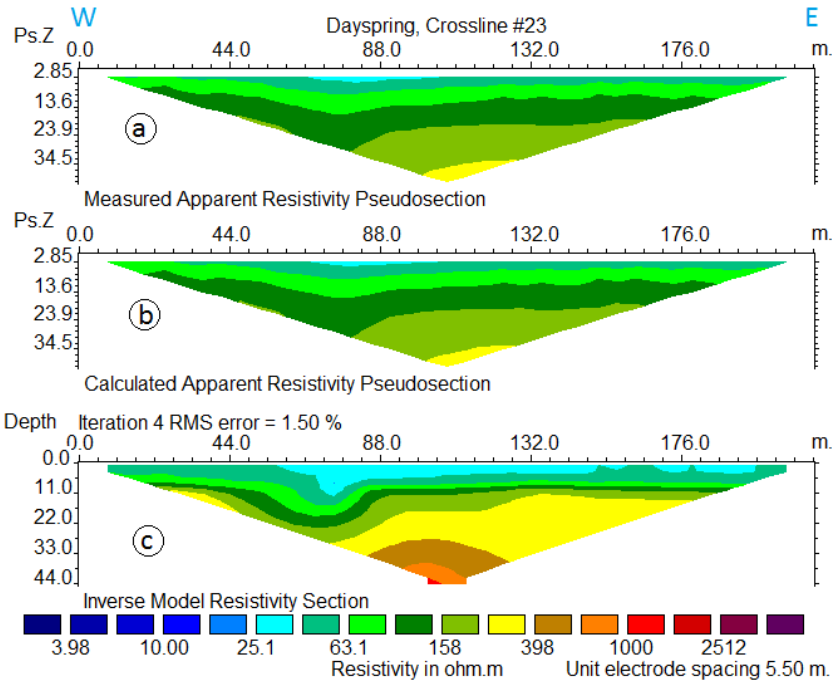

Figure 3.26. Electrical image along part of profile 23 using the Wenner-Schlumberger array.

The north-south striking feature is probable not geologic, but the gridded data reveal the mafic sill and the hornfels are separated by an east-west striking feature of low resistivity at a depth of 7-10 m (Figure 3.21d). The slight difference in the two features is that the east-west striking feature is not saturated; hence, the resistivity is not as low as in the north-south striking feature. Thus, the north-south striking feature could be a steeply dipping fracture. However, the borehole chips from DS2 reveal that there is ~30 m of regolith, and in such a case, one cannot expect a fracture zone to be preserved. Moreover, the crossline data collected using the dipole-dipole array (Appendix), which is good for resolving vertical features, do not show any significant differences from the data collected using the Wenner-Schlumberger array. There is no plausible evidence that this low resistivity feature could be due to a steeply dipping fracture.

Other studies have shown that fractures can develop below the clayey weathered layer (e.g. Hazell et al., 1988). A close inspection of the low resistivity suggests that the low resistivity feature may be associated with a saturated narrow ribbon-like clay

layer (Figure 3.21). Thus, the north-south striking feature with low resistivity could be fractured clay parallel to a lithological joint.

Groundwater contamination

Borehole DS2 produces smelly greenish water when pumping commences. The water is possibly contaminated with the E.coli bacteria. It is also reported that DS4 had smelly water. Therefore, if the north-south striking feature has cracks or is fractured, then this may explain the contamination because there is a pit latrine, along strike, south of borehole DS2 and in the proximity of DS4.

Chapter 4. Other data sets at Dayspring School

4.1 Preliminary DC Resistivity surveys at Dayspring School

The DC resistivity method was used by Ngobeni (2009) used to investigate the impact of alien tree species on groundwater at Dayspring School.

4.1.1.1 **Description of the equipment and materials employed.**

Data were acquired using the Geotron G41. The instrument is cased in an aluminum box. It is a manual single channel instrument. The transmitter has current output range from 10 to 1000 mA while the maximum voltage output is 400 V. It has an input impedance of 10 MΩ with noise rejection filter. It has a resolution of 0.1 mA and 0.1 mV. A 12 V built-in rechargeable battery provides power. The following configurations: Wenner, Schlumberger, dipole-dipole, and self-potential are supported.

4.1.1.2 ***Data acquisition in 2009 and 2010***

Steel electrodes were pounded into the ground until they were firm, and they were saturated with water to improve ground contact. The resistivity meter was connected to four electrodes at a time to make a measurement and would make traverses at intervals of 5 m along the profile. Each data point had 6 cycles of measurements and the standard deviation thereof was not allowed exceed 0.3%; and should the standard deviation be >0.3%, the measurement would be re-run until a satisfactory standard deviation was obtained. A Wenner alpha array configuration was used to measure lines 1, 2 and 3 where the potential electrodes are placed between the current electrodes and the separation between the potential and current electrodes is kept constant.

Line 1 (Figure 4.1) was measured on the 15th, 16th, 22nd of August and 3 September 2009, and repeat measurements were collected on the 17th, 18th and 19th of March 2010. A minimum electrode spacing of 5 m and cable lengths allowing sample spacings of 5, 10, 20, 40, and 60 m lengths were used to do the measurements. The repeat line was extended to the north by 90 m to cover more ground.

Figure 4.1. Image showing survey of the preliminary data.

Line 2 (Figure 4.1) was measured on the 23rd and 24th of September 2009 and repeat measurements were collected on the 27th and 28th of March 2010. The spacings employed for line 2 and its repeat were 5, 10, 20, 40, and 60 m. The repeat line was not parallel, but close to the first measured line 2 because I was trying to straighten it.

Line 3 (Figure 4.1) was measured on 24 September 2009 and there are no repeat measurements for this line. A minimum electrode spacing of 5 m and only cable lengths allowing sample spacings of 20, 40, and 60 m were used to collect data because of time constraints.

The starting position of the line 1 was clearly marked during the initial measurements of the preliminary surveys and this was helpful in locating as close as possible the positions of the electrodes for the time-lapse measurements. The noise levels were very low and therefore any changes in resistivity were due to temporal effect.

4.1.1.3 ***Results and interpretations***

2009 results and interpretations

Figure 4.2 shows the image measured along the line 1a in Figure 4.1. The measured data (Figure 4.2a) shows a lateral change in resistivity. The high resistivity (>600 Ω·m) layer rises steadily to the south where it drops sharply at the 240 m mark. Figure 4.2b shows the calculated data which fits the measured data well revealed the low rms error of 2.8%. Figure 4.2c is the inverted image and shows (1) a resistive top regolith from surface to 5 m depth, (2) a less resistive lower regolith between the 5 m and 15 m depths, and (3), highly resistive bedrock from a depth of 15 m.

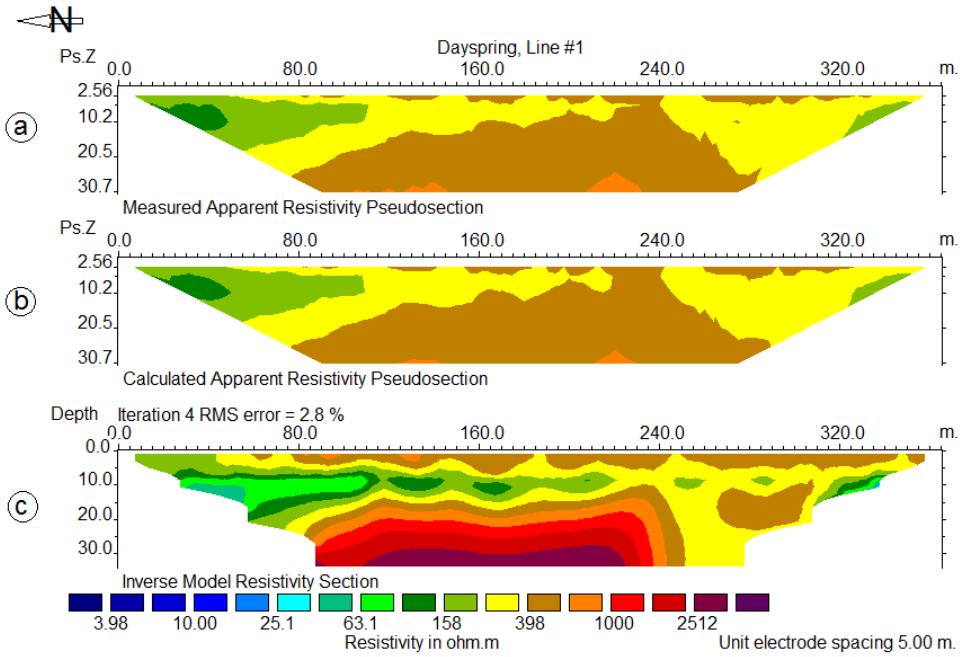

Figure 4.2. Electrical image along line 1 for the Wenner array. (a) is the measured contoured image, (b) is the calculated image from the model, and (c) is the inverse model that represents the approximate electrical resistivity and depth of the geologic formations.

Figure 4.3 shows the image measured close (~ 5m) to borehole DS1 along line 2a in Figure 4.1. The measured data (Figure 4.3a) shows lateral and vertical changes in apparent resistivity, with the higher apparent resistivities (> 150 Ω·m) shallower to the north and to the south. The calculated data (Figure 4.3b) fits the measured data well revealed by the low rms of error of 3.0%. The inversion image (Figure 4.3c) shows a lateral change in resistivity of the regolith, which may indicate lithological changes. The thin band of low resistivity (<100 Ω·m) between a depth of 10 and 15 m could be clayey material. The bedrock is showing up below a depth of 25 m.

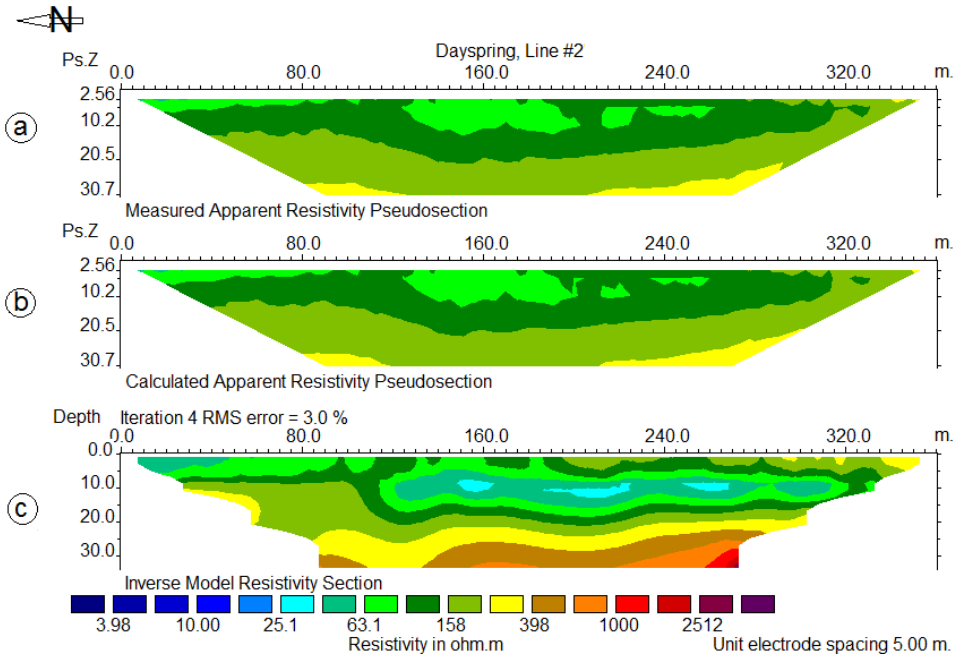

Figure 4.3. Electrical image along line 2a.

Figure 4.4 shows the image measured along line 3 in Figure 4.1, intersecting lines 1a and 2a. I used a minimum cable spacing of 10 m due to time constraints, so resolution was lost in the top 10 m. Nevertheless, the measured data (Figure 4.4a) shows low (<100 Ω·m) apparent resistivity to the west and higher (>100 Ω·m) apparent resistivity to the east. The apparent resistivity also increases with depth. The calculated data (Figure 4.4b) and measured data show low misfit of 4.3%. The inverted data (Figure 4.4c) shows a less resistive regolith down to a depth of 15 m, and bedrock from a depth of 15 m. The lateral changes in resistivity of the regolith in Figure 4.4c may indicate lithological changes. The low resistivity in the middle of Figure 4.4 could be due to a steeply dipping fracture zone or lithological contact or a pipe. However, soil profiles cannot preserve fracture zones; therefore, the model of a fracture cannot hold.

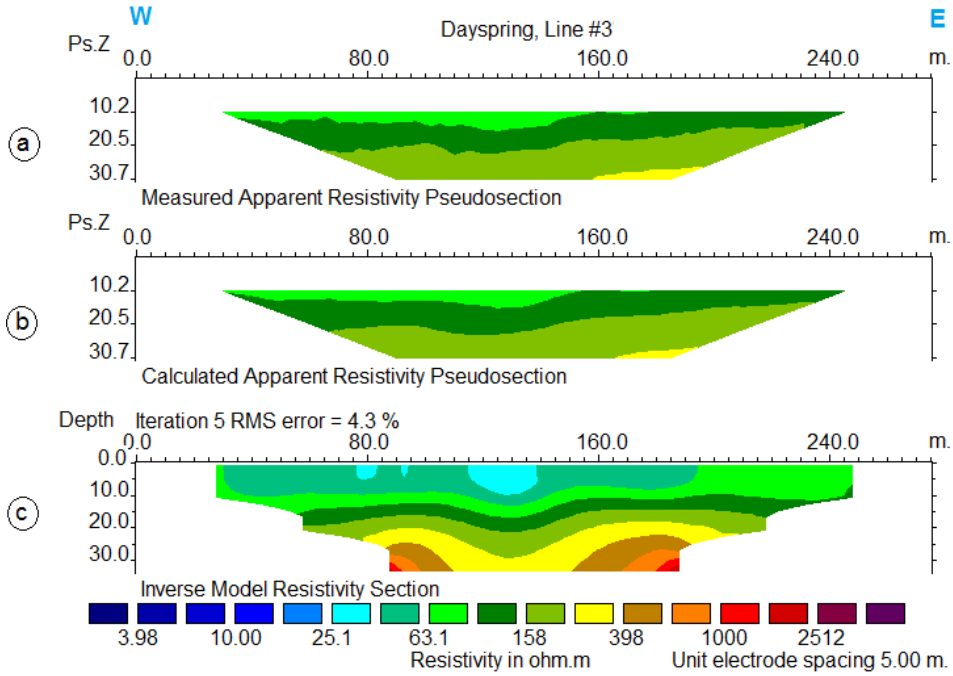

Figure 4.4. Electrical image along line 3.

2010 results and interpretations

Figure 4.5 shows the image measured along line 1b in Figure 4.1, repeated after ~ 6 months at the end of the rainy season, but extended to the north by 95 m. The measured data (Figure 4.5a) shows a gentle rise in apparent resistivity to the south, and the apparent resistivity drops steeply at the 320 m mark. The apparent resistivity also increases with depth. The measured and calculated (Figure 4.5b) data show low rms error of 2.6%. The inverted data (Figure 4.5c) shows lateral changes in resistivity of the regolith, which may indicate changes in lithology. The structure of the regolith and the bedrock appears to be similar to Figure 4.2, though there are subtle differences because of the difference in moisture content.

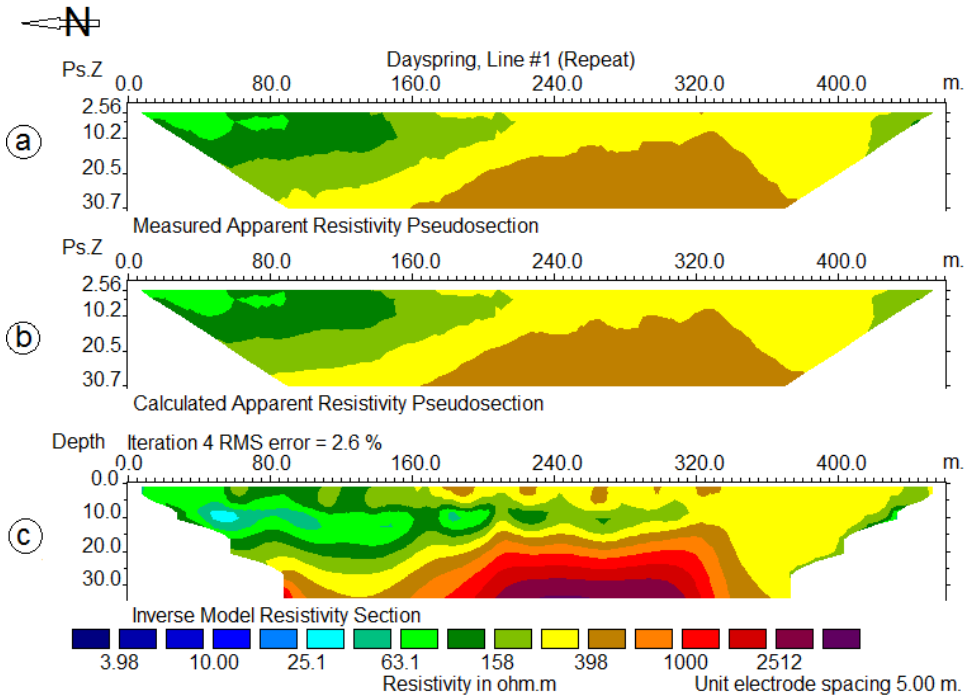

Figure 4.5. Electrical image along line 1 (repeated in March 2010).

Figure 4.6a and 4.6b show little differences when contrasted with a naked eye. Figure 4.6c shows a difference plot between Figures 4.5a and 4.5b. Notice the position of the yellow wattle and the bluegum trees on the surface. The low rate of resistivity decrease of the top regolith below the bluegum and yellow wattle trees could reflect the impact of these on groundwater, especially the bluegum. The 5% resistivity increase of the bedrock reflects that the bedrock may have dewatered during the rainy season probably because it maybe fractured and/or fissured. The vertical features depicted by the 10% decrease in resistivity may be fractures.

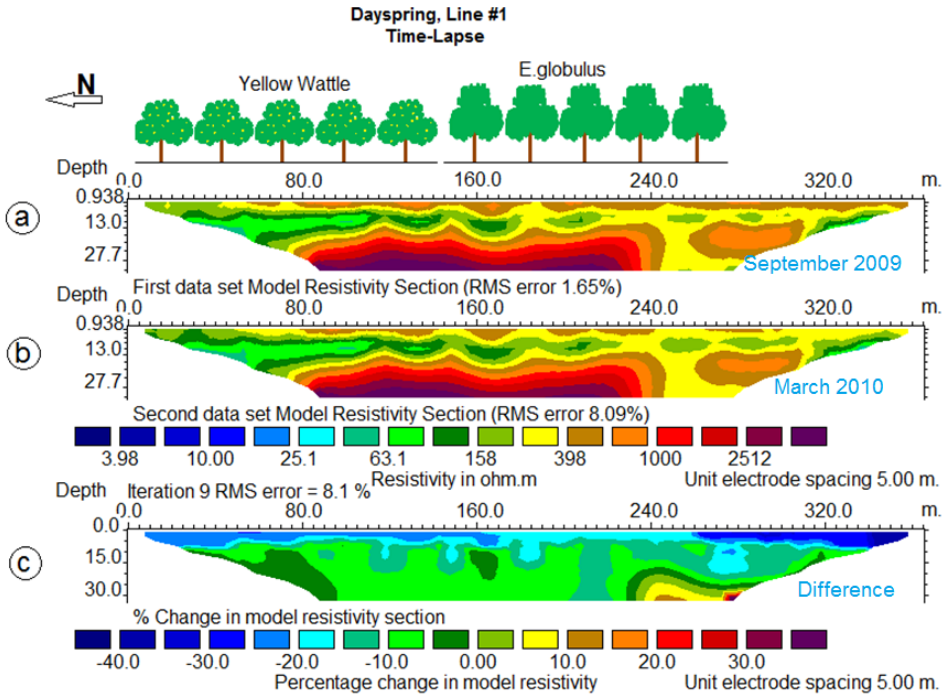

Figure 4.6. Electrical resistivity monitoring along line 1. (a) Initial data set and (b) time-lapse data set. (c) Difference plot between the two periods.

Figure 4.7 shows the repeat image measured along line 2b in Figure 4.1, repeated at the end of a rainy season in March 2010. Line 2 and its repeat line are not parallel but at proximity, hence Figure 4.7 is slightly different from Figure 4.3, especially between the 0 m and the 160 m marks. The difference in resistivity to the north could be due to a rock that is slightly weathered to towards Line 2a (Figure 4.3) and more competent towards line 2b (Figure 4.7). Otherwise, the data are repeatable which means that they honour the subsurface structure.

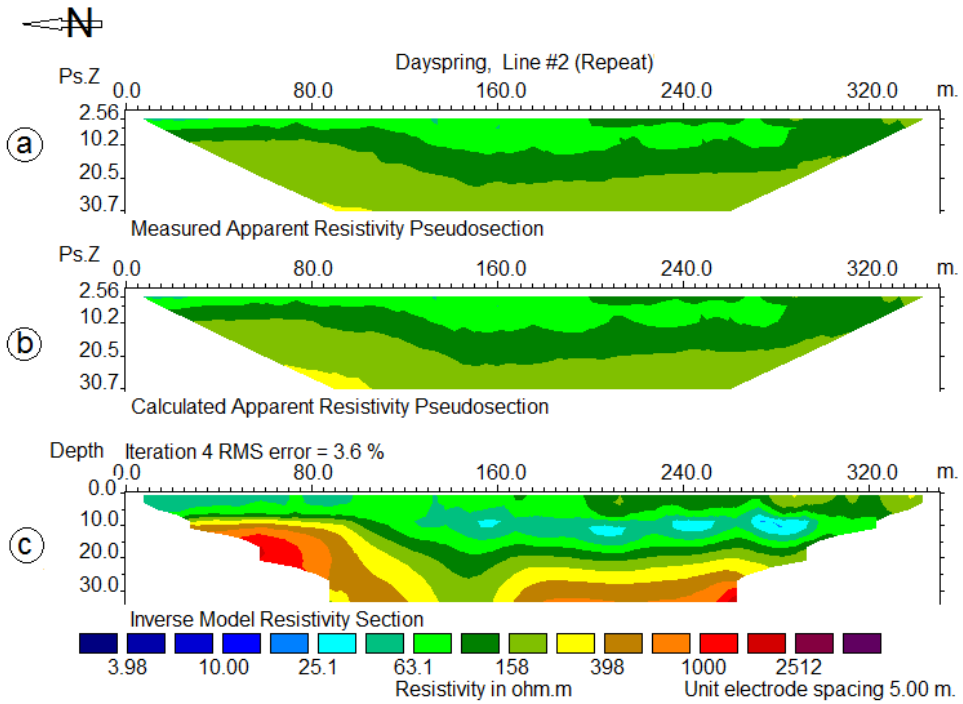

Figure 4.7. Electrical image along line 2 (repeated in March 2010).

4.2 Time-domain electromagnetic surveys at Dayspring School

4.2.1 Introduction

Fugro Airborne and Council for Geosciences collected the airborne and ground time-domain (TDEM) data respectively. I was part of the crew in collecting the ground TDEM data.

The time-domain electromagnetic method has been used extensively for hydrogeophysical exploration (e.g. Palacky, 1981; Fitterman and Stewart, 1986). This method has been used among other things to map geology (Palacky, 1981) and/or groundwater (Fitterman and Stewart, 1986). The weathered layer is one of the sources of electromagnetic anomalies (Palacky, Ritsema and Jong, 1981); hence, mapping the weathering patterns is an indirect way of mapping the geology because the weathered layers are derived from underlying parent rocks. In hard rock environments like Dayspring School, groundwater exploration includes mapping depth to the bedrock, locating fracture zones, and mapping bedrock depressions (McNeill, 1991). While recognizing the work of De Beer et al. (1991) and most recently Tessema et al. (2011), there is little published work that has been done in South Africa, especially in the region of the study area.

4.2.2 Basic principles of the TDEM method

The electromagnetic method depends on the conductivity contrast of the geologic formation below the surface. In time-domain, a steady current is allowed to flow in a conductive loop for a limited time and switched off instantaneously. According to Ampere's law, the current in the loop induces a primary magnetic field. The sudden termination of the current in the transmitter loop, in accord to Faraday's law, induces an emf that drives eddy currents in the nearby conductive earth. When the eddy currents decay – which depends on the conductivity, size and shape of the conductor – a proportional secondary magnetic field is induced. The secondary magnetic field tends to maintain the total primary magnetic field; hence the eddy currents assume the shape and direction of the steady current in the transmitter loop before off time.

The image currents of the steady current diffuse downward and outward while their amplitudes diminish. A receiver loop measures the time rate-of-change of the secondary magnetic field, i.e., $d\boldsymbol{B}_s/dt$.

4.2.3 Airborne TDEM

4.2.3.1 *Materials and methods*

Description of the equipment and materials employed.

Fugro Airborne, South Africa, using GENESIS, a TEMPEST EM system, collected the airborne data. A full description of the instrument can be found in Lane et al. (2000).

Explanation of the way in which the work was done.

The airborne data were collected as part of pilot training exercise in 2010 (Webb et al., 2011). Although the dominant strike of the geology is east-west, and ideally, the lines should have been flown north-south; this could not be done because of the presence of the nearby Magaliesberg Mountains directly to the north. These mountains strike east-west and rise rapidly from the floor of the valley to over ~200 m. Thus for safety reasons the decision was made to fly the lines east-west. A flight height of 90 m was used to avoid powerlines and tall trees. A total of 11 lines (~5, 480 m long) were collected with line spacing of 50 m (Figure 4.8). System and work specifications are summarized in Table 4.1.

Figure 4.8. This image shows the survey lines of the TDEM and magnetic data measured by Fugro Airborne, South Africa.

Table 4.1: Genesis system specifications as provided by Fugro.

Base frequency	75 Hz
Transmitter area	134 m^2
Transmitter turns	1
Waveform	Square
Duty cycles	50 %
Peak current	450 A
Peak moment	60 300 Am^2
Average moment	30 150 Am^2
Receiver sample rate	153.6 kHz
Receiver samples per half cycle	76.8 kHz
System bandwidth	Base frequency to 50.0 kHz
Flying height	90 – 100 m (subject to safety audit)
EM sensor	Towed bird with 3 orthogonal coils (X and Z processed)
Tx-Rx horizontal separation	85 m
Tx-Rx vertical separation	45 m
Stacked data output interval	200 ms
Number of output windows	13
Magnetometer	Stinger-mounted cesium vapour
Magnetometer sampling rate	Nominal 150 Hz, processed to 10 Hz
Digital video resolution	352 x 288 pixels
Digital video sample rate	2 Hz
Receiver	$FASDAS_{EM}$ (integrated real time processing)

4.2.3.2 ***Experiments and results***

Description of the experiment

Fugro airborne did all the processing (but not inversion) of the data and prepared a Geosoft database. They then gridded the data to produce the apparent conductivity maps of the region. The regional maps were then masked to sizes that were just a few

of meters outside the Dayspring school property, so that the subtle conductivity anomalies at Dayspring were not be masked by higher amplitude conductive anomalies elsewhere.

Description of the results

Figure 4.9 shows the z-component TEMPEST data for window 1 (0.019 ms), 2 (0.045 ms), 3 (0.070 ms), 4 (0.108 ms), 5 (0.172 ms), 6 (0.274 ms), 7 (0.439 ms), 8 (0.693 ms), and 9 (1.075 ms). The times corresponding to the different windows represent the center times between the start and end times. The airborne electromagnetic data were converted to conductivity, and are presented in parts per million (ppm). The colour scale is different in all cases, but red is resistive and blue is conductive. The image (Figure 4.9a) on Window 1 (0.019 ms ms) shows a high conductivity zone to the north coinciding with the mafic sills. High conductivity can also be seen to the extreme south. The intermediate resistivity on the image on window 1, shown in green, coincides with the area has boulders of hornfels. There is a low conductivity feature to the west running roughly north-south that corresponds to the syenite dyke and the powerline. On the Window 2 (0.045 ms) image (Figure 4.9b), a small zone of high conductivity develops in the middle of Dayspring School (outlined by the white polygon), meanwhile, the conductivity zone to the south migrates northwards. On the image (Figure 4.9c) on window 3 (0.070 ms), the conductive zone in the middle of Dayspring School becomes more strongly developed, and the conductive zone to the south migrates further to the north, while becoming smoother and thinner. The resistive zone to the west is strongly developed on the image for window 3. The image (Figure 4.9d) for window 4 (0.108 ms) shows that the northern conductive zone, the middle conductive zone, and the southern conductive zone are merging. The southern conductive zone becomes more smooth and thinner, while the resistive zone to the west begins to disintegrate slightly at position that is parallel to the merger of the southern and the middle conductive zones (Figure 4.9d). On the window 5 (0.172 ms) image (Figure 4.9e), a thin conductive zones running east-west develops across the resistive feature to the west. The east-

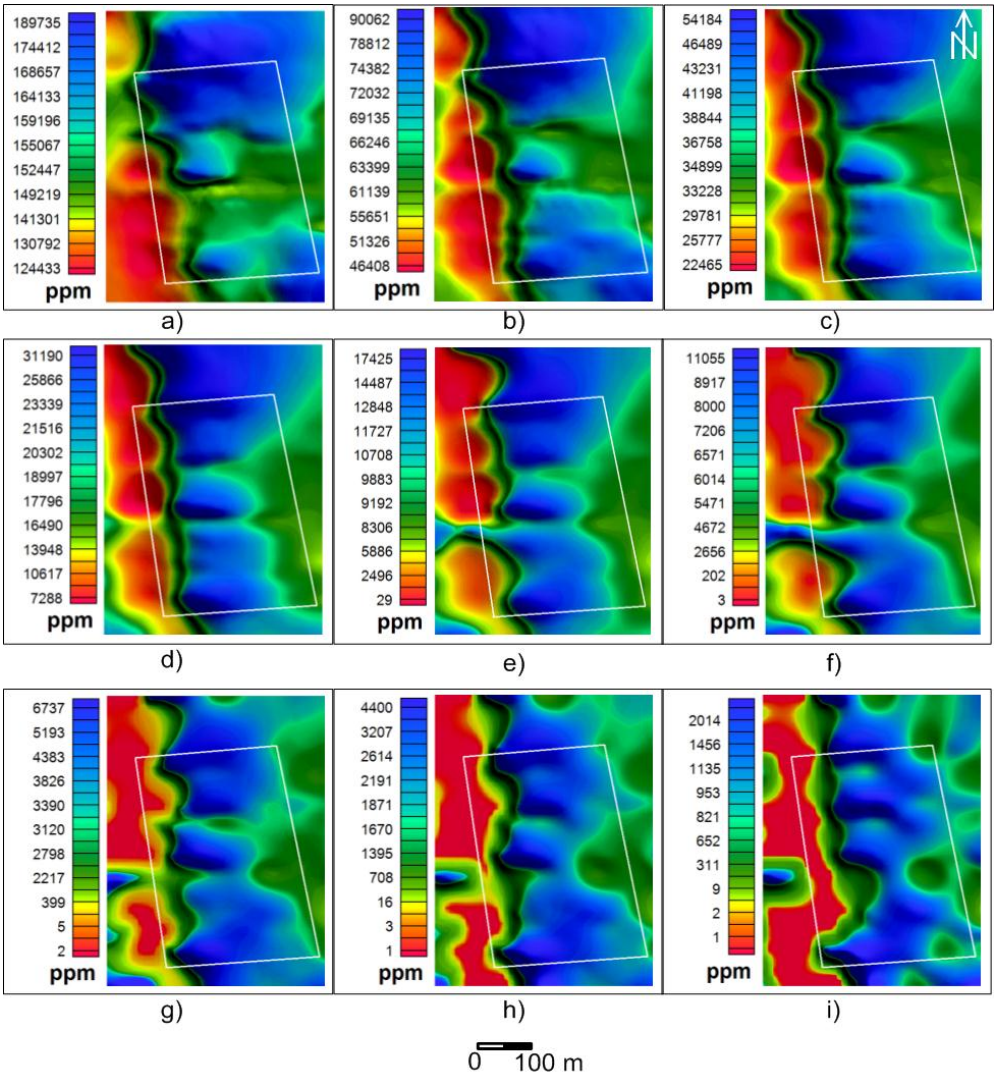

Figure 4.9. The apparent conductivity map derived from the TEMPEST z-component data. The data presented in ppm. Panels (a) to (i) represent windows 1 to 9. The subsequent windows show noise. Blue is conductive and red is resistive. The polygon that is superimposed on the grids outlines Dayspring School.

west thin conductive zone appears to be connected to the southern conductive zone, though the middle conductive zone and the southern zone still appears to be merged. On the window 6 (0.274 ms) image (Figure 4.9f), the east-west running feature is strongly developed. The southern conductive zone appears to be broadening to the

east on the window 6, image (Figure4.9f), while similar broadening trends are apparent on Figures 4.9g and 4.9h (window 7 (0.439 ms) and 8 (0.693 ms). By window 8 (0.693 ms) image (Figure 4.9h), the northern, the middle, and southern conductive zones more connected to form one continuous conductivity feature running north-south. The conductive thin feature running east-west is no longer evident on the images (Figure 4.9g to 4.9h) for window 7 (0.439 ms) to 9 (1.075 ms). The image on window 9 and the subsequent windows 10 to13 (1.660-5.585 ms) stars to show noisy data; hence, the subsequent images are not presented.

4.2.4 Ground TDEM

4.2.4.1 *Materials and methods*

Description of the equipment and materials employed.

The ground TDEM data were collected by the Council for Geoscience (CGS) using the TEM-FAST 48 HPC EM system. Barsukov et al. (2006) give a full description of this system.

Explanation of the way in which the work was done.

Data were collected in 2010 completing 45 soundings (Figure 4.10). A common square loop with a side length of 25 m was used. The station spacing, in the traverse direction, was 25 m as the loop was flipped over for the next sounding point. Survey specifications are summarized in Table 4.2. The position of each sounding point, which was in the center of the loop, was recorded with a hand-held GPS. The central position was selected by walking 12.5 steps along a side of the loop, then another 12.5 steps in the orthogonal direction to the opposite side. The hand-held GPS has an accuracy of ~5 m.

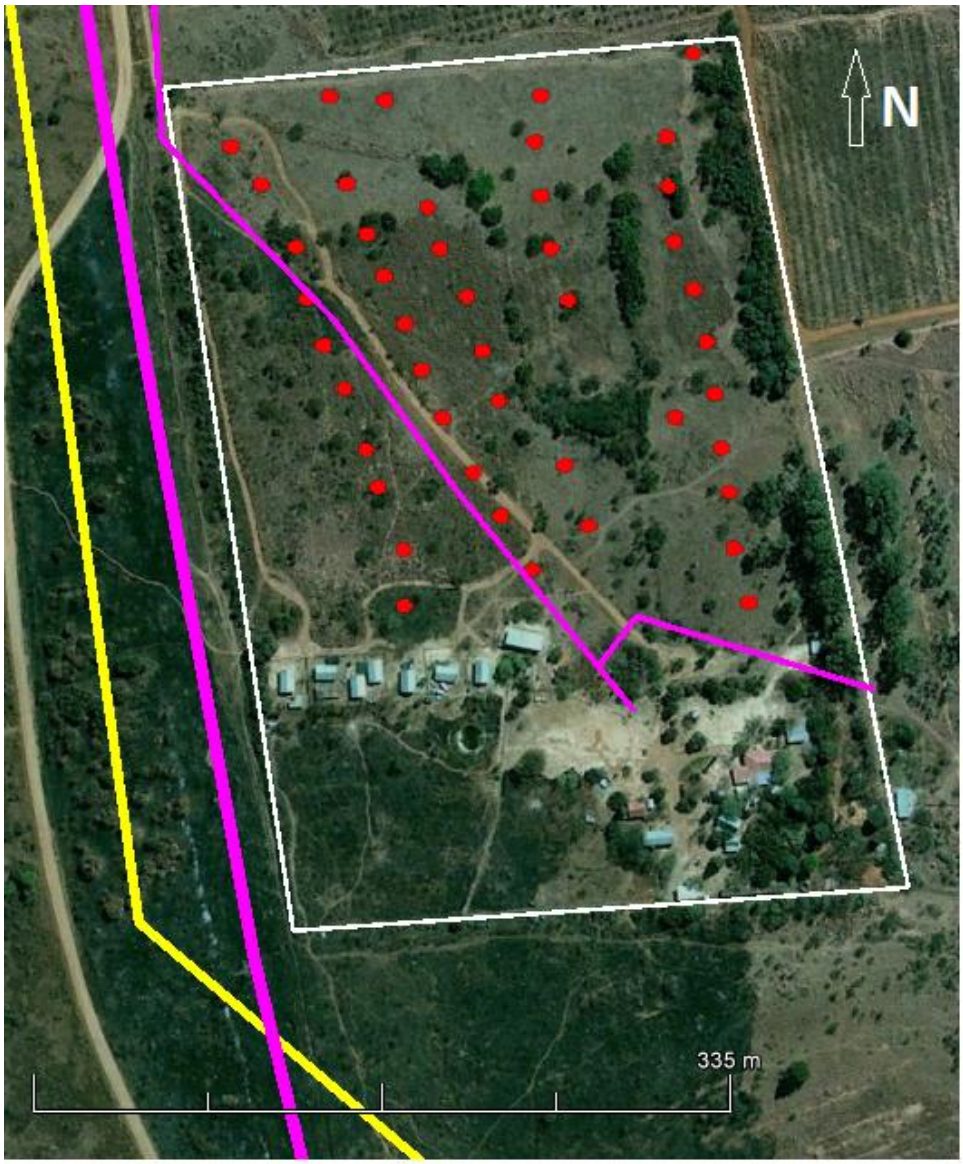

Figure 4.10. The dots represent the positions of the ground TDEM sounding points. The yellow line represents a syenite dyke while the purple lines represent the powerlines, with bold representing the big powerline.

Table 4.2: TEM-FAST survey specifications.

Time-range	5 µs
Stacks	4
Deff	3 µs
Transmitter current	1.0 A
Filter	50 Hz
Amplifier	Off
Tx loop	25 m
Rx loop	25 m

4.2.4.2 ***Experiments and results***

Description of the experiment

The field specifications can be seen in Table 4.2. The data were downloaded at the Council for Geoscience and were given to me via E-mail. The data were arranged in iso-channel/ window form related to the GPS positions of the soundings. Geosoft was used to grid the iso-channel data to produce apparent conductivity maps of the study area. It should be noted that this type of imaging is not iso-depth, but iso-times of the response. The log of the apparent conductivity was gridded so that negative value could be rejected. According to Barsukov et al. (2006), the negative values could be due to a thin conductive (resistivity less than 20-40 Ω·m) layer overlying a more restive rock mass with resistivities of greater than 300-500 Ω·m. Other source of the negative values could be weathering cores in crystalline rocks and faults (Barsukov et al., 2006).

Description of the results

Figure 4.11 shows the z-component TEMFAST data for window 1 (0.004 ms), 2 (0.005 ms), 3 (0.006 ms), 4 (0.007 ms), 5 (0.009 ms), 6 (0.011 ms), 7 (0.013 ms), 8 (0.015 ms), 9 (0.017 ms), 10 (0.022 ms), 11 (0.026 ms), 12 (0.030 ms), 13 (0.035 ms), 14 (0.043 ms), 15 (0.051 ms), 16 (0.059 ms), 17 (0.071 ms), 18 (0.090 ms), 19 (0.103 ms), and 20 (0.120 ms). The delay times above are the center times between the start and end times of a window. Blue represent conductive zones while red

represent resistive zones. The Window 1 (0.004 ms) image (Figure 4.11a) shows a conductive feature to the north that is conductive, which correspond to the mafic sills. Figure 4.11a also shows, a small conductive feature to the south of the gridded data, running north-south. The high apparent resistivity to the east correspond the area where there are large boulders of hornfels. On the window 2 (0.005 ms) image (Figure 4.11b), the conductive zone to the north is reduced on the eastern side, and the patchy conductive zone is also reduced. On window 3 (0.006 ms) image (Figure 4.11c), the northern as well as the small conductive zones appear to be greatly reduced. The windows 4 to 6 (0.006 - 0.011 ms) images (Figure 4.11d - 4.11f) show that the conductive zones continue to be reduced while a restive zone develops to the south and extends to the north. By window 6 (0.011 ms) image (Figure4.11f), the northern conductive zone has been reduced such that it appears to be north-south trending. On the window 7 image (Figure 4.11g), the resistive zone has exteded more to the north, surrounding the small conductive zone, which has been greatly reduced and its apparent conductivity has decreased. A less restive feature running northwest-southeast develops on the image (Figure 4.11h) of window 8. (0.015 ms). By window 9 (0.017 ms) image (Figure 4.11i), the feature running northwest-southeast is more developed. By window 10 (0.022 ms) image (Figure 4.11j), the small conductive feature at the southern part of the gridded data re-develops. On the window 11(0.026 ms) image (Figure 4.11k), the southern part of the gridded data is clipped because taking the log of negative apparent conductivity rejects such data points. Nevertheless, the image (Figure 4.11k) on window 11 (0.026 ms) shows the high resistivity zone extending to the north, whereby surrounding the less resistive small feature, whose size has been reduced greatly. By window 12 image, the low resistivity small feature is no longer evident. Figure 4.12m to 4.12t (window 13 to 20 (0.035-0.120 ms)) shows inconstant variations, and therefore will not be discussed because the abrupt changes in the data could be due to noise since these data were not inverted for true conductivity models.

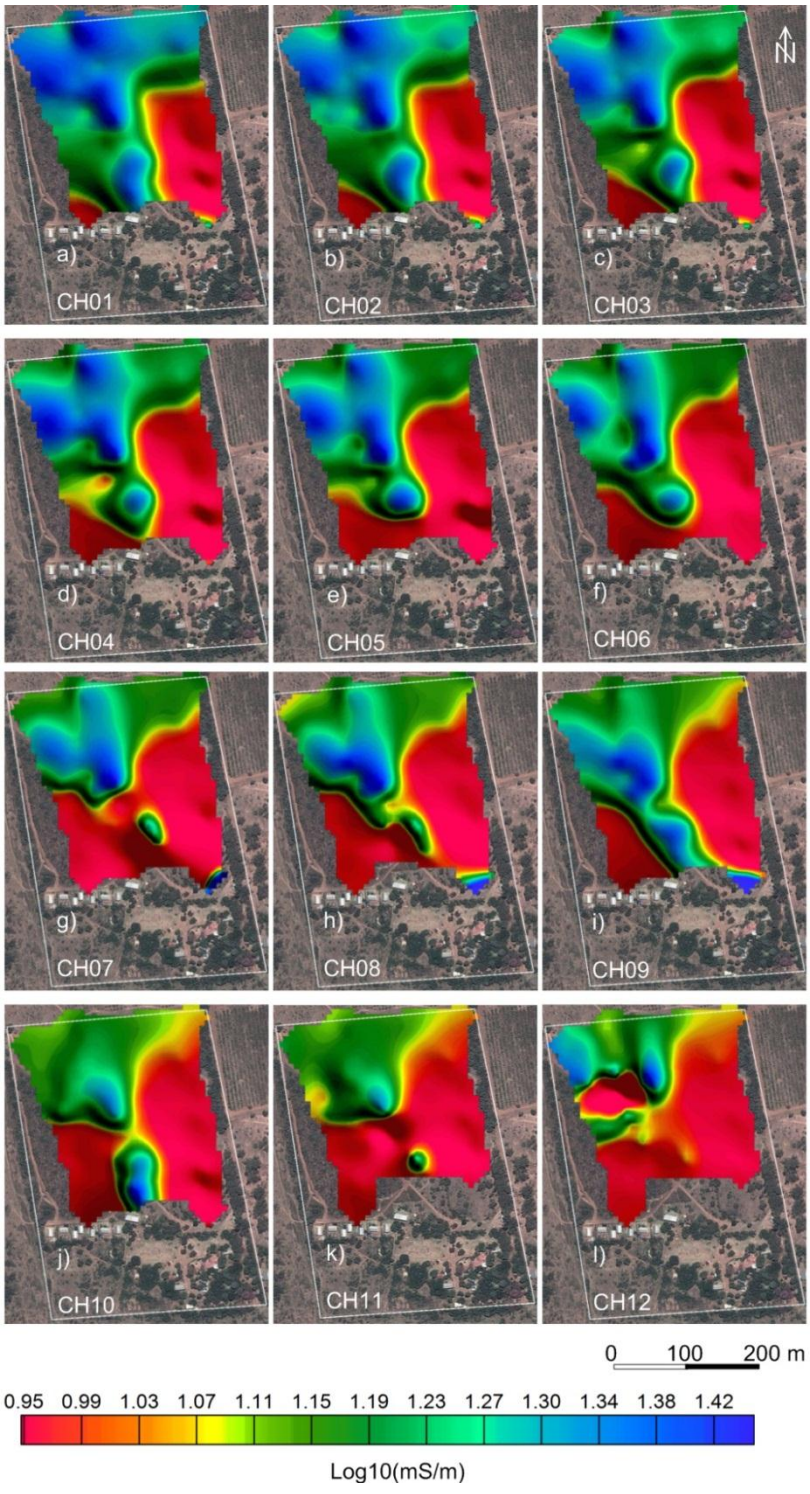

Figure 4.11. Apparent resistivity image derived from TEMFAST z-component. The panels show resistivities derived from window 1(CH01) to window 12(CH12). Blue is conductive and red is resistive.

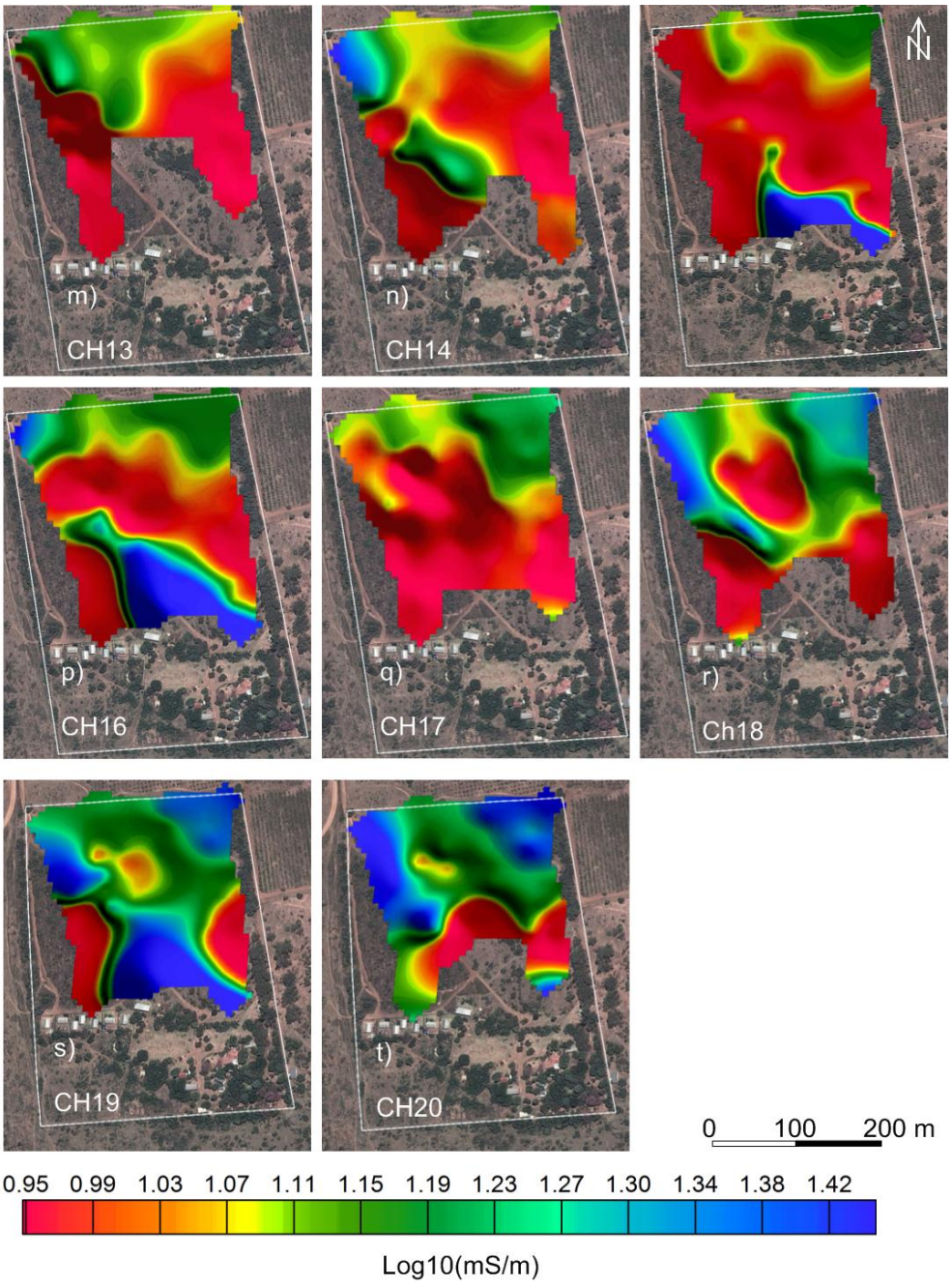

Figure 4.12. Apparent resistivity image derived from TEMFAST z-component. The panels show resistivities derived from window 1 (a) to window 20 (j). Blue is conductive and red is resistive.

4.2.5 Discussion of results

Comparisons of the two data sets prove to be difficult because the traverse lines used to acquire data were different. Nevertheless, some good comparison can be drawn from the two data sets. The ground and airborne data show that there is a conductive zoneto the north. This conductive zone could be due to a mafic sill as there are outcrops of feldspathic pyroxenite in this area. The low resistivity in the middle of the data derived from TEMFAST can also be seen in the data derived from TEMPEST, whose trend is generally north-south. The apparent resistor to the west in Figure 4.9 is probably due to a combination of the residual effect of the power line (after processing) as well as the response of the syenite dyke. The syenite dyke further to the left does not show a resistivity low (Figure 4.13), which suggests that the resistivity low that coincides with the powerline and the syenite dyke is due to the combination of effect of the powerline and the dyke. Lane et al. (1998) have acknowledged that if the receiver is close to a powerline, the magnetic fields associated with the powerline may result in imperfect cancellation of the response of the powerline.

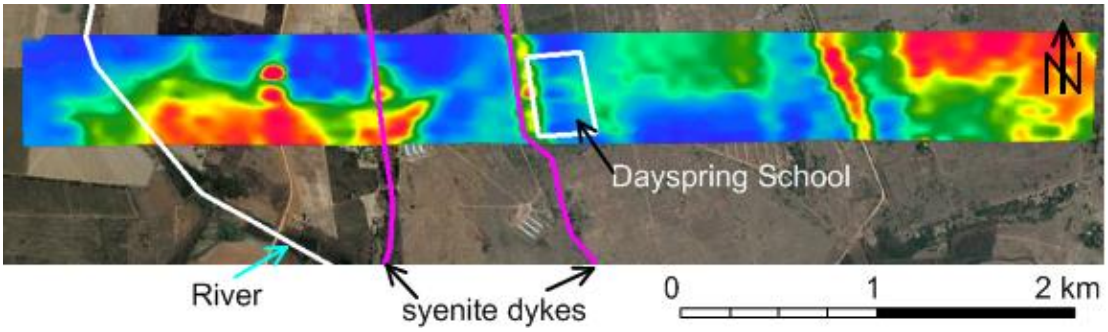

Figure 4.13. The apparent conductivity map derived from the TEMPEST z-component data of window 3. The map shows a river and syenite dykes superimposed on it.

The data derived from the TEMPEST and TEMFAST suggest there are at least two lithologies in the study area, the conductive mafic sills to the north and the resistive hornfels to the south. The low resistive feature in the middle could be a feldspathic pyroxenite that cuts across the hornfels.

4.3 Microgravity surveys at Dayspring School

4.3.1 Introduction

This method was used by Lee (2011) to map lithology changes and quantify time-lapse gravimetric changes due to water changes. The gravity method has been used extensively over many years to map the depth to the bedrock (e.g. Bohidar et al., 2001). Others have used this method to monitor aquifer storage recovery systems and water distributions, among other things, by doing time-lapse gravity (Davis et al., 2008). Time-lapse gravity includes looking at small amplitude gravity variations. These small amplitude changes are usually related to groundwater fluctuations, and are referred to as microgravity.

Microgravity is a useful tool for monitoring variations in the subsurface moisture and aquifers, hence a good tool in charactering aquifers. Microgravity refers to small magnitudes of gravity anomalies (Kirsch, 2006). These small magnitudes are often expected in the case of groundwater exploration and vary with time, caused by changes of the groundwater table or changes in soil moisture (Kirsch, 2006). Time dependent gravity measurements can be used to map and quantify aquifers by producing varying amplitudes of gravity anomalies in the same positions, but at different times (Kirsch, 2006). A gravity anomaly of about 0.0043 mGal caused by a rise of the groundwater table of 1m was, for example, detected in Bandung/Indonesia and Kyoto/Japan (Kirsch, 2006). Moreover, gravity changes, between 0.01 and 0.035 mGal, associated with land subsidence due to withdrawal of groundwater were observed (Kirsch, 2006). Davis et al. (2008) used time-lapse microgravity to detect the distribution of injected water as well as its general movement in an artificial aquifer in Leyden, Colorado.

4.3.2 Basic principles of the gravity method

The gravity method depends on density contrasts of the geologic formation below surface. Density excess will produce a positive anomaly while density deficiency will produce a negative anomaly. Therefore, an increase in density is related to increase in

mass for a constant volume. The unit for gravity is mGal. Gravity data should be corrected for terrain, drift, latitude variations, elevation and topographical effects.

The data are reduced so that the anomalies observed are due to either local density excess or deficiency. Gravity measurements would yield different results at the same position at different times of the day, thus the data should be corrected for instrument drift and tidal effects. The terrain is not always flat, there are hills and valleys, and the contributions of these elevation and topographical effects to the measured data should be removed by performing the free-air and Bouguer corrections. The radius of the Earth at the poles is different to the one at the equator, so gravity pull at this places is different, hence the data should be corrected for northing traverses (latitude variations). Large objects (e.g., mountains) will also contribute the measured gravity value; therefore, terrain corrections should be performed.

4.3.3 Materials and methods

4.3.3.1 **Description of the equipment and materials employed.**

The Scintrex CG-5 was used to collect the gravity data. This instrument has an accuracy of ± 5 µgal, and it does real time tidal and drift corrections. Lee (2011) corrected the data. The data were corrected for elevation changes (free air and Bouguer) and latitude (theoretical gravity) by means of a spreadsheet, and the processed data were imaged using Geosoft. The data were modeled using grav2d software. The real time kinematic differential GPS (DGPS) was used was used for x, y and z positions. The DGPS has an accuracy of ~1 cm.

4.3.3.2 **Explanation of the way in which the work was done.**

Lee (2011) collected the initial data in April 2011, towards the end of rainy season, for her project as part of the honours degree at the University of Witwatersrand (Figure 4.13). S.J. Webb and S.E. Scheiber (personal communication, 2011) collected the time-lapse data in September 2011 (Figure 4.14), at the end of dry season, because Lee (2011) could not do it due to time constraints. The repeat measurements were collected at the same position as the initial measurements by following markers

on the ground and GPS coordinates of the initial measurements. A station and line spacing of 20 m were used, and ~ 300 data points were collected. Traverse lines were north-

Figure 4.14. This image shows the gravity survey stations. The lines start from line 6 to the west to line 17 to the east represented by the dots.

south, orthogonal to the outcrop of mafic sill. A base station was chosen on an outcrop so that ground movement would be insignificant, hence a good reference point for reduction of the data. The base station measurements were collected at regular intervals of three hours; the measurements taken between any two base station

measurements comprise an internal loop. External measurements were also collected by repeating some of the previously measured points. A hand-held GPS was used to navigate the grid points and a DGPS was used measure the elevation component of the grid points.

4.3.4 Experiments and results

4.3.4.1 Description of the experiment

The gravimeter was leveled at every station such that the instrument tilt was within a diameter of up to 10 units. A smiley face would be displayed on the instrument screen to confirm that the tilt is within the diameter. A measurement stack of three was used while the measuring cycle of 60 seconds in measurement was used. Densities of the loose boulders and outcropping mafic sills were also measured.

Reduction of gravity data

The reduction of the data were performed using an excel spreadsheet. The data were corrected for drift notwithstanding that the CG-5 has built-in drift corrections. Topographical effects were removed by performing the free-air and Bouguer corrections. The data were also corrected for northing traverses while corrections for terrain effects were not performed. All gravity values were reduced to Bouguer anomalies and were gridded using Geosoft to produce two Bouguer gravity maps.

4.3.4.2 Description of the results

Figures 4.15 and 4.16 show Bouguer gravity map of Dayspring School in Figure 4.13. Figure 4.15 shows traverse line striping, which cannot be accounted for. However, two discrepancies may have contributed to the striping: (1) the data were collected over a longer period, and (2) the differential GPS measurements were collected four months after the gravity measurements; or the striping could have arisen from errors in the reduction of the data. Nonetheless, the two data sets are comparable.

The most prominent boundary to the north striking virtually east-west, separating gravity high to the north and gravity low to the south, outlined by the -0.32 mGal (yellow), is in the vicinity mafic sill outcrops. The gravity lows, -0.63 to -0.47 to the south correspond to the houses at Dayspring, but the decrease at this area could be due to a lithological change. Because of the striping in the data that were measured in April, a time-lapse map cannot not be used to compare the two data sets, because there would be no guarantee that the differences in the data is solely to due changes in the mass of water.

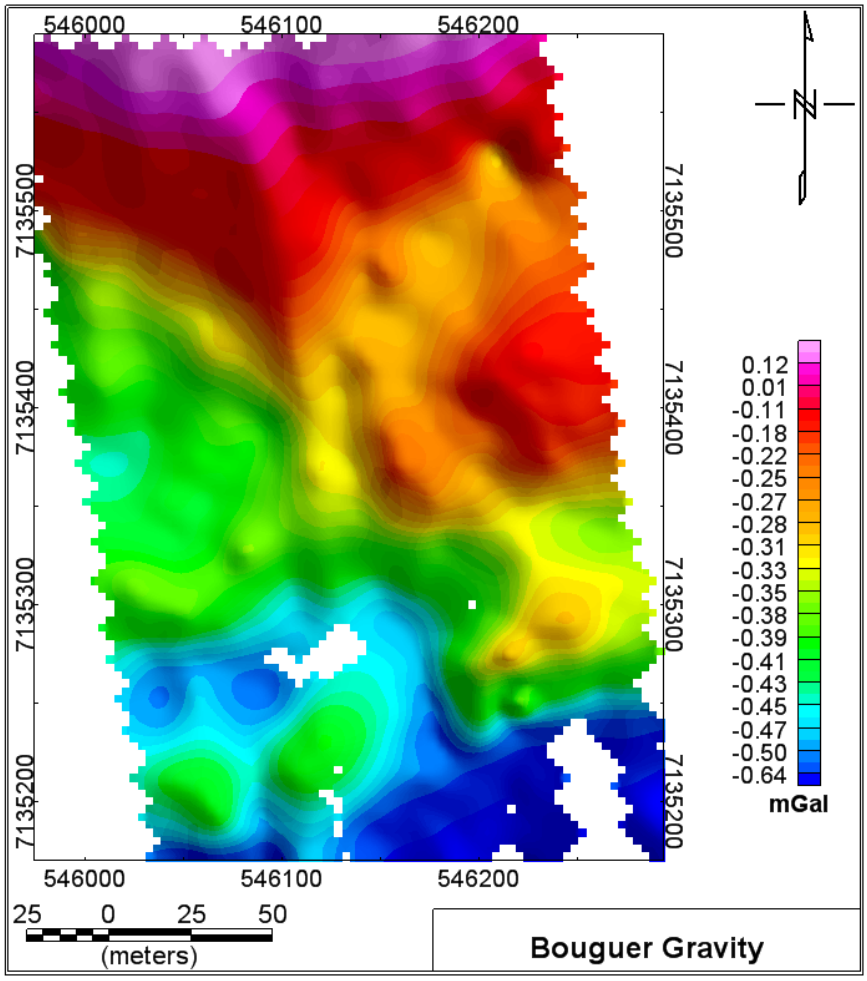

Figure 4.15. Bouguer gravity data derived from the CG-5 in April 2011 (Lee, 2011). The datum is WGS 84, the grid is UTM, and the zone is 35S.

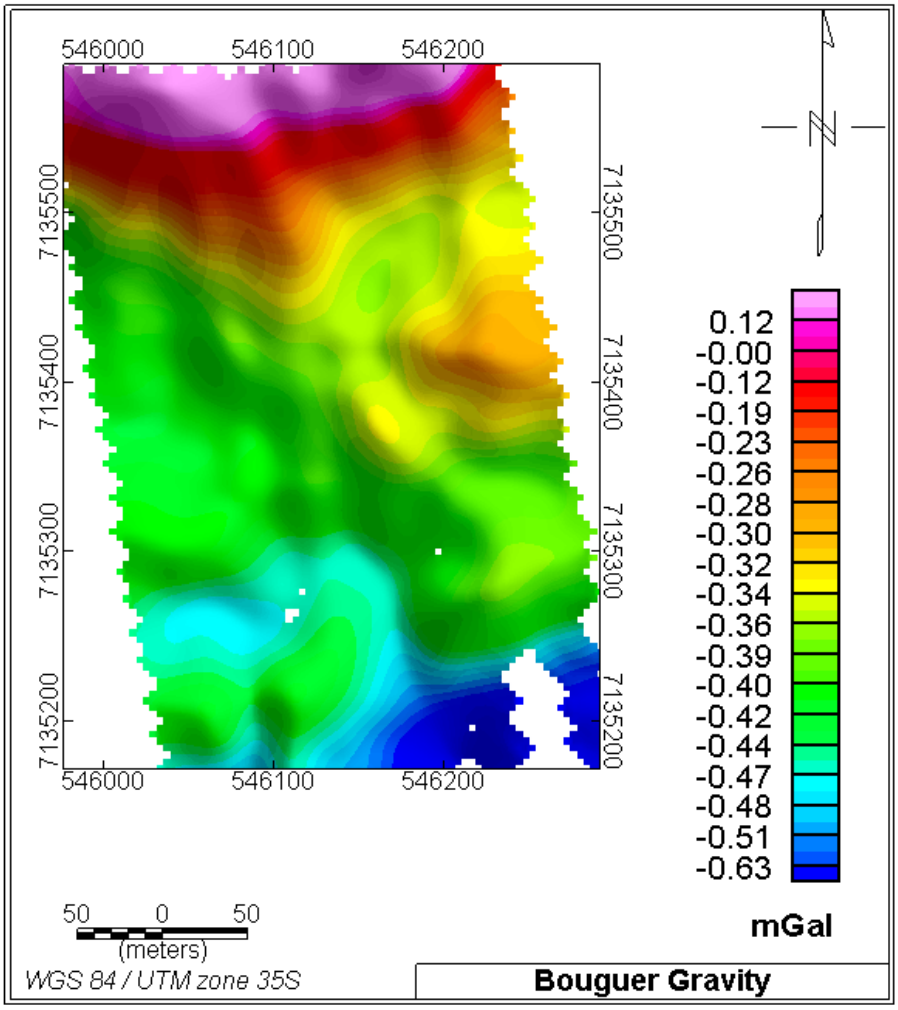

Figure 4.16. Bouguer gravity data derived from the CG-5 in October 2011 (Lee, 2011).

4.3.5 Discussion of results

Button (1973) reported the occurrence of mafic sills with hornfels in the Silverton Formation. The base station that was used to reduce the data was chosen to be an outcrop of feldspathic pyroxenite. The measured feldspathic pyroxenite at Dayspring School has an average density of 2.95 g/cm^3 while the boulders of hornfels have an average destiny of 2.70 g/cm^3 (Lee, 2011). Therefore, negative values indicate gravity low of hornfels with respect to the feldspathic pyroxenite.

The gravity method has mapped two lithologies, mafic sill to the north and hornfels to the south. The interpretation is based on outcrops of feldspathic pyroxenite and

loose boulders of hornfels that have been observed (Figure 2.2) as well as the measured densities. A few of trenches also show boulders of hornfels. The density of hornfels ranged from 2.59 to 2.75 g/cm^3 (Lee, 2011), therefore, the Bouguer gravity lows by the houses could still be a hornfels of different densities. The gravity high in orange peaking at 546200E and 7135400N could be a shallower hornfels. The sharp end of the mafic sill in the middle of Figures 4.14 and 4.15 may indicate that there may be a thin continuation of the mafic sill to the south.

4.4 Magnetic surveys at Dayspring School

4.4.1 Introduction

This method was used by Sepato (2011) to investigate structures at Dayspring. collected the ground magnetic data in a parallel study while Fugro Airborne collected the airborne data. The use of magnetic to map geological structures has been done extensively in South Africa (e.g., Hales and Gough, 1959; Stettler, 1979). The magnetic methods can locate geological structures in hard-rock environments such as faults, dykes and fractures, which could aid in groundwater exploration.

4.4.2 Basic principles of the magnetic method

Magnetic investigations produce data about the subsurface geological structures. It is measured in nano-Teslas (nT) as total magnetic field intensity (TMI) (Lowrie, 2007). Magnetic anomalies result from lateral variation in magnetic properties of rocks, i.e., when there is a contrast in magnetisation of rocks occurring next to each other, there will be a magnetic anomaly. Magnetisation of the body should be considered in terms of its shape and orientation as well as the inclination of the present day direction of the Earth's field. According to Telford et al. (1990), these anomalies can be large enough to double the main field. To produce a good anomaly map, one should know the diurnal variations of the geomagnetic field in space and time in the area of survey. The diurnal variations should be removed from the data before processing and interpretation.

4.4.3 Airborne Magnetics

4.4.3.1 ***Materials and methods***

Description of the equipment and materials employed.

The airborne magnetic data were collected together with the airborne TDEM as part of pilot training exercise in 2010 (Webb et al., 2011). The data were collected in 2010 comprising 11 lines with line spacing of 50 m and length of ~5480 m. The flight

height was 90 m and flight direction was east-west. They used the Stinger-mounted cesium vapour magnetometer and system specifications are summarized in Table 4.3.

Table 4.3: Genesis system specifications as provided by Fugro.

Base frequency	75 Hz
Transmitter area	134 m^2
Transmitter turns	1
Waveform	Square
Duty cycles	50 %
Peak current	450 A
Peak moment	60 300 Am^2
Average moment	30 150 Am^2
Receiver sample arte	153.6 kHz
Receiver samples per half cycle	76.8 kHz
System bandwidth	Base frequency to 50.0 kHz
Flying height	90 – 100 m (subject to safety audit)
EM sensor	Towed bird with 3 orthogonal coils (X and Z processed)
Tx-Rx horizontal separation	85 m
Tx-Rx vertical separation	45 m
Stacked data output interval	200 ms
Number of output windows	13
Magnetometer	Stinger-mounted cesium vapour
Magnetometer sampling rate	Nominal 150 Hz, processed to 10 Hz
Digital video resolution	352 x 288 pixels
Digital video sample rate	2 Hz
Receiver	$FASDAS_{EM}$ (integrated real time processing)

4.4.3.2 ***Experiments and results***

Description of the experiment

Fugro airborne did all the processing of the data and prepared a Geosoft database. I gridded the data to produce the total magnetic intensity map of the region. The regional map was then masked to a size that was just a few of meters outside the Dayspring school property, so that the subtle magnetic anomalies at Dayspring would not be masked by higher amplitude magnetic anomalies elsewhere.

Description of the results.

Figure 4.16 shows the total magnetic intensity map of the study area derived from the airborne magnetic survey. Blue are magnetic lows and pinks are magnetic highs. The airborne data were collected east-west and therefore delineate north-south features well such as the north-south powerline and the river to the west in Figure 4.17. Unfortunately the geologic strike is east-west and hence the boundary between the mafic sills and the hornfels could not be resolved by the airborne magnetic data (Figure 4.18). The magnetic low the west in Figure 4.18 coincides with the syenite dyke and the big powerline in Figure 4.17. The lowest magnetic intensity to the west coincides with a river. There is no outcrop or boulders coinciding with the regional magnetic high of ~28300 nT in pink peaking at 546100E and 7135500N in Figure 4.18. However, this magnetic high is bounded to the north by the outcrop of feldspathic pyroxenite and to the south by boulders of hornfels (Figure 2.2).

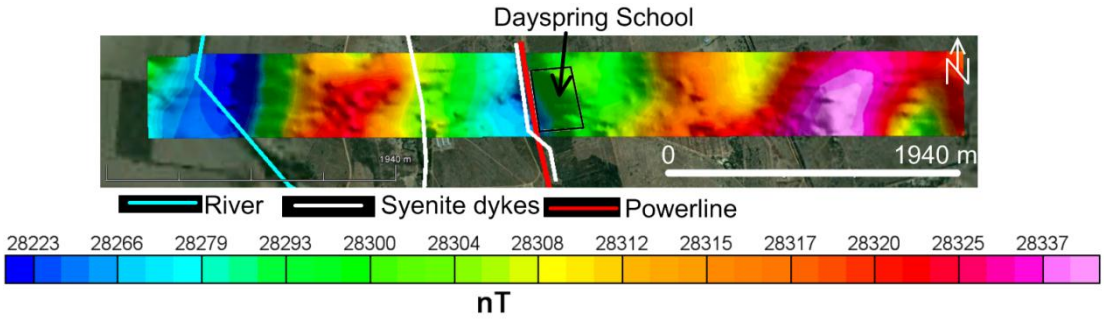

Figure 4.17. The airborne regional magnetic intensity map.

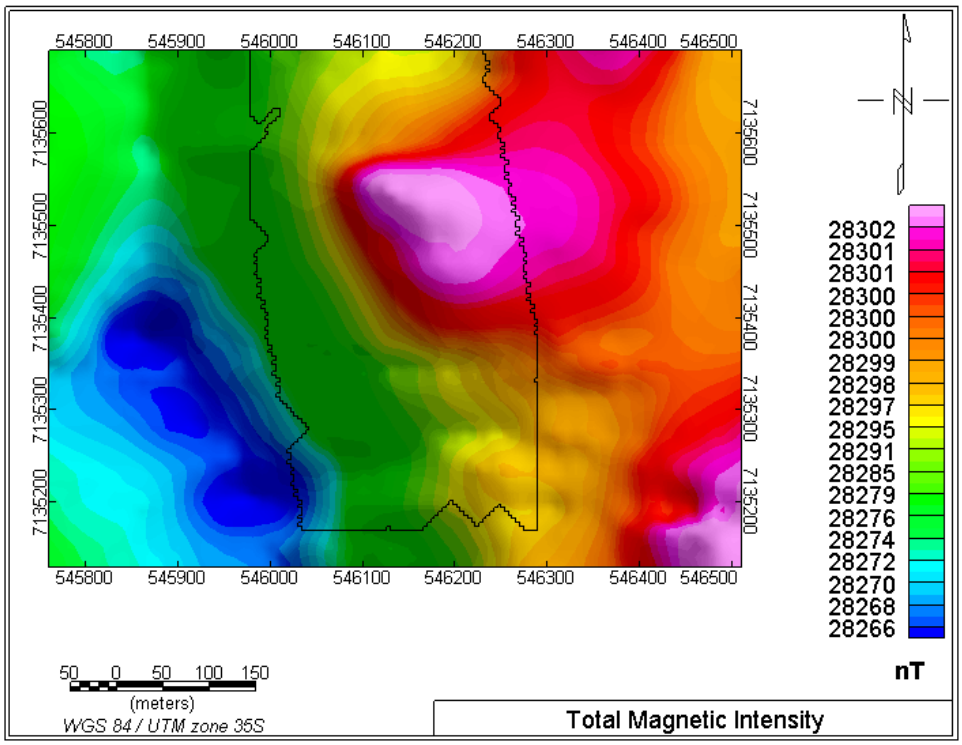

Figure 4.18. The zoomed-in airborne magnetic intensity map. The outline superimposed on the map is the ground magnetic grid.

4.4.4 Ground magnetics

4.4.4.1 *Materials and methods*

Description of the equipment and materials employed.

The instruments used were proton precession magnetometers and hand-held geographic positioning systems (GPSs). The proton sensor has an electric coil mounted in a liquid that has protons (hydrogen nuclei). When an electric current is switched on, an electric current flow in the coil and it creates a magnetic field. The protons in the fluid align themselves in the direction of the induced field. When the current is switched off, the protons begin to precess in the direction that is perpendicular to the direction of the Earth's field. The protons precess at an angular frequency known as the Larmor precession frequency, which is proportional to the

magnitude of the magnetic field. Since proton precession magnetometers do not drift, a separate base station can be used to measure diurnal variations.

Explanation of the way in which the work was done.

Sepato (2011) collected the ground magnetic data as part of the honours degree at the University of the Witwatersrand. The data were collected in April 2011 within Dayspring property and the grid was extended north of Dayspring property in September 2011. The survey lines were 460 m long with line spacing of 20 m and station spacing of 5 m (Figure 4.19). The measurements were taken at regular intervals of 5 m along the lines. The lines were running perpendicular to the strike of the mafic sills so that the boundary between the sills and the hornfels could be delineated. There were two field magnetometers, one roving magnetometer, and a base station magnetometer. The roving magnetometer had a leading GPS and a tracking GPS. The following steps were carried out in all the surveys: (1) clear the memory of the magnetometers, (2) synchronize the magnetometers with the GPS, (3) tune the magnetometers to achieve best signal strength, (4) place the base magnetometer in a secure place, (5) check reliability of the data, and lastly (6) start taking measurements. Before the commencement of data acquisition, measurements were taken at one location to check the reliability of the readings and differences were found to be no more than 1 nT. The base station was set to take measurements automatically for every 60 seconds.

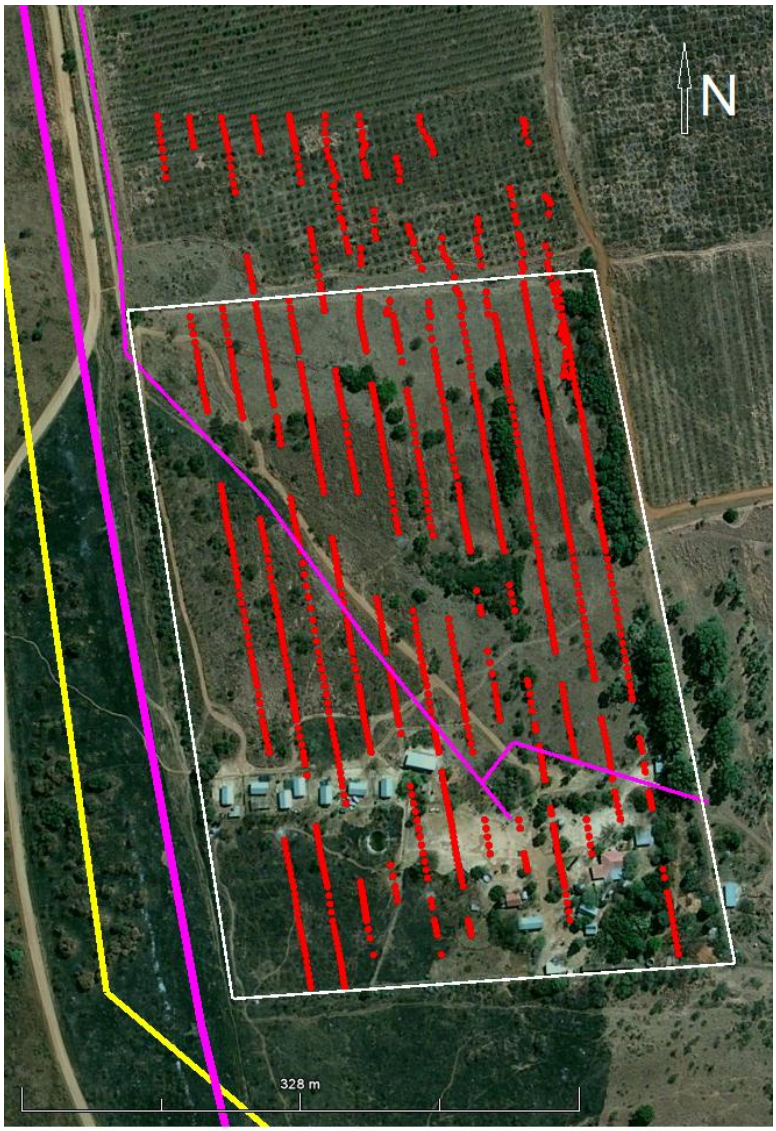

Figure 4.19. This image shows the ground-magnetics survey lines. The lines start from line 6 to the west to line 17 to the east represented by the dots.

4.4.5 Experiments and results

Description of the experiment

In the field, when all settings and checks were satisfactory, data acquisition would commence. The base station was stopped from recording measurements at the end of data acquisition.

In the office, data were downloaded and processed Sepato (2011) using Mag Map software, where diurnal variations were removed from the data. A careful de-spiking of data was performed by analyzing and correlating the observed spikes in data with the noted cultural features. Such features included fences, powerline and a Petronet gas pipe. The final processed data were gridded in Geosoft and a total magnetic intensity map of the study area was produced by Sepato (2011).

4.4.5.1 **Description of the results.**

Table 4.4 shows the average magnetic susceptibilities at Daypsring School. The standard deviation of the hornfels is high owing to a great difference in the measured magnetic susceptibilities.

Figure 4.20 shows the ground magnetic intensity map of Dayspring School. The data are noisy in the proximity of fences, Petronet gas line and powerline. However, the gridded data are free of the cultural noise as the data were de-spiked before gridding . The map shows two anomalous features, which are the high magnetic intensity to the north and the north-south striking feature. The magnetic high to the north corresponds to inferred outcrop of feldspathic pyroxenite. The dyke-like feature covers borehole DS2 of which the thin section derived from its borehole chips reveal that the rock type is rich in pyroxene, with minor feldspar and opaque mineral. The opaque mineral could be magnetite that is responsible for the high magnetic signature.

Table 4.4. Measured average magnetic susceptibilities (Sepato, 2011).

Lithology	$\kappa_{Avg.} \times 10^{-5}$ (SI)	Standard deviation
Syenite	6.85	4.0
Hornfels	41.4	20.5
Pyroxenite	28.2	0.8

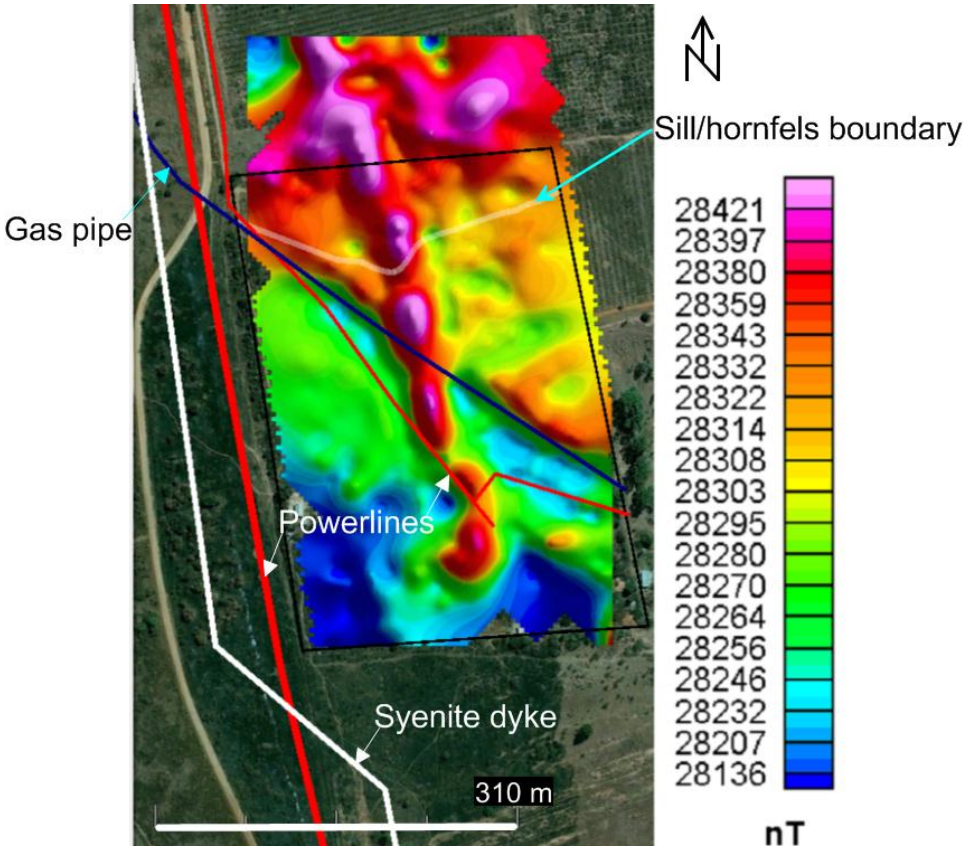

Figure 4.20. The ground magnetic map of Dayspring School. The mafic sill and hornfels boundary is based on the interpretation of gravity data (after Sepato, 2011).

4.4.6 Discussion of results

Although the data were not interpreted quantitatively, the ground magnetic data shows more detail than the airborne data as they are significantly closer to the source (2 m versus 90 m). Some of the differences between the ground and airborne data could be due to different traverse directions when the data were acquired. The fact that the north-south feature was not picked up by the airborne data suggest very strongly that this is a near surface shallow source. The lines were flown east-west and they are ideal for delineating north-south features (and do well on other features). Nevertheless, it is possible that the north-south feature, in the airborne magnetic data, was masked by the high amplitude of the big powerline. Nonetheless, the two data

sets managed to map the anomaly that shows up strongly as a magnetic high in the airborne data, though the anomaly has been masked by high amplitude anomalies in the ground data. The high standard deviation shown by the averaged magnetic susceptibilities derived from hornfels measurements may suggest that there is more than one type of hornfels at Dayspring School.

4.5 Hydrogeology surveys at Dayspring School

4.5.1 Introduction

Goba (2010) used this method, under the supervision of T. Abiye (personal communication, 2010) to characterize the hydrogeology of the Dayspring area.

Rainwater, upon falling on the surface, could evaporate and/or run off and/or infiltrate the ground. The amount of infiltration depends on subsurface porosity and saturation. Dayspring School falls in the region that had an average annual rainfall of 835 mm. Barnard (2000) estimated the annual evaporation of the region to be between 1600-1800 mm. When the soil is porous, more water will infiltrate and as the soil gets saturated, infiltration slows down and run off takes place or increases. The infiltrated water is pulled down by gravity until it rests on a non-porous and impermeable rock. A rock that is porous and is able to transmit water, but underlain by a layer of rock that is non-porous and impermeable is called an aquifer. Unconsolidated sedimentary rocks are good aquifers because of the high porosity and permeability while crystalline rocks are poor aquifers. In crystalline terrains, like Dayspring School, groundwater can be found in cracks, contacts, fissures and weathered layers.

4.5.2 Basic principles of the hydrogeology method

4.5.2.1 Groundwater Chemistry

Groundwater contains dissolved inorganic and organic constituents that were acquired from its present location and past movements (Todd and Mays, 2005). The concentration of organic compounds is usually small, less than 0.1 mg/ℓ, due to oxidation of organic matter to carbon dioxide during infiltration (Hiscock, 2005). Inorganic ions and compounds usually comprise more than 95% of the dissolved constituents (Fitts, 2002). Groundwater chemistry can be used to identify various aquifers.

Total dissolved solids

The degree of groundwater salinity is expressed as the total dissolved solids (TDS) (Hiscock, 2005). TDS depends on the rock type from which the solutes are derived and the length of time that the water was in contact with the rocks and soil (Fitts, 2002). More soluble minerals produce higher TDS. TDS is lowest at shallow depths because the water would have just infiltrated (Fitts, 2002). Igneous rocks show low TDS even after a long contact with groundwater because they are more resistant to weathering (Todd and Mays, 2005). TDS is directly proportional to electrical conductivity (Hiscock, 2005). TDS can assist in defining and characterizing the rocks forming the aquifers.

Acidity /Alkalinity (pH)

pH is a measure of the degree to which a substance is acidic or basic (Terwey, 1984). Carbon dioxide (CO_2) and aqueous carbonate compounds tend to dominate acid-base reactions (Todd and Mays, 2005). pH values that are in the range 0-7 indicate an acidic solution whereas solutions that are basic have a pH range of 7-14 (Todd and Mays, 2005). Acidic water will dissolve minerals upon contact with the rock or soil (Fitts, 2002). Therefore, the amount of pH in water will assist in explaining the salinity of groundwater at Dayspring School, i.e., high salinity would be expected in acidic groundwater.

Redox potential

Redox potential (expressed in mV) is a result of oxidation and reduction in chemical reactions. Oxygen is usually the oxidising atom, hence the name oxidation (Todd and Mays, 2005). An atom that accepts electrons in a reaction is said to be oxidising the atom that is donating these electrons. The electron donor reduces the atom that is accepting the electrons (Todd and Mays, 2005). Redox potential can be correlated with the amount of dissolved oxygen (Nelson, 2002). Rainwater is saturated in dissolved oxygen and as the water infiltrates deeper, the oxygen content drops and the environment becomes more reducing (Nelson, 2002). The redox potential will assist

in characterising and distinguishing between open and closed aquifers at Dayspring School by evaluating the oxygen content in groundwater.

Isotopes

Isotopes are atoms with the same number of protons (same atomic number), but different number of neutrons (different atomic mass). There are stable and non-stable (radioactive) isotopes. Groundwater contains environmental isotopes that can be used to characterise and trace waters through the hydrologic cycle (Terwey, 1984). Stable isotopes of water molecules, deuterium ^{2}H and ^{18}O and the radioactive isotopes, tritium ^{3}H and ^{14}C are usually analysed (Terwey, 1984). Stable isotopes are useful in determining water circulation while radioactive isotopes are good indicators of residence time.

Stable isotopes

Variations in the abundance of stable isotopes of ^{2}H and ^{18}O, which are usually reported as a deviation from the standard isotopic ratio in some standard sample, give information about the chemical evolution of the groundwater (Fitts, 2002). The standard reference point is the Standard Mean Ocean Water (SMOW) and deviations are expressed in per mille (or ‰) (Mook et al., 2000). The deviation is calculated using the following equation:

$$\delta = \left[\frac{R_{sample}}{R_{standard}} - 1\right] \times 1000\ ‰, \qquad 4.1$$

where R represents a ratio of either ^{18}O to ^{16}O, or D to H (^{2}H/ ^{1}H). Unchanging isotopic content within an aquifer reflects the recharge processes, period and location of the water (Terwey, 1984). Changing isotopic content along groundwater paths reflects the history of the water such as mixing, salinisation and discharge processes (Terwey, 1984).

Radioactive isotopes

Radioactive isotopes are useful to determine the residence time of groundwater. The tritium rise (IAEA, 1981) in the atmosphere in the mid-sixties with tritium levels

rising to a record 61.1 TU (tritium units) in 1965, make it possible to date groundwater. Tritium has a half-life of 12.43 years, and today's rain in south Africa has 5 TU since the outburst in 1965. Thus, the age determined with this method is an average since the intergrowth of helium is not incorporated in the calculation.

The water circulation and age of groundwater will be used to identify different aquifers at Dayspring School.

4.5.3 Materials and methods

4.5.3.1 Description of the equipment and materials employed.

The Crison and Hannah instruments were used to collect the physical properties data. The Hannah instrument can measure pH, TDS, electrical conductivity, temperature, and redox potential while the Crison instrument can measure similar parameters as the Hannah except for the redox potential.

4.5.3.2 Explanation of the way in which the work was done.

These data were collected in March and August 2010 by Goba (2010) as part of her honours degree in geology. More detailed explanation of the way in which the work was done can be found in her report. Here I provide a summary of her work.

The borehole water was allowed to run for a few minutes before collecting samples, after which water was collected in a cup that would have been rinsed thrice with the borehole water to be sampled. Measuring electrodes were dipped into the cup for readings to be taken after they were calibrated using standard pH solutions. It took 5 minutes on average for the system to stabilize after dipping the electrodes, thus readings were taken after the readings had stabilized. An average of the readings between the two instruments was used.

Water was also collected with 1-liter bottles. The bottles were rinsed with water from the borehole where water was to be collected to eliminate contamination. The bottles were sealed tight after it has been observed that there were bubbles in the sample, and

they were labeled just after sealing to avoid mix-up. The water samples were then taken to iThemba Laboratories for isotope analysis.

4.5.4 Results and discussions

The redox potential data from DS2 was not analyzed at all while it was not analyzed in August for DS1 (Table 4.4). The pH values for DS1 are slightly acidic while the pH is slightly basic for DS2. Consequently, DS1 has higher TDS value than DS2. Thus, the electrical conductivity of DS1 is higher than that of DS2. However, the TDS and electrical conductivity result do not divulge any more significant information other than that the rock type is resistant to weathering. The temperature measured in August 2010 shows similar values between the two boreholes. The oxygen content that may be determined from the redox potential suggests that DS1 is an open system, i.e., there is interaction between water in the aquifer and the atmospheric oxygen.

Table 4.5. The physical properties of boreholes DS1 and DS2 (after Goba 2010).

Time	Borehole	depth	Pump rate	pH	temperature	TDS	E.C	EH
Month	code	m	litres/hr		°C	mg/l	mS/m	mv
March	DS1	50	<1000	6.97	23.0	143.2	22.4	14.00
August	DS1	50	< 1000	6.57	18.9	131.0	20.5	
August	DS2	162	1500	9.25	19.1	76.1	12.3	

Table 4.5 shows the results of the analysis of environmental isotopes. Again, it is clear from the data that DS1 and DS2 tap water from different aquifers because of the age difference of the waters. The age was calculated using the 12.43 years half-life of tritium. However, the age is an average, as the intergrowth of helium was not analyzed. The depletion in the stable isotopes suggests that the clouds that the water precipitated from formed far from the oceans. Furthermore, Figure 4.21 shows that DS2 is more depleted in ^{18}O than DS1 because DS2 is deeper. The stable isotopes were compared to the Global Meteoric Water Line (GMWL) and the Pretoria Local Meteoric Water Line (LMWL). The data shows that DS1 is shallower and unconfined

while DS2 is deeper and confined reveled by the depletion of ^{18}O in DS2 than in DS1.

In summary, the hydrogeology results have shown that borehole DS1 and DS2 draw water from different aquifers. This observation is revealed by the differences in physical properties and isotope data. Borehole DS1 is shallow and unconfined while DS2 is deep and confined.

Table 4.6. Analytical results of the isotopes of deuterium, oxygen-18, and tritium.

Time	Borehole	depth	δ D	$\delta^{18}O$	Tritium		Age	EH
months	code	m	(‰)	(‰)	(T.U.)		years	mv
March	DS1	50	-26.0	-4.63	1.2	±0.3	≥ 25	14.00
August	DS2	162	-29.3	-5.28	0.0	±0.2	> 60	

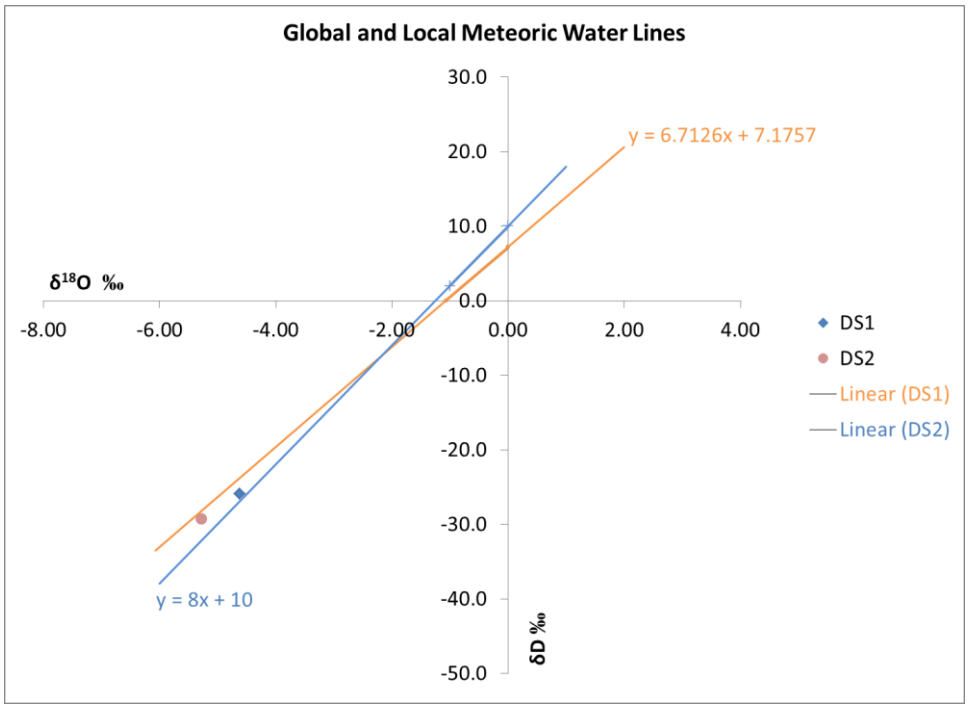

Figure 4.21. Deuterium and oxygen-18 variation in water samples from DS1 and DS2.

Chapter 5. General discussion

The purpose of this study was to examine the complex interaction between the geology, hydrology, and alien tree species. Thus, the discussion will look at each aspect and finally, an interaction amongst these aspects will be discussed under conclusions.

Geology

The gravity method has shown that there are at least two lithologies at Dayspring School, the feldspathic pyroxenite to the north and hornfels to the south. There is a possibility of hornfels further to the south as there is a gravity change in the vicinity of the school (Figures 4.15 and 4.16). However, the high variability in density of the hornfels (Lee, 2011) suggests that the gravity lows may just be hornfels of lower density. Similarly, the relatively high gravity to the south of the pyroxenite could be a hornfels of higher density (Figures 4.15 and 4.16). Gravity anomalies do not necessarily result from density change due to different rock types. The unevenness of the depth to bedrock, which is probably the case at Dayspring School, may produce gravimetric anomalies, which may be falsely interpreted as lithological change. For example, the outcrop of the pyroxenite to the north (Figure 2.2) suggests that the bedrock is shallow in that proximity, leading to higher gravimetric anomalies in this region.

The maps produced from DC resistivity, ground TDEM, and airborne TDEM show features that are directly correlated to the gravity data, though their spatial extent and amplitude are somewhat different. Electrical and electromagnetic methods have shown that there are at least two lithologies at Dayspring School (Figures 3.21, 3.23, 4.9 and 4.11). The shallower depth ranges (Figure 3.21a and 3.21b) from the DC resistivity data, the earlier delay times from the airborne EM data (Figure 4.9a and 4.9b) and ground TDEM (Figure 4.11a and 4.11b) show a response that is similar to the gravity (Figures 4.15 and4.16), i.e., pyroxenite to the north and hornfels to the south.. DC resistivity and ground EM data show that the rock to the west of the

hornfels has similar electrical properties as the pyroxenite. Therefore, it is possible that the pyroxenite continues further to the south in the western region of the gravity map (Figures 4.15 and 4.16).

The magnetic data give crucial evidence about the structural aspect of the geology of Dayspring School. It is clear from the magnetic data the north-south striking feature is not only conductive, but magnetic as well. A thin section derived from the borehole chips of DS2 (Figure 5.1) at a depth of 40 m reveal that the rock type is rich in pyroxene with few plagioclase and opaque minerals, probably magnetite, in which the magnetic signature can be explained. However, DS2 is further to south of the pyroxenite sill boundary (Figure 5.1), but has similar mineralogy as the sill. The lithology to the east of the unknown north-south feature, but south of the sill, was interpreted as hornfels due to the boulders of this rock type that are found in this area (Figure 5.1). Thus, the lithology to the west could be pyroxenite as revealed by similar mineralogy and electrical properties. Figure 5.2 shows the final geologic interpretation model.

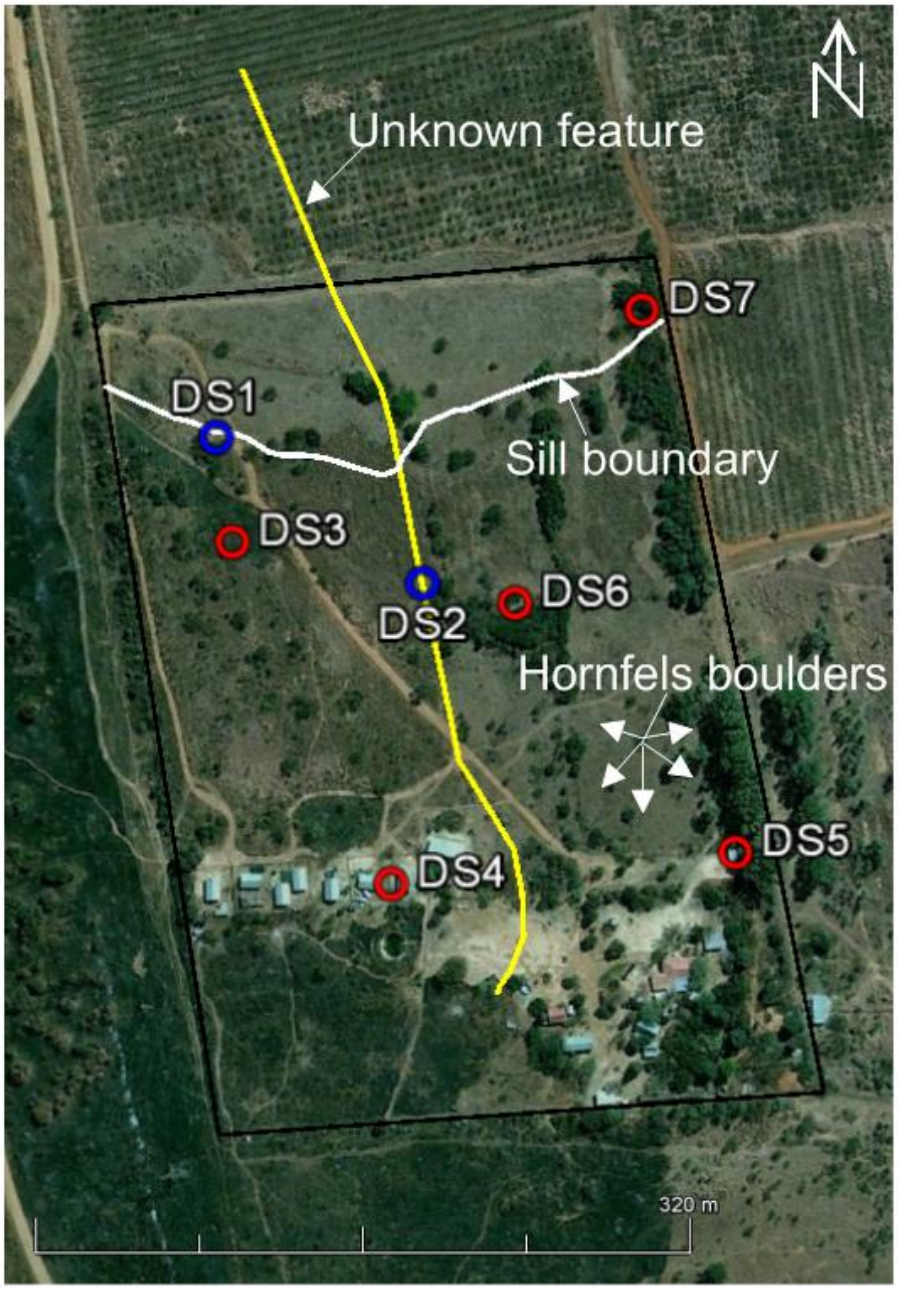

Figure 5.1. A map showing the position of the boreholes as well as the mafic sill boundary (white) as interpreted from gravity and resistivity methods. The unknown north-south striking feature (yellow) was mapped by electrical and magnetic methods.

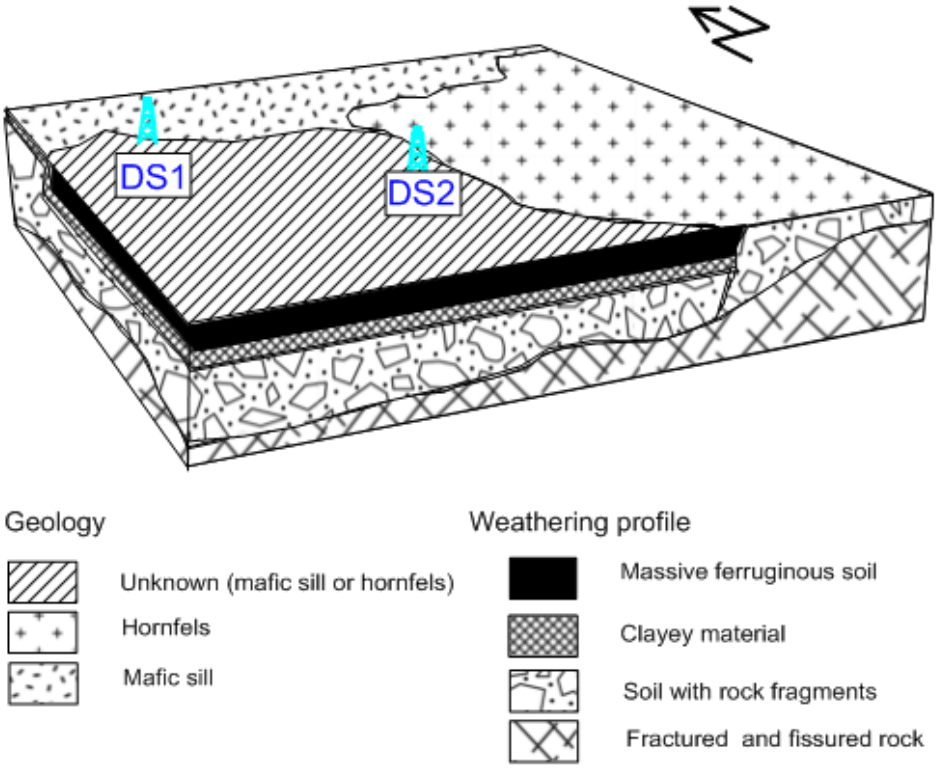

Figure 5.2. A schematic final geologic interpretation of Dayspring School for the top 45 m.

Hydrogeology

The occurrence of groundwater in crystalline rocks has already been discussed. What suffices to discuss is the occurrence of groundwater at Dayspring School. Barnard (2000) suggests that while groundwater levels occur between 10 and 25 m, the most favourable reservoirs would be brecciated or jointed zones. Thus, the contact between the mafic sills and the shales, slates, or hornfels should be potential water bearing zones. Borehole DS7 at Dayspring School was drilled on or close to probable jointed zones (Figure 5.1), but does not produce water.

The results from the geophysical methods have mapped linear features (lithological contact(s)), which are likely to host groundwater. The bedrock is probably fractured, at a depth of 35 m since the resistivity time-lapse data show resistivity changes at this depth, and according to literature, fractured bedrock should host good water (e.g. Acworth, 2001).

The locations of boreholes DS1, 2, and 7 seem to be on linear structures (Figure 5.1). In fact, Goba (2010) recognized that the borehole DS1 is located on lithological contact. Geophysical results have shown that borehole DS7 is also on or close to a lithological contact (Figure 5.1). Thus, it is perplexing that borehole DS1 is a low yield borehole, and DS7 is dry. Borehole DS3 may have been sited under assumption that part of the syenite dyke continues on to Dayspring School. Under this assumption, DS3 would have been at a contact; however, DS3 was unsuccessful as the dyke was not found.

Borehole DS3 is located on part of Dayspring School where the regolith is thicker. Based on other groundwater studies elsewhere in the world, this borehole, at a depth of 80 m, should produce water. The other boreholes, which were drilled at positions where there are no structural controls (Figure 5.1), dried up at depths of 30-35 m, which is the depth to the fractured rock in some parts of Dayspring. Thus, fractured bedrock aquifers are probable not good groundwater reservoir at Dayspring School. Geophysics cannot guarantee finding groundwater, however, for successful holes, borehole siting at Dayspring School should be in the proximity of a lithological contact since fractured-rock aquifers proved unproductive.

On the other hand, if good groundwater yields should be along lithological contacts, then why is borehole DS7 dry and why is borehole DS2 so deep. At least two explanations are possible for the apparent dry hole for DS7: (1) it may have collapsed, or (2) the siting did not consider the dip angle of the rocks. The deep water hole in DS2 may have been caused by drilling slightly off the probable joint, and thus intercepted a different (from DS1) aquifer at depth.

Impact of invasive plants

It is not clear from the time-lapse DC resistivity (and the time-lapse gravity data has not been fully processed) if the trees are responsible for the depletion of aquifers at Dayspring School though literature has shown that these invasive plants, bluegum especially, have a significant amount of water-withdrawal. Time-lapse resistivity data

have shown that profile 17 (Figure 2.2), which is the closest to the trees, had higher rate of dewatering (10-20%) below the bluegum trees, especially where the bedrock appears disjointed (Figure 3.47). The percentage change in resistivity is closely related to change in saturation, though percentage change in resistivity does not necessarily imply the same percentage change in saturation. Similar dewatering rates were observed in other profiles further away (160-200 m) from the trees, which makes it difficult to ascribe the dewatering to the trees. However, the higher dewatering rates observed in profiles 7 and 9 are due to higher hydraulic conductivity rate owing to different lithologies from north to south. Therefore, the resistivity increase near the bluegum can be attributed to the effect to the trees.

Conversely, with the annual rainfall in the region falling below the annual evaporation, it is most likely that most of the rainfall water will evaporate since the rate of infiltration is slow due to the low permeability of the baked top soil. In fact, Holland and Benyon (2010) concluded from their study of water use by bluegum, that most of the evapotranspiration was derived from evaporative losses directly from the surface soil. It is evident that at shallow subsurface (~ 5 m) the combination of plants with shallow roots, effect of temperature, and evaporation from the surface masks the impact of the invasive trees. The rate of water movement depends largely on the pore spaces, and with the geology at Dayspring being crystalline, rates of water-movement will be slow. Hence, the impact of these trees may not be dominant at shallow depth.

Another possible explanation for the inconclusive results about the impact of the trees obtained from time-lapse resistivity could be that of recovery nature of groundwater in linked aquifer system. The evidence from the work of Barker and Moore (1998) shows that groundwater or soilwater recovers after being drawn by substituting the missing waters. Evidently, the subsurface below DS1 should be drier than the surrounding, but it is not the case, hence groundwater recovery could be a possibility. Thus, the time-lapse resistivity method could not map the long-term effect of the either the borehole or the trees. However, as argued by Mook et al. (2000), fissured aquifers are usually discrete, therefore anisotropic, and thus not interconnected in

which case water substitution may not take place. Nevertheless, the results of time-lapse resistivity show that the fractures and cracks are interconnected because the changes in the resistivities of the bedrock revealed that there has been dewatering between the two set of measurements.

While the impact of the trees on shallow subsurface was monitored successfully, the presence of the trees cannot explain the apparent shortage of groundwater at Dayspring School. As discussed earlier, groundwater at Dayspring is structurally controlled (Figure 5.1). Bluegum trees at Dayspring School are ~20-30 m tall, and Sudmeyer et al. (2004) have shown that the root density of bluegum was highest in the top 0.5 m and the root lateral extent was 1.5 to 2 m times the height of the tree. Therefore, the maximum lateral length of the bluegum tree roots at Dayspring School is ~ 60 m. The distance between the sill boundary and the bluegum trees is > 120 m, and the distance between the bluegum trees and the unknown feature is ≤ 120 m (Figure 5.1). Thus, the trees do not tap into the geologic structures aquifers; hence, their presence cannot be used to explain the water shortage.

Groundwater contamination

The management of the school has stated that groundwater from DS2 at Dayspring is contaminated. A north-south striking feature with low resistivity and high magnetic response has been mapped. This feature could be leading contamination into DS2 because it close to a pit latrine near the houses.

Chapter 6. Conclusion and recommendations for further work

6.1 Conclusion

Integrated geophysical methods can be used to map geology in areas with complex geology and limited borehole data. 2D resistivity method, in the absence of seismic refraction, can give an estimate of the depth to bedrock though, can sometimes overestimate or underestimate depending on the resistivity contrast between the saprolite and the bedrock. The contrast in electrical properties of the regolith, which is derived from the bedrock, makes it possible for electrical methods to map the underlying geology. Redox potential, stable isotopes of deuterium and oxygen-18, and tritium analysis can give valuable insight on the character of the aquifer, water circulation and residence time respectively. In airborne surveys, the presence of large power line can mask narrow anomalies with high amplitudes. This type of features could carry contamination into boreholes. Hence, the combination of airborne and ground surveys yields good results. Impact of invasive trees can be determined using time-lapse resistivity and gravity; however, stringent techniques should be applied, especially in time-lapse gravity where precisions in position and elevation are very important. The impact of bluegum at Dayspring School can be seen from the time-lapse resistivity results, but cannot be used to explain the apparent shortage of water.

Insights in the geology and the hydrology of the study area have been gained. Groundwater at Dayspring School is structurally controlled. Depth to the bedrock varies between 11-35 m, and it is fissured at this depths, but does not hold enough water for exploitation. The rocks at Dayspring School are feldspathic pyroxenite to the north and hornfels to the south, and are resistant to weathering. The contacts between the different lithologies are good hosts of groundwater at Dayspring School as it was argued that ground waters in this region are structurally controlled. There are at least two aquifers at Dayspring School, with the shallower one being an unconfined aquifer, and the ground waters are older than 25 years in DS1 and DS2 has old water of > 60 years. Though, the time-lapse resistivity could not determine

satisfactory the impact of the invasive trees, it can be concluded, based on the distance between the bluegum and the geological structures (Figure 5.1), that the alien trees are not responsible for the depletion of groundwater. The dried up boreholes were not drilled on geological structures, hence, they dried-up owing to limited water in fissures and the weathered rock. If the water from DS2 is contaminated with E.coli, then the linear north-south striking feature may be carrying the contamination from pit latrine by the schoolhouses

6.2 Recommendations

I recommend that the trees should be removed to clarify the effect of the trees. In addition, I recommend that the gravity method should be applied carefully as it is the only method that can quantify the variations in groundwater, since resistivity cannot do so owing to the presence of clay and compact rock. I recommend that at least three holes be dug to ~5 m deep to confirm that the lithology to the east is probably different from the one to the west. The holes should be dug along crossline 15 (Figure 3.9) ; 1) to the east of the unknown feature (Figure 5.1), 2) on or close to the feature, and 3) to the west of the feature.

References

Acworth, I., 2001, The electrical image method compared with resistivity sounding and electromagnetic profiling for investigation in areas of complex geology: A case study from groundwater investigation in a weathered crystalline rock environment: Exploration Geophysics, **32**, 119-128.

Anand, R. R., 2005, Weathering history, landscape evolution and implications for exploration: Regolith Landscape Evolution Across Australia: A Compilation of Regolith Landscape Case Studies with Regolith Landscape Evolution Models. CRC LEME Monograph, 2–40.

Barker, R. and Moore, J., 1998, The application of time-lapse electrical tomography in groundwater studies: The Leading Edge, **17**, 1454.

Barker, R., Rao, T. V. and Thangarajan, M., 2001, Delineation of contaminant zone through electrical imaging technique: Current Science, **81**, 277-283.

Barnard, H. C., 2000, An Explanation of the 1:500 000 General Hydrological Map, Johannesburg 2526: Department of Water Affairs and Forestry.

Barsukov, P., Fainberg, E. and Khabensky, E., 2006, Shallow investigations by TEM-FAST technique: Methodology and examples: Methods in Geochemistry and Geophysics, **40**, 55-77.

Benyon, R. G., Theiveyanathan, S. and Doody, T. M., 2006, Impacts of tree plantations on groundwater in south-eastern Australia: Australian Journal of Botany, **54**, 181-192.

Bohidar, R. N., Sullivan, J. P. and Hermance, J. F., 2001, Delineating depth to bedrock beneath shallow unconfined aquifers: A gravity transect across the Palmer River Basin: Ground Water, **39**, 729-736.

Burger, R. H., Sheehan, A. F. and Jones, G. H., 2006, Introduction to Applied Geophysics: W.W. Norton & Company.

Button, A., 1973, A regional study of the stratigraphy and development of the Transvaal Basin in the eastern and northeastern Transvaal: Ph. D. dissertation, University of the Witwatersrand, Johannesburg, South Africa.

Calder, I. R., 1992, A model of transpiration and growth of Eucalyptus plantation in water-limited conditions: Journal of Hydrology, **130**, 1-15.

Carruthers, V., 1990, The Magaliesberg: Southern Book Publishers.

Christiansen, L., Lund, S., Andersen, O. B., Binning, P. J., Rosbjerg, D. and Bauer-Gottwein, P., 2011, Measuring gravity change caused by water storage variations: Performance assessment under controlled conditions: Journal of Hydrology, **402**, 60-70.

Claerbout, J. F. and Muir, F., 1973, Robust modeling with erratic data: Geophysics, **38**, 826.

Colin, F., Nahon, D., Trescases, J.J. and Melfi, A.J., 1990, Lateritic weathering of pyroxenites at Niquelandia, Goias, Brazil: The supergene behavior of nickel: Economic Geology, **85**, 1010-1023.

Conein, J. and Barker, R., 2002, The effects of tree roots on the electrical properties of Triassic clay: Proceedings of 8th Meeting of Environmental and Engineering Geophysical Society-European Section, Aveiro, Portugal.

Constable, S. C., Parker, R. L. and Constable, C. G., 1987, Occam's inversion: A practical algorithm for generating smooth models from electromagnetic sounding data: Geophysics, **52**, 289-300.

David, T. S., Ferreira, M. I., David, J. S. and Pereira, J. S., 1997, Transpiration from a mature Eucalyptus globulus plantation in Portugal during a spring-summer period of progressively higher water deficit: Oecologia, **110**, 153-159.

Davis, K., Li, Y. and Batzle, M., 2008, Time-lapse gravity monitoring: a systematic 4D approach with application to aquifer storage and recovery: Geophysics, **73**, WA61-WA69.

Dawson, T. E. and Pate, J. S., 1996, Seasonal water uptake and movement in root systems of Australian phraeatophytic plants of dimorphic root morphology: a stable isotope investigation: Oecologia, **107**, 13-20.

De Beer, J. H., Le Roux, C. L., Hanstein, T. and Strack, K. M., 1991, Direct current resistivity and LOTEM model for the deep structure of the northern edge of the Kaapvaal craton, South Africa: Physics of the Earth and Planetary Interiors, **66**, 51-61.

De Beer, J. and Stettler, E., 1992, The deep structure of the Limpopo Belt from geophysical studies: Precambrian Research, **55**, 173-186.

—1988, Geophysical characteristics of the southern African continental crust: Journal of Petrology, 163-184.

de Groot-Hedlin, C. D. and Constable, S. C., 1990, Occam's inversion to generate smooth, two-dimensional models from magnetotelluric data: Geophysics, **55**, 1613.

Devkurran, N., 2010, An investigation of water movement within an aquifer using 4D gravity: Honours report (unpublished), University of the Witwatersrand, Johannesburg, South Africa.

Dey, A. and Morrison, H. F., 1979, Resistivity modeling for an arbitrary shaped two-dimensional structures: Geophysical Prospecting, **27**, 106-136.

Edwards, L. S., 1977, A modified pseudosection for resistivity and IP: Geophysics, **42**, 1020.

Eriksson, P. G. and Clendenin, C. W., 1990, A review of the Transvaal sequence, South Africa: Journal of African Earth Sciences (and the Middle East), **10**, 101-116.

Fitterman, D. V. and Stewart, M. T., 1986, Transient electromagnetic sounding for groundwater: Geophysics, **51**, 995.

Fitts, C. R., 2002, Groundwater Science: Academic Press.

Fritzsche, F., Abate, A., Fetene, M., Beck, E., Weise, S. and Guggenberger, G., 2006, Soil–plant hydrology of indigenous and exotic trees in an Ethiopian montane forest: Tree Physiology, **26**, 1043.

Goba, R., 2010, Hydrogeological Characterisation of Dayspring area, Magaliesberg South Africa: Honours report (unpublished), University of the Witwatersrand, Johannesburg, South Africa.

Geological Survey of South Africa, 1981, 2526 Rustenburg Geological Map: **1:250000**, 1.

Greenwood, E. A. N., Klein, L., Beresford, J. D. and Watson, G. D., 1985, Differences in annual evaporation between grazed pasture and Eucalyptus

species in plantations on a saline farm catchment: Journal of Hydrology, **78**, 261-278.

Hales, A. and Gough, D., 1959, Gravity anomalies and crustal structure in South Africa: Geophysical Journal of the Royal Astronomical Society, **2**, 324-336.

Hazell, J. R. T., Cratchley, C. R. and Preston, A. M., 1988, The location of aquifers in crystalline rocks and alluvium in Northern Nigeria using combined electromagnetic and resistivity techniques: Quarterly Journal of Engineering Geology and Hydrogeology, **21**, 159.

Hiscock, K., 2005, Hydrology: Principles and Practice: Blackwell.

Holland, K. L. and Benyon, R. G., 2010, Water use by Eucalyptus globulus plantations over shallow groundwater on the Fleurieu Peninsula: CSIRO, 1835-095X.

IAEA, 1981, Statistical Treatment of Environmental Isotope Data in Precipitation: IAEA, 206.

Jones, G. M., Cassidy, N. J., Thomas, P. A., Plante, S. and Pringle, J. K., 2009, Imaging and monitoring tree-induced subsidence using electrical resistivity imaging: Near Surface Geophysics, **191**, 147-236.

Kaufman, A. A. and Anderson, B., 2010, Principles of electric methods in surface & borehole geophysics: Methods in geochemistry & geophysics, **44**, 1- 439.

Kim, J. H., Yi, M. J., Park, S. G. and Kim, J. G., 2009, 4-D inversion of DC resistivity monitoring data acquired over a dynamically changing earth model: Journal of Applied Geophysics, **68**, 522-532.

Kirsch, R., 2006, Groundwater Geophysics: a tool for hydrology: Springer.

Lane, R., Green, A., Golding, C., Owers, M., Pik, P., Plunkett, C., Sattel, D. and Thorn, B., 2000, An example of 3D conductivity mapping using the TEMPEST airborne electromagnetic system: Exploration Geophysics, **31**, 162-172.

Lane, R., Plunkett, C., Price, A., Green, A. and Hu, Y., 1998, Streamed data-a source of insight and improvement for time-domain airborne EM: Exploration Geophysics, **29**, 16-23.

Le Maitre, D. C., Scott, D. F. and Colvin, C., 1999, A review of information on interactions between vegetation and groundwater: Water S.A., **25**, 137-152.

Lee, S., 2011, 4D Time-lapse gravitational investigation at the Dayspring Children's Village: Honours report (unpublished), University of the Witwatersrand, Johannesburg, South Africa.

Lines, L. R. and Treitel, S., 1984, A review of least-squares inversion and its application to geophysical problems: Geophysical Prospecting, **32**, 159-186.

Loke, M. H., Acworth I. and Dahlin, T., 2003, A comparison of smooth and blocky inversion methods in 2D electrical imaging surveys: Exploration Geophysics, **34**, 182-187.

Loke, M. H., 2001, Tutorial: 2-D and 3-D electrical imaging surveys: Geotomo Software, Malaysia.

—1999, Time-lapse resistivity imaging inversion: Proceedings of the 5th Meeting of the Environmental and Engineering Geophysical Society European Section, Budapest, Hungary.

Loke, M. H. and Barker, R. D., 1995, Least-squares deconvolution of apparent resistivity pseudosections: Geophysics, **60**, 1682-1690.

Lowrie, W., 2007, Fundamentals of Geophysics: Cambridge University Press.

McNeill, J., 1991, Advances in electromagnetic methods for groundwater studies: Geoexploration, **27**, 65-80.

Meyer, R. and De Beer, J. H., 1987, Structure of the Bushveld Complex from resistivity measurements: Nature, **325**, 610-612.

Mook, W. G., Gat, J. R., Meijer, H. A. J., Rozanski, K. and Froehlich, K., 2000, Environmental isotopes in the hydrological cycle: principles and applications: Technical Documents in Hydrology, **IV**, 1-200.

Nassir, S. S. A. and Lee, C. Y., 1999, Detection of man-made voids by 2D & 3D geoelectrical imaging surveys: Exploration Geophysics, **30**, 141-146.

Nelson, D., 2002, Natural Variations in the Composition of Groundwater: Drinking Water Program, Springfield, Oregon.

Ngobeni D.D., 2009, A geophysical investigation of the hydrology of the Dayspring School: Honours report (unpublished), University of the Witwatersrand, Johannesburg, South Africa

Palacky, G. J., 1988, Resistivity characteristics of geologic targets, in Nabighian, M. N., Ed., Electromagnetic Methods in Applied Geophysics, **1**, Theory: Soc. Expl. Geophys.

—1981, The Airborne Electromagnetic Method as a Tool of Geological Mapping: Geophysical Prospecting, **29**, 60-88.

Palacky, G. J., Ritsema, I. L. and Jong, S. J., 1981, Electromagnetic Prospecting for Groundwater in Precambrian Terrains in the Republic of Upper Volta: Geophysical Prospecting, **29**, 932-955.

Pohjonen, V. and Pukkala, T., 1990, Eucalyptus globulus in Ethiopian forestry: Forest Ecology and Management, **36**, 19-31.

Rosqvist, H., Dahlin, T., Fourie, A., Rohrs, L., Bengtsson, A. and Larsson, M., 2003, Mapping of leachate plumes at two landfill sites in South Africa using geoelectrical imaging techniques: Proceedings of the ninth waste management and landfill symposium, Cagliari, Italy.

Roy, A. and Apparao, A., 1971, Depth of investigation in direct current methods: Geophysics, **36**, 943-959.

Samraj, P., Sharda, V. N., Chinnamani, S., Lakshmanan, V. and Haldorai, B., 1988, Hydrological behaviour of the Nilgiri sub-watersheds as affected by bluegum plantations, part I. The annual water balance: Journal of Hydrology, **103,** 335-345.

Sasaki, Y., 1989, Two-dimensional joint inversion of magnetotelluric and dipole-dipole resistivity data: Geophysics, **54,** 254-262.

Sepato, O., 2011, Magnetic investigation of geological structures at Dayspring Children's Village: Honours report (unpublished), University of the Witwatersrand, Johannesburg, South Africa.

Sharda, V. N., Samraj, P., Chinnamani, S. and Lakshmanan, V., 1988, Hydrological behaviour of the Nilgiri sub-watersheds as affected by bluegum plantations, part II. Monthly water balances at different rainfall and runoff probabilities: Journal of Hydrology, **103**, 347-355.

Sharda, V. N., Samraj, P., Samra, J. S. and Lakshmanan, V., 1998, Hydrological behaviour of first generation coppiced bluegum plantations in the Nilgiri sub-watersheds: Journal of Hydrology, **211**, 50-60.

Sikka, A. K., Samra, J. S., Sharda, V. N., Samraj, P. and Lakshmanan, V., 2003, Low flow and high flow responses to converting natural grassland into bluegum

(Eucalyptus globulus) in Nilgiris watersheds of South India: Journal of Hydrology, **270**, 12-26.

Stettler, E. H., 1979, A geological and geophysical investigation of the diamond runs on Ruigtelaagte and vicinity in the Bakerville area, Lichtenburh District, MSc. thesis (unpublished), University of Pretoria.

Stettler, E., Du Plessis, J. and De Beer, J., 1988, The structure of the Pietersburg greenstone belt, South Africa, as derived from geophysics: South African Journal of Geology, **91**, 292-303.

Sudmeyer, R. A., Speijers, J. and Nicholas, B. D., 2004, Root distribution of Pinus pinaster, P. radiata, Eucalyptus globulus and E. kochii and associated soil chemistry in agricultural land adjacent to tree lines: Tree Physiology, **24**, 1333-1346.

Telford, W. M., Geldart, L. P. and Sheriff, R. E., 1990, Applied Geophysics: Cambridge University Press.

Terwey, J. L., 1984, Isotopes in groundwater hydrology: Challenges in African Hydrology and Water Resources, Harare.

Tessema, A., Mengistu, H., Chirenje, E., Abiye, T. and Demlie, M., 2011, The relationship between lineaments and borehole yield in North West Province, South Africa: results from geophysical studies: Hydrogeology Journal, **20**, 351-368.

Todd, D. K. and Mays, L. W., 2005, Groundwater Hydrology: John Wiley & Sons, Inc.

Van Overmeeren, R. A., 1981, A combination of electrical resistivity, seismic refraction, and gravity measurements for groundwater exploration in Sudan: Geophysics, **46**, 1304-1313.

van Schoor, M., 2002, Detection of sinkholes using 2D electrical resistivity imaging: Journal of Applied Geophysics, **50**, 393-399.

Van Zijl, J. S. V., 1977, A practical manual on the resistivity method: CSIR, k79.

—1969, A deep Schlumberger sounding to investigate the electrical structure of the crust and upper mantle in South Africa: Geophysics, **34,** 450-462.

Van Zijl, J. S. V., Hugo, P. L. V. and Bellocq, J. H., 1970, Ultra Deep Schlumberger Sounding and Crustal Conductivity Structure in South Africa: Geophysical Prospecting, **18**, 615-634.

Van Zijl, J. S. V. and Joubert, S. J., 1975, A crustal geoelectrical model for South African Precambrian granitic terrains based on deep Schlumberger soundings: Geophysics, **40**, 657-663.

Vickery, A. C. and Hobbs, B. A., 2002, The effect of subsurface pipes on apparent-resistivity measurements: Geophysical Prospecting, **50**, 1-13.

Webb, S. J., Ngobeni, D., Jones, M., Abiye, T., Lee, M., Devkurran, N., Goba, R., Burrows, D., Ashwal, L.D., Pellerin, L. (2011): Hydrogeophysical investigation for groundwater at the Dayspring. The Leading Edge, **30**, 434-440.

Appendix

DC resistivity data obtained using dipole-dipole array for the crosslines

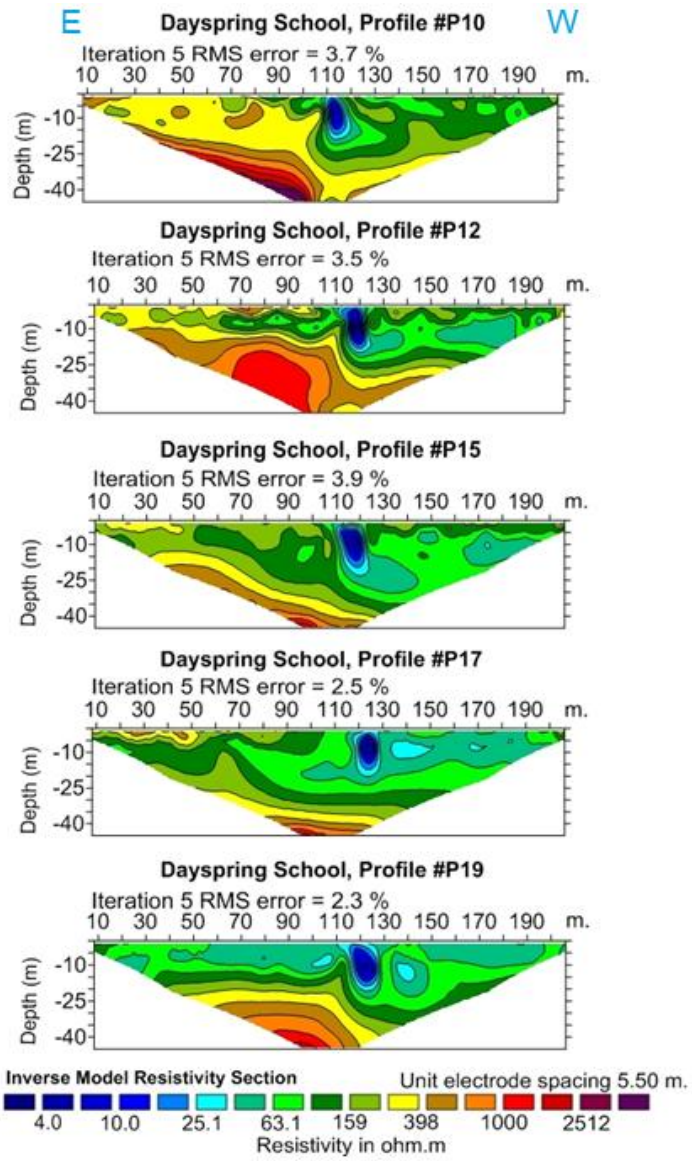

Figure A-1. Electrical image showing data collected along crossline 10, 12, 15, 17, and 18 using the dipole-dipole array in May 2011.